Towards high resolution Particle Image Velocimetry

Estimating turbulence statistics from the ensemble correlation

Sudarshan Sridharan

Technische Universiteit Delft

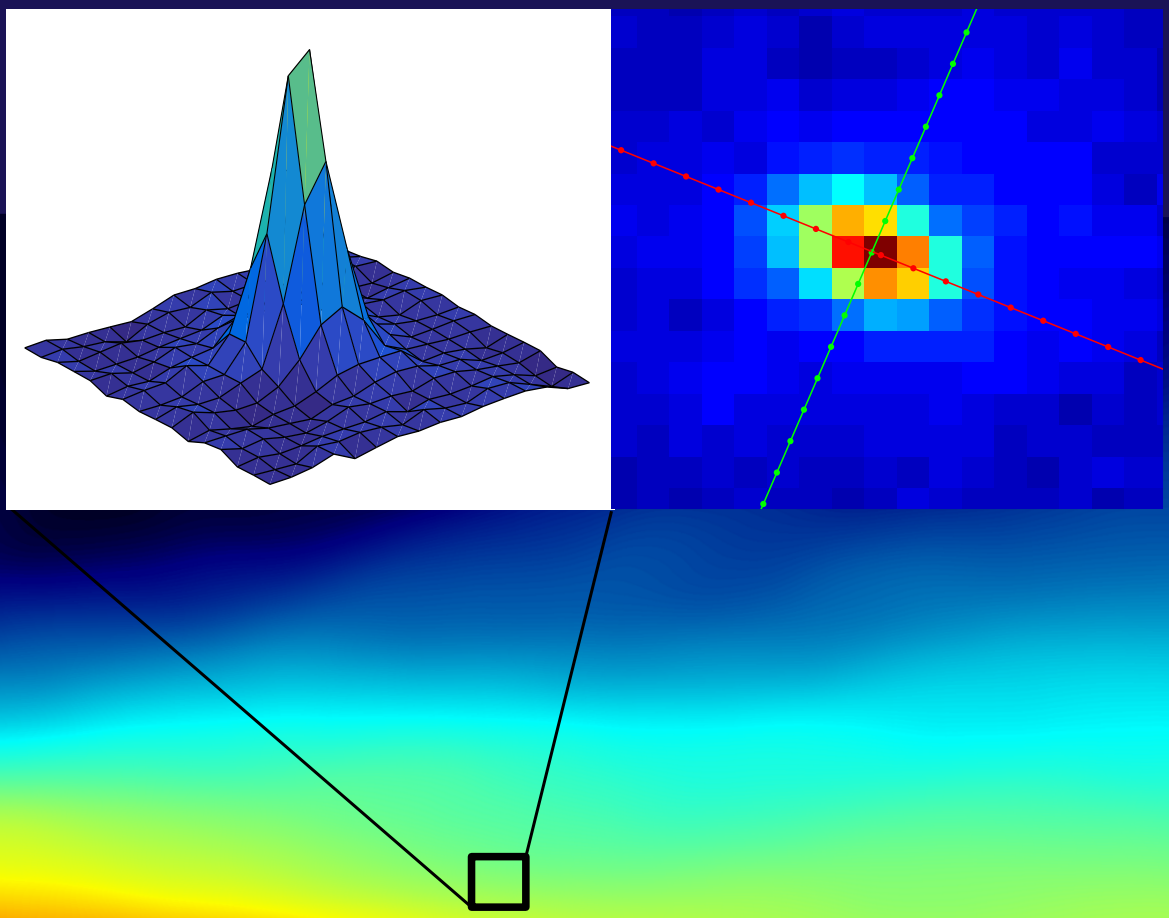

Towards high resolution Particle Image Velocimetry

by

Sudarshan Sridharan

in partial fulfillment of the requirements for the degree of

Master of Science
in Mechanical Engineering

at the Delft University of Technology,
to be defended publicly on Thursday October 25, 2018 at 10:00 AM.

P & E Report number: 2926

Supervisors:	Prof. dr. ir. Jerry Westerweel,	TU Delft
	Dr. ir. Gosse Oldenziel,	Deltares/TU Delft
Thesis committee:	Prof. dr. ir. R. A. W. M. Henkes,	TU Delft
	Prof. dr. ir. Francois Clemens,	TU Delft
	Dr. ir. Pepijn Pennings,	Dynaflow Research Group

This thesis is confidential and cannot be made public until October 25, 2018.

TU Delft Delft University of Technology

Acknowledgement

The thesis presented is a result of support and contributions from several people over last ten months, to whom I extend my heartfelt gratitude.

Firstly, I would like to thank my supervisor, ***Dr. Jerry Westerweel***. Thank you very much for guiding me throughout the project, dealing with me with patience, and shaping the work by providing valuable feedback. I learned a lot from our discussions, and your suggestions and directions to approach towards the problem statement were immensely helpful. Your encouragement to defend the results I obtained further motivated me to research and gain in-depth knowledge in the field. I really hope I will have a chance to work with you again in the future.

I am deeply grateful to ***Dr. Gosse Oldenziel*** for the effort he has put into my thesis. It is due to your interest and eagerness in the work, I am able to submit the thesis on time. Thank you for being always available for several discussions we had in person as well as via internet. I learned a lot from you, not just in research but also on people skills. The interest you showed in the project, by linking several people motivated me to work harder. The experiments wouldn't have been possible without your contribution. Your valuable inputs to write this report are profoundly appreciated.

I would also like to thank ***Edwin Overmars***. Many thanks to you to have taught me means to perform a PIV experiment. Your patience and guidance were very instrumental throughout my work. Your suggestions in studying the reflections in the pipe is a major reason for the quality of the PIV data acquired. Also, thank you for helping me with experiments at Deltares and assisting me with issues faced during the measurements.

I extend my gratitude to ***Michiel Tukker***, for operating the Alpha Loop facility, without which the experiments wouldn't be possible. Thank you for sharing your knowledge on various practical aspects of performing experiments, and many smarter ways to improve the quality of measurements.

I would like to thank ***Jasper Ruijgrok*** and ***Job Waaijerink*** for assisting me with constructing the experimental setups. I am also thankful to ***Ernst Jan Grift*** for allowing me to construct the jet flow experiment at the Row-boat facility. I extend my gratitude to ***Ankur Kislaya*** for introducing me to PIV analysis and guiding me throughout the thesis. I extend my gratitude to everyone at Deltares in helping with the experiments.

Lastly, I would like to thank my friends for supporting me throughout my Masters program. Special thanks to ***Puja*** and ***Anshul*** for providing constant support and encouragement. Lastly, I would like to thank my family for their support during the whole journey of my Masters program.

Sudarshan Sridharan
Delft, October 2018

Abstract

The research in resolving the smaller scales of turbulence has gained significant attention in recent years, owing to the advancements in the measurement techniques. High resolution experimental studies are required to investigate high Reynolds number flows where the scales of turbulence are very small. This is of particular importance in addressing the theoretical issues in studying high Reynolds number wall turbulence which finds applications in transport, energy, and aerospace industries. Hot-Wire Anemometry (HWA) is often employed to reach very high spatial resolution. Early research in Particle Image Velocimetry (PIV), a qualitative flow visualization technique, was not able to achieve a higher resolution as comparable with that of HWA. However, recent developments in PIV allow high resolution measurements, using information on the time averaged ensemble correlation. The ensemble correlation can be used to reduce the size of the interrogation windows employed in a PIV analysis, without compromising for the particle image density in an interrogation window. This is achieved by using a large number of image pairs. In this thesis, ensemble correlation is used to study the turbulence in two specific cases: a turbulent jet and high Reynolds number pipe flow.

The ensemble correlation, though being a time averaged quantity, contains information on the velocity Joint Probability Distribution Functions (JPDFs) which can be used to estimate the turbulence statistics. This information can be retrieved from the shape of the ensemble correlation. It is assumed that the ensemble correlation is the convolution of the auto-correlation and the velocity JPDFs. The velocity JPDFs are retrieved by estimating the second moments of the ensemble correlation by fitting a Gaussian profile, and further using a correction for auto-correlation. The second moments can be used to estimate the Reynolds stresses in the flow.

The proposed method is validated by implementing it to study the turbulent jet. For this purpose, 9000 image pairs are acquired. The results show that the retrieved moments predict the Reynolds stresses accurately. Further, high Reynolds number pipe flow experiments are performed in the Alpha Loop facility at Deltares. The bulk Reynolds number is varied from 3.37×10^5 to 6.22×10^5, acquiring 20,000 image pairs per measurement series. Also, the pressure drop is measured across the pipe along with the PIV measurements to estimate the roughness of the pipe. The results from the PIV measurements show that the mean velocity profile follows a similar trend as observed in the literature. A small bias is observed between the mean velocity obtained from the ensemble correlation and that obtained by averaging the instantaneous velocity vectors, in regions of high velocity gradients. The Reynolds shear stress estimated from the shape of the ensemble correlation is underestimated. However, the streamwise turbulent fluctuations estimated follow a trend, similar to that observed in the literature.

Contents

List of Figures

List of Tables

List of Symbols

ϵ	RMS height of the surface irregularities	m
κ	'*Von Kármán*' constant	
λ	Wavelength of the laser light	m
μ	Dynamic viscosity of the fluid	kg/ms
ν	Kinematic viscosity of the fluid	m^2/s
$\overline{uv}$	Reynolds shear stress	
$\overline{u}$	Mean local velocity	m/s
ρ	Density of the fluid	kg/m^3
τ	Wall shear stress	N/m^2
b_u	Half-width of the jet	m
C_f	Skin friction coefficient	
d	Diameter of the pipe	m
f_D	Darcy-Weisbach friction factor	
F_I	Fraction of in-plane motion of particles in the plane of laser light sheet	
F_O	Fraction of out-of-plane motion of particles from the plane of laser light sheet	
K	Eddy viscosity	m^2/s
L	Length of pipe section	m
M_O	Magnification	
N	Number of image pairs	
p	Pressure	N/m^2
Q	Volumetric flow rate	m^3/s
R^*	Single pixel ensemble two point correlation	
R_{avg}	Ensemble cross-correlation	
Re	Reynolds number	
Re_*	Friction Reynolds number	
T	Temperature of the fluid	K

u	Local velocity	m/s
u^+	Mean velocity normalized with the friction velocity ($\overline{u}/u_*$)	
$u^{'}$	Fluctuating local velocity	m/s
u^{2+}	Normalized streamwise fluctuations	
u_*	Friction velocity	m/s
U_b	Bulk velocity	m/s
U_c	Centreline jet velocity	m/s
u_{cl}	Centreline velocity in a pipe	m/s
u_{rms}	Turbulent intensity	
v	Local velocity in wall normal direction in pipe; Local span-wise velocity in jet	m/s
y^+	Normalized wall unit	

1

Introduction

Turbulent flows are encountered almost everywhere in our routine life. The flow in the atmosphere, the smoke rising from a chimney, the wake behind a solid body, the water flowing out of a tap, and the motion of waves in sea are some classic examples of turbulence observed in daily life (Figure 1.1). The subject of turbulence has a distinguished history with enormous research dedicated on the topic. It is hence not surprising that it has been reviewed by some great minds over centuries, developing the theory of turbulence to how we interpret them today. Despite this enormous growth, turbulence still remains to be one of the challenging problems encountered in the classical physics. The complexity of turbulence is not only in its lack of physical understanding, but also in describing it mathematically. Turbulent flows find applications in many fields such as energy production, transport industry, weather prediction, aerospace industry, and so on. Most of these applications depend on the numerical simulations that use turbulence models which are often placed under scrutiny over its inadequacy in solving the problem, especially at high Reynolds numbers. Understanding turbulence is pivotal in predicting the flow accurately in all the mentioned fields.

One of the ways to measure the complexity of the flow is to classify them based on the Reynolds number ($Re = \rho u d/\mu$), interpreted as the ratio of the inertial forces ($\sim \rho u^2$) to the viscous forces ($\sim \mu u/d^2$), where u is the velocity, d is the length scale and, μ and ρ are the dynamic viscosity and the density of the fluid . Interestingly, most of the applications mentioned in the previous paragraph have flows at high Reynolds numbers. For example, the Reynolds number of a typical atmospheric boundary layer flow is of the order $O(10^5 - 10^6)$. High Reynolds number flows have received a lot of attention over the past decades because of large separation between the scales of the largest eddy and the smallest eddy. The friction Reynolds number, Re_* defined as the ratio of the characteristic size of the flow domain (say R) to the size of the smallest eddy (say η, also called as Kolmogorov length scale), gives a direct measure of how complicated modelling the turbulence can be, as η can be as small as 0.3 μm (Yakhot et al. [69]). Also, most of the theories of turbulence are only applicable at the high Reynolds number limit. These conditions make direct computations of turbulence (at high Re) extremely difficult, thus relying on the field experiments to develop the models and the scaling rules to predict the turbulence and the flow behaviour. However, it is also complicated to perform experiments at such Reynolds numbers. In order to achieve high Reynolds numbers in laboratories, either R has to be increased or η has to be decreased with both operations being challenging and expensive. Also, as the Reynolds number increases, η decreases almost proportionally. In addition to this, measuring the smaller scales of turbulence requires appropriate measurement techniques to reach high spatial and temporal

resolution.

(a) Atmospheric boundary layer [36].

(b) Pipelines used to transport gases [1].

(c) Flow in a dam [7].

(d) Smoke coming out of a chimney [16].

Figure 1.1: Few examples of turbulent flows encountered in daily life.

Experiments aimed at measuring the smaller scales of turbulence predominantly employ Hot-Wire Anemometry (HWA) to measure the associated velocity. The hot-wire anemometer sensor length can be as small as 60 μm (NSTAP, Vallikivi et al. [60]) and gives a continuous time signal, and is a front-runner in such high resolution measurements. The Princeton Superpipe facility [20], the Melbourne pipe and channel facility [37], and the MTL facility, KTH [43] are some of the experimental facilities that study the wall-bounded turbulence at a high resolution using HWA. HWA is a well developed technique, being used to measure the flow field for decades. However, it is a single point measurement technique and cannot produce instantaneous spatial structure of the flow [63], which would provide more insight into the structure of the flow and help in describing the turbulence statistics.

Particle Image Velocimetry (PIV) is another technique employed extensively to study turbulence. The advantage of PIV over HWA is its ability to produce qualitative as well as quantitative measurements of the flow field [5]. A single realization of a PIV measurement can reveal the spatial coherence present in the flow. This helps in estimating the spatial derivatives and describing the spatial turbulent statistics. Present day digital cameras allow PIV to operate at high frequencies, enabling PIV to reach high temporal resolution. The major drawback of this technique is its inability to reach high spatial resolution compared to that achieved by HWA, limited by the size of the interrogation windows used in conventional PIV processing. In a two-dimensional planar PIV, the resolution is constrained by the length and width of the interrogation windows, and the thickness of laser light sheet. Using the conventional analysis,

Figure 1.2: Turbulent water jet, depicting the macro-structure and the micro-structure (Van Dyke [61]).

a sophisticated high resolution study on the wall turbulence was performed by Willert et al. [68] employing 6 x 64 interrogation windows, and were able to produce results similar to that obtained in the Princeton Superpipe facility [60]. They were able to resolve up to 65 μm in the wall-normal direction. Recent developments in PIV show potential to reach even higher spatial resolution using the ensemble correlation process, even up to single pixel which for the case of Willert et al. [68] allows to resolve up to 11 μm. However, the resolution is still limited by the thickness of the laser light sheet (0.3 - 1 mm). The current study intends to use the ensemble correlation analysis to study the turbulence at high Reynolds numbers. In the next section, the development of PIV enabling high spatial resolution measurements, is described. It is followed by a brief description of the motivation for this project, followed by a short overview of the report.

1.1. Particle Image Velocimetry (PIV) at high spatial resolution

Since the introduction of PIV in 1980s, there has been a rapid development in this technique, making it the state-of-the-art measurement technique for two-dimensional and three-dimensional flow fields. The main advantages of using PIV are: the measurement method is non-intrusive, provides instantaneous velocity fields, and helps in flow visualization. Major drawbacks of PIV are its reliability on the tracer particles to follow the flow and the increase in noise when using smaller interrogation windows (Adrian and Westerweel [5]).

The general principle of PIV can be explained as follows: tracer particles, that are required (or close) to be neutrally buoyant in the flow medium, are uniformly distributed across the flow. The flow is illuminated for a short instance by high intensity pulsed laser light. The image of the illuminated flow is captured and along with this, another image is captured after a small time delay of Δt. The two images obtained are processed and the information on the displacement fields are retrieved (Figure 1.5). The first and second images are generally referred as first and second exposures respectively. The images are usually divided into

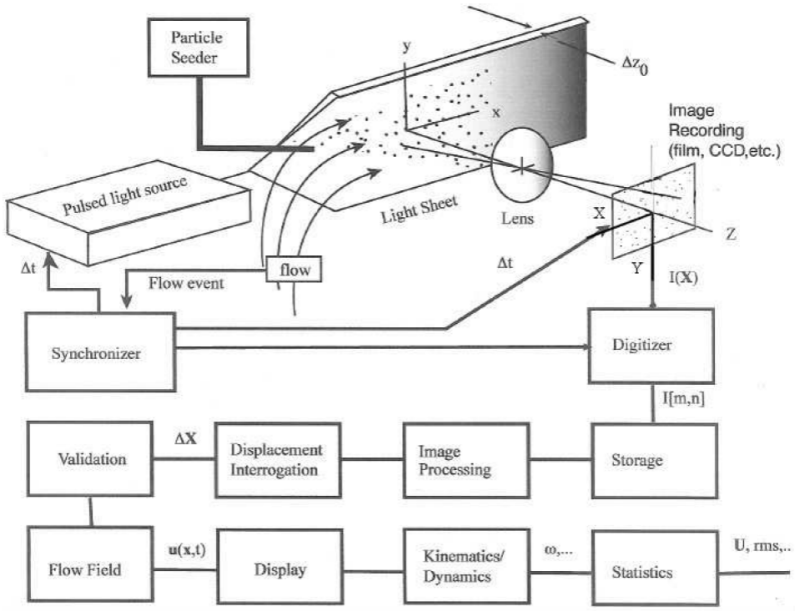

Figure 1.3: Elements and processes in a planar 2D particle image velocimetry system (Adrian and Westerweel [5]).

sub-regions, also called as interrogation windows, and these windows from the two exposures are correlated to produce the cross-correlation function. The position of the peak of the cross correlation yields the most probable displacement of all particles inside a particular interrogation window (Adrian [2]). In order to increase the accuracy to sub-pixel values, often a Gaussian curve is fitted to the correlation peak [5].

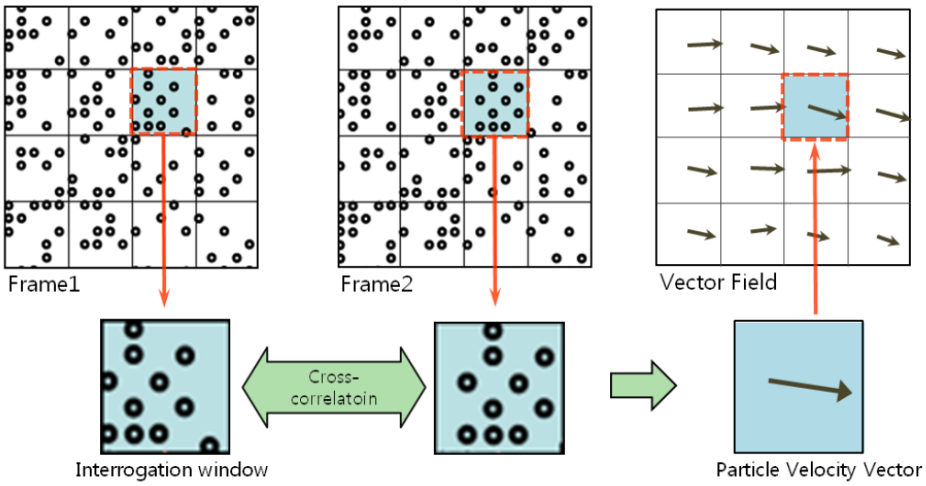

Figure 1.4: The cross-correlation of two interrogation windows from the two exposures yields a velocity vector per interrogation window (Choi et al. [10]).

In the initial stages of development of PIV, *Young's fringes* were used to compute the displacement wherein, the spaces between the fringes had an inverse relation with the magnitude of the displacement (Keane and Adrian [25]). This technique was then popularly called as *optical particle image velocimetry*. The evolution of PIV was complemented by the

developments in the optical measurements, the flow visualization and the image processing techniques. The development of digital cameras helped in digitizing PIV (DPIV), which increased the processing time to a greater extent and provided the base for much of the later advancements in PIV. This also allowed recording the images digitally and storing it in the digital memory. The electronic devices however have lower spatial resolution than the photographic films, but provide satisfactory amount of data. Over the years, numerous tracking algorithms and correlation analysis methods have been reported (Westerweel [63]), that has improved the performance of PIV significantly. PIV attracted many researchers especially to investigate the structure of turbulence because of its ability to capture the spatial structure and sense flow in all directions. However, it requires very small particles, a few microns in size. After the development of digital PIV, the research was focused in reaching higher spatial resolution. *Super-resolution* is a common term in PIV, referring to a type of interrogation that can improve the spatial resolution beyond the general interrogation window size used (Adrian [3]). Proposed by Keane et al. [24], the vectors from the standard correlation analysis were used to track the particles reliably in the image pair (5-10 individual particle vectors). There were also several improvements aimed at reaching high image density to produce more valid velocity vectors ([48],[56],[21]). As a rule of thumb, 10 particles per interrogation window are generally used in a conventional PIV interrogation ([42]). A detail review on the development of PIV is given by Adrian [3].

The interest in achieving higher resolution is motivated by the studies of high Reynolds number flow wall turbulence. These studies were predominantly performed using single point measurement techniques. One such technique in PIV to yield higher resolution is achieved by producing Ensemble correlation. Ensemble correlation is produced by averaging the cross correlations of the successive image pairs. At first, the ensemble correlation was used mainly to increase the signal-to-noise ratio of the cross correlation function. Delnoij et al. [14] implemented this technique to increase the signal-to-noise ratio while analyzing bubble flumes rising in a bubble column. They performed an ensemble average of spatial cross-correlation computed in identical positions for a set of 10-20 consecutive image pairs. Meinhart et al. [35] implemented this technique to compensate for low image density and to improve the signal-to-noise ratio of the spatial correlation in micro-PIV experiments. They call this technique as the *average correlation method*. The resolution was significantly improved to one pixel by Westerweel et al. [66] for micro-PIV applications, which can be interpreted as an extreme implementation of ensemble correlation. They implemented a two-point ensemble correlation and the technique was referred as '*single-pixel ensemble correlation* (SPE).

In a conventional PIV process, the spatial resolution of the velocity field is limited by the finite size of the interrogation window, with the number of particles in a window being the main limitation. With ensemble correlation, high signal-to-noise ratio can still be obtained using smaller interrogation windows due to averaging. This can also be interpreted as increasing the number of particles in a window (image density) without having to over-seed the flow. However, the ensemble correlation is a time averaging operation and hence loses the instantaneous information on the flow field. Despite this, the technique was extended to unsteady flows by Billy et al. [8]. They reported that, for unsteady flows on an average, the single pixel ensemble correlation does not compare well with the results from the cross correlation with window deformation (Scarano [49]). They recommend using more than one pixel to cross correlate (for example, 7 x 7 interrogation windows) and estimate ensemble correlation. They also observed the broadening of the shapes of the ensemble

correlation distribution. The technique was implemented in fully turbulent flows by Kähler et al. [22]. They report that turbulence spreads the probability distribution function of the cross correlation. The technique was further extended to stereoscopic recording by Scholz and Kähler [52]. The potential of SPE in resolving turbulence was shown by Scharnowski et al. [51]. They fitted Gaussian profiles to the SPE correlation function and estimated the Reynolds normal and shear stresses from the shape of the Gaussian profile. According to them, the velocity gradients stretch the correlation peaks and rotate them. Thus, the shape of the ensemble correlation contains information on the velocity distribution. Further, Strobl [58] showed that the moments can be directly estimated from the ensemble correlation instead of fitting Gaussian profiles, provided the correlation have very high signal-to-noise ratio.

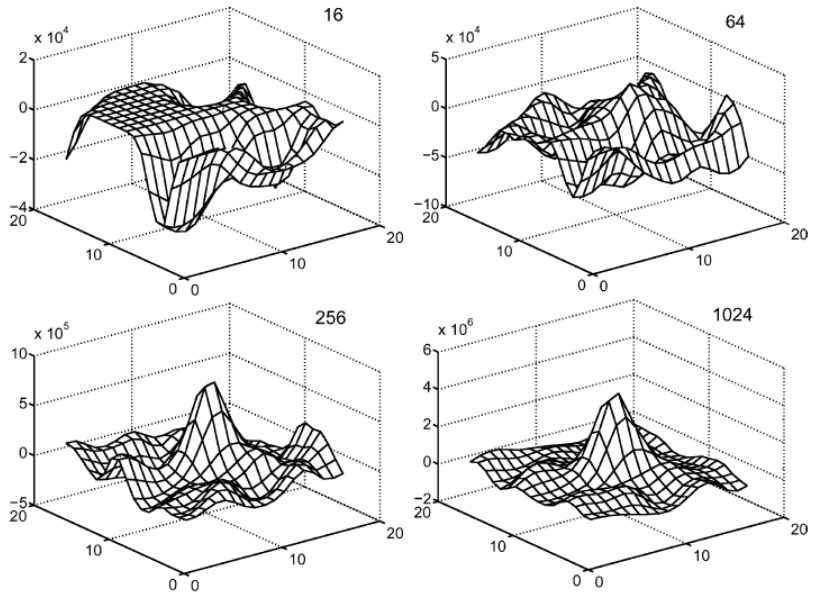

Figure 1.5: The increase in the signal-to-noise ratio in the spatial correlation with number of images using the single pixel ensemble correlation technique (Westerweel et al. [66]).

Recently, higher spatial resolution was also obtained using particle tracking velocimetry (PTV). The high resolution 4D-PTV "Shake-The-Box" technique (Schanz et al. [50]) employs fast and accurate tracking of particles using image matching process. According to Kähler et al. [23], a 2D-PTV would enable even higher resolution of mean velocity field close to walls and overcome the bias in the displacement fields observed in the case of ensemble correlation approach due to in-homogeneous seeding and steep velocity gradients. However, the estimation of Reynolds stresses is difficult (in PTV) due to the overlap of particle images in the case of high seeding concentration. With ensemble correlation, though they produce bias in the mean velocity field, the stresses can still be estimated at high accuracy [23].

1.2. Motivation

The shape of the ensemble correlation contains information on the velocity Joint Probability Distribution Functions (JPDFs) of the flow field [51]. The ensemble correlation is approximately given by the convolution of the particle image and the velocity JPDFs. Finding an analytical

expression for the velocity JPDFs is extremely difficult because of the involved deconvolution operation. However, an estimate of the velocity JPDFs can be obtained by fitting a Gaussian profile to the ensemble correlation. According to literature, the estimates for the velocity JPDFs obtained by following this method has high accuracy at higher spatial resolution [51], as the ensemble correlation can be implemented even at single pixel resolution [66].

By realizing the potential of the ensemble correlation approach, the small scales of turbulence can be well resolved and can match the spatial resolution achieved using single point measurements like HWA. With the ongoing uncertainties around the high Reynolds number wall-bounded turbulence over scaling [60] and other issues (discussed in detail in chapter 2), PIV with ensemble correlation provides a platform to contribute to the research in wall-bounded turbulence at such Reynolds numbers. From the experiments by Willert et al. [68], the spatial resolution along wall-normal direction is around 65 μm (same as the resolution obtained by high resolution HWA measurements [60]) using a 6 x 64 interrogation window. Going to single pixel resolution increases the resolution (in this case, by 6 times), providing a promising scope to resolve the smaller turbulence scales. Moreover, this would enable the use of PIV in studying high Reynolds number flows without having to compromise for spatial resolution.

1.3. Objective

The aim of the study is to find an estimate for the velocity JPDFs from the shape of the ensemble correlation obtained using PIV measurements. This is approached by estimating the statistical moments of the ensemble correlation by fitting a Gaussian profile to the ensemble correlation. The approach implemented in this study assumes that the convolution of the velocity JPDFs and the particle image results in the ensemble correlation. Since, the shape of the particle image can be assumed to be circular, the orientation of the velocity JPDFs and the ensemble correlation is then the same complying with the convolution operation. This is in contrast to the approach followed by Scharnowski et al. [51] where they report a bias in the orientation between the ensemble correlation and velocity JPDFs. The technique followed in the current study is verified by implementing it on a jet flow experiment, set up with same scale as the jet flow experiments performed by Westerweel et al. [65]. Further, the technique is used to estimate the mean velocity profile and the Reynolds stresses in high Reynolds number pipe flow at the Alpha loop facility at Deltares. The mean velocity profiles of the flow in the pipe is also a subject of interest.

1.4. Overview

The rest of the report consists of five more chapters. Chapter 2 provides an overview of challenges faced in the wall turbulence at high Reynolds numbers. Issues with the scaling laws, uncertainty in the '*Von Kármán*' constant and roughness are discussed briefly. Chapter 3 aims at describing the PIV and associated ensemble correlation approach analytically. The method used to retrieve the velocity JPDFs and the filters used are discussed towards the end of the chapter. In Chapter 4, the method described in Chapter 3 is implemented on the turbulent jet flow and compared with results from Westerweel et al. [65]. In Chapter 5, firstly, the Alpha loop facility is described in detail. The associated experimental conditions and methods used to improve the quality of the experiments like the study on reflections in the pipe are also discussed. The results obtained using the ensemble correlation approach are reported towards the end. The final chapter summarizes the entire work and presents some recommendations.

2

Wall turbulence at high Reynolds number flows

This section aims to put forth the challenges faced in studying the near wall turbulence at high Reynolds number flows. In order to study the wall turbulence exclusively, simple geometries are used, often flow in a pipe or through a channel. The available experiments are limited at high Reynolds numbers because of presence of thin boundary layers at such Reynolds numbers. Also, the measurement techniques employed are unable to completely resolve the near wall region. There are some theoretical issues in near wall region in terms of the scaling laws, some experimental constraints and lack of numerical simulations. There are many unanswered questions, some of which are scaling of the mean flow and the Reynolds stress, the extent of the logarithmic overlap region, and the universality of model parameters like the '*Von Kármán*' constant [31]. The chapter intends to discuss the recent trends and challenges in the subject. The first section introduces some common terms used in the thesis related to wall turbulence. The second section describes the scenario at high Reynolds numbers. Further, the challenges and issues are discussed based on the literature.

2.1. Reynolds Averaged Navier-Stokes Equations

The Reynolds averaged continuity and Navier-Stokes (RANS) equations in the Boussinesq approximation (Nieuwstadt et al. [42]) can be written as,

$$\frac{\partial \overline{u_i}}{\partial x_i} = 0, \tag{2.1}$$

$$\frac{\partial \overline{u_i}}{\partial t} + \frac{\partial \overline{u_i}\,\overline{u_j}}{\partial x_j} = \frac{1}{\rho_0}\frac{\partial \overline{p}}{\partial x_i} + \frac{g}{T_0}\overline{\theta}\delta_{i3} + \nu\frac{\partial^2 \overline{u_i}}{\partial x_j^2} - \frac{\partial \overline{u_i' u_j'}}{\partial x_j}, \tag{2.2}$$

where velocity (u_i), pressure (p) and temperature (θ) are decomposed to an average quantity represented by $\overline{u}$, $\overline{p}$, and $\overline{\theta}$ respectively, and the fluctuating quantity represented by prime ($'$) (For example, $u = \overline{u} + u'$). The index 'i' represents the direction of the respective quantities (or their components along direction 'i'). The transport term $\overline{u_i' u_j'}$ originates from the non-linear advection term in the RANS Equations. ρ_0 and ν are the density and the kinematic viscosity of the fluid respectively. A closure model is required in order to solve Equation (2.2). The turbulent stress tensor [42] can be written as,

$$\Sigma_{ij} = -\frac{1}{3}\rho_0 \overline{u_k'^2}\delta_{ij} + \rho_0\Big(-\overline{u_i' u_j'} + \frac{1}{3}\overline{u_k'^2}\delta_{ij}\Big). \tag{2.3}$$

The first term on the right hand side of Equation (2.3) can be perceived as *turbulent pressure* and in most flows, it is negligible compared to the static pressure (p). The second term can be perceived as deviatoric stress and can be written as,

$$\rho_0\Big(-\overline{u_i'u_j'} + \frac{1}{3}\overline{u_k'^2}\delta_{ij}\Big) = \rho_0 K\Big(\frac{\partial \overline{u_i}}{\partial x_j} + \frac{\partial \overline{u_j}}{\partial x_i}\Big). \tag{2.4}$$

where K is the *eddy viscosity*. The eddy viscosity is commonly modelled using the *Prandtl mixing length hypothesis*. According to the hypothesis, the characteristic velocity of an eddy, U obeys the following relation,

$$U \sim L\Big|\frac{\partial \overline{u}}{\partial y}\Big|. \tag{2.5}$$

where L is the characteristic length scale of the eddy. The eddy viscosity following a first order approximation empirically scales as,

$$K \sim UL. \tag{2.6}$$

In the following content, the flow is assumed to be fully developed, that is the flow is stationary and horizontally homogeneous. For the mean velocity, it holds that $\partial/\partial t = 0$ and $\partial/\partial x = 0$. Thus, the mean velocity can be written as $\overline{u_i} = (\overline{u}(y), 0, 0)$. The fully developed pipe flow can be completely represented in two dimensions. Also, the variation in the fluid density and the temperature are neglected. The continuity equation simplifies to $\partial\overline{v}/\partial y = 0$. Defining x and y coordinates as depicted in Figure 2.1, Equation (2.2) in x-direction simplifies to,

$$0 = -\frac{\partial \overline{p}}{\partial x} + \nu\frac{\partial^2 \overline{u}}{\partial y^2} - \frac{\partial \overline{u'v'}}{\partial y}. \tag{2.7}$$

Equation (2.2) in y-direction simplifies to,

$$0 = -\frac{\partial \overline{p}}{\partial x} - \rho_0\frac{\partial \overline{v'^2}}{\partial y}. \tag{2.8}$$

Figure 2.1 shows the two dimensional view of the flow in a pipe. The mean flow is generally represented as a function of the radial coordinate, r. However, the quantities inside the boundary layer are often represented as functions of the wall normal distance (y). To maintain consistency, Cartesian coordinates are used.

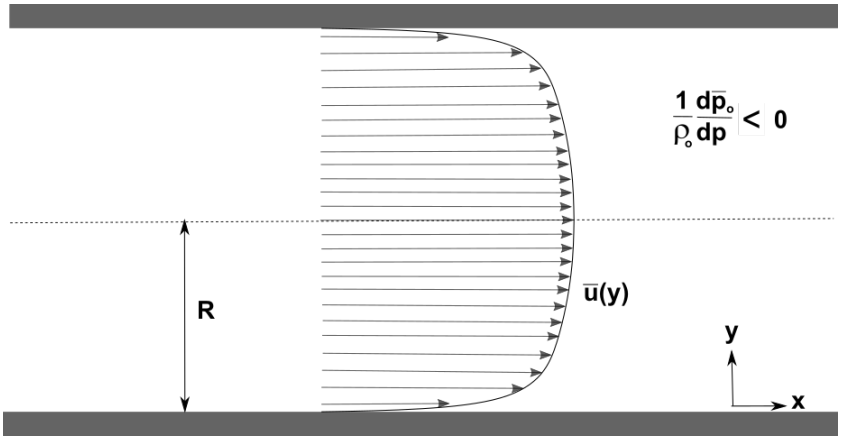

Figure 2.1: The geometry of the fully developed turbulent pipe flow with radius R, shown in two dimensions (x and y).

2.2. Mean velocity profile

The mean velocity profile in a turbulent pipe flow can be divided into four regions, based on the flow scales. Using the *Prandtl mixing layer* hypothesis, the characteristic length (L) is defined differently in different regions [42].

2.2.1. Core region

In this region (centre of the pipe), the characteristic size of eddies scale with the radius of the pipe as $L = \beta R$. The equation for the mean velocity in the core region is given by,

$$\overline{u} = u_0 - \frac{2}{3}\frac{u_*}{\beta}\left(1 - \frac{y}{R}\right)^{3/2}. \tag{2.9}$$

where u_0 is the integration constant and β is a constant obtained from experiments. u_* is the friction velocity defined as $\sqrt{\tau_s/\rho}$, where τ_s is the wall shear stress. Equation (2.9) is obtained by simplifying Equation (2.2) assuming fully developed conditions. For complete derivation, the readers can refer to Nieuwstadt et al. [42]. The value of the constant β is about 0.13 for turbulent pipe flows.

2.2.2. Wall region

The characteristic length of the eddy in this region scales with the distance of the region from the wall (y), and not on the radius of the pipe. The relation is given by $L = ky$, where k is the '*Von Kármán*' constant. From the experiments, the value of k is about 0.4. In this region, the total stress τ_s is approximately equal to ρu_*^2. The velocity profile is given by,

$$\overline{u} = \frac{u_*}{k} ln\left(\frac{y}{y_0}\right). \tag{2.10}$$

where y_0 is the integration constant. This region is popularly referred as *logarithmic or overlap* region.

2.2.3. Viscous sublayer

Equation (2.10) is not valid for y = 0. However, Equation (2.4) can be written in terms of friction velocity as, $u_*^2 = K\partial\overline{u}/\partial y$. The turbulent stresses are negligible very close to wall as only wall shear stress dominate. Thus, the velocity profile can be written as,

$$\overline{u} = \frac{u_*^2}{\nu} y. \tag{2.11}$$

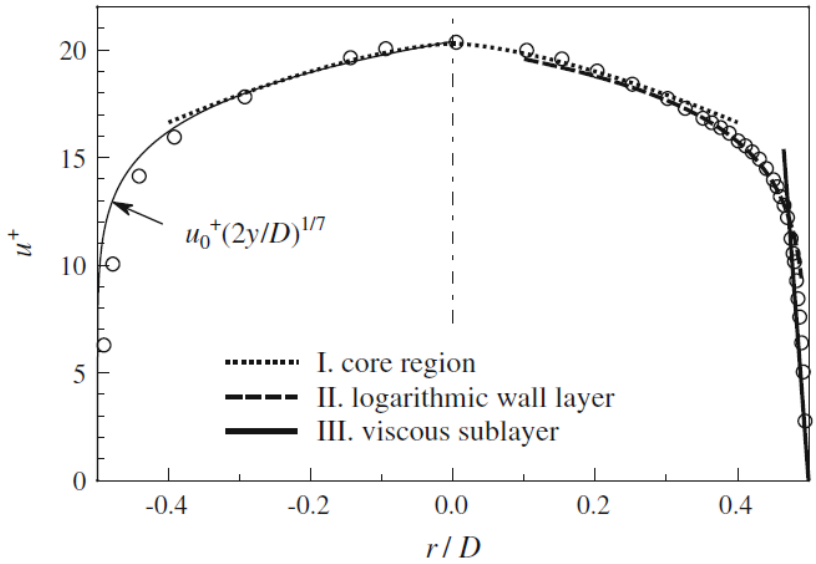

Figure 2.2: The normalized mean velocity (u^+) profile of a turbulent pipe flow at Re = 10,000 as a function of the radius, r. The right half represents Equation (2.9), Equation (2.10), and Equation (2.11). The left half represents a $\frac{1}{7}$th power law (Nieuwstadt et al. [42], Figure 6.2).

2.2.4. Important dimensionless parameters

In order to connect the profiles in the different regions, the velocity is matched at their boundary limits. This process yields two non-dimensional parameters,

$$u^+ = \frac{\overline{u}}{u_*} \; ; \; y^+ = y\frac{u_*}{\nu}. \tag{2.12}$$

These numbers are commonly referred as *wall units*. The extent of different regions can be expressed in terms of these parameters.

Viscous sublayer	:	y^+ = 0	to	y^+ = 5
Buffer region	:	y^+ = 5	to	y^+ = 30
Logarithmic region	:	y^+ = 30	to	r/D = 0.34
Core region	:	r/D < 0.34		

The buffer region is the region between the viscous region and the logarithmic region. Another non-dimensional number often encountered is the friction Reynolds number (R_*) is given by,

$$R_* = \frac{u_* d}{\nu}. \tag{2.13}$$

These wall parameters are used to normalize different quantities which are often encountered while dealing with wall turbulence.

2.3. Wall bounded high Reynolds number flow

Majority of the experiments and the simulations are dedicated to low and moderate Reynolds number flows, given such studies are more feasible compared to the high Reynolds number study. Also, a thicker viscous regime at lower Reynolds numbers makes it easier to study the wall turbulence and the coherent structures. This section aims to explain what makes high Reynolds number flows different, the challenges faced and anomalies observed based on the literature.

2.3.1. Scaling of the flow regions

The 'classical' scaling of wall turbulence popularly followed is based on the comprehensive reviews by Clauser [11] and Kline et al. [27]. Clauser [11] assumes a constant eddy viscosity model to predict the outer 80-90% of the turbulent boundary layer, including the overlap region. According to Gad-el Hak and Bandyopadhyay [19], the boundary layer is composed of two principle regions: a near wall region dominated by viscosity, and the outer region where effect of viscosity is negligible. The friction velocity (u_*) and the wall unit ($y^+ = \nu/u_*$) represents the scales of velocity and length from the wall in the near wall region respectively. In the outer region, the characteristic length scales with the boundary layer thickness (δ) or appropriate length (like radius of the pipe) while the velocity continues to scale with the friction velocity. The friction velocity is considered as a 'slip' velocity as seen by the outer scale motions, and is regarded as proper scale for the deviation of mean velocity from the freestream velocity by Townsend [59].

The mean velocity profile for fully developed pipe and channel flows, and zero-pressure gradient (ZPG) boundary layers (Coles [13]) can be expressed as,

$$u^+ = f(y^+) + \Pi g(y/R). \tag{2.14}$$

The first term in the RHS of Equation (2.14) describes the velocity in the near wall region and the second term describes the velocity at the outer region. The term Π is referred as the Coles wake factor (Coles [13]). For the near wall region, the inner function, $f(y^+)$ contributes to the mean velocity entirely. Therefore, as $y^+ \to 0$, $f(y^+) \to y^+$ and $g(0) \to 0$. The inner function diminishes further away from the wall. There exists a region where the mean velocity follows a logarithmic trend and is independent of viscosity, infamously called as logarithmic (overlap) region. The mean velocity profile in this region is given by,

$$u^+ = \frac{1}{\kappa} ln(y^+) + B. \tag{2.15}$$

where B is an additive constant which depends on the geometry of the flow (pipe/channel/boundary layer) and the roughness of the wall. Equation 2.15 is another convenient version of Equation (2.10). The values of κ reported in the past vary even though it is generally considered as a constant, with a value of 0.38 for boundary layer flows and a value of 0.42 in a pipe flow (Vallikivi et al. [60]). The uncertainty in κ is explained in brief later in the section. The pipe flow measurements by Zagarola and Smits [70] showed the presence of the extended logarithmic/overlap region even up to $y^+ = 1000$, wherein for low Reynolds number flows the logarithmic region is generally assumed to be located at $y^+ = 30$-50.

At high Reynolds number, the scaling for the mean velocity profile in a fully developed turbulent pipe flow in the overlap layer follows Equation (2.15), and in the outer layer it follows,

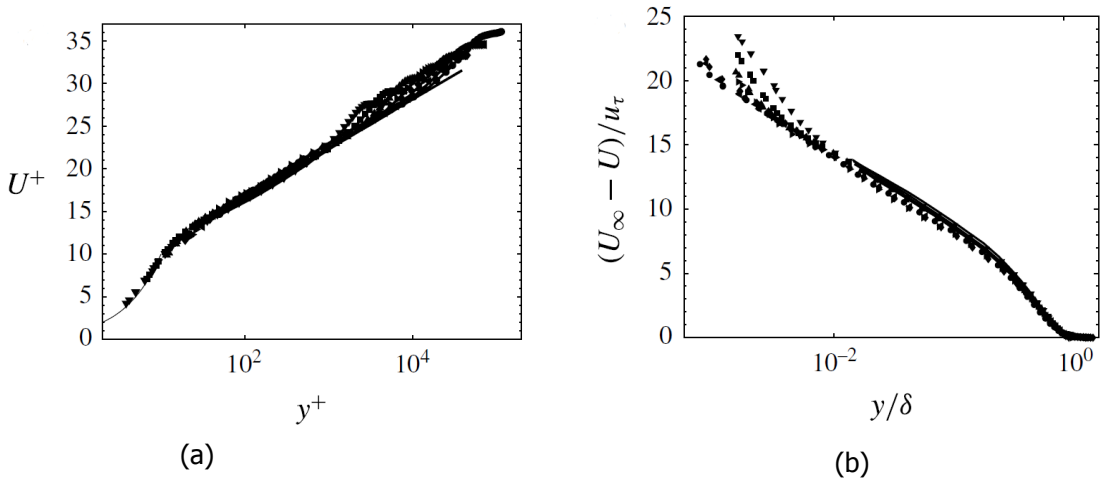

Figure 2.3: Boundary layer mean velocity profiles for Re_* = 3334 - 98,190.
(a) Inner coordinates, black lines follow Equation (2.15) with κ = 0.4 and B = 5.1;
(c) outer coordinates. (Vallikivi et al. [60], Figure 3). The symbols in the plots followed are given in Figure 2.6.

$$\frac{U_\infty - \overline{u}}{u_*} = -\frac{1}{\kappa} ln \frac{y}{R} + B^*. \tag{2.16}$$

where U_∞ is the centreline velocity, and B^* is the additive constant independent of Reynolds number (Mckeon et al. [34]). This is shown in Figure 2.3. Here, the symbols U^+, U, and u_τ represent u^+, $\overline{u}$, and u_* respectively as followed in this report.

At high Reynolds numbers, the streamwise fluctuations ($\overline{u'^2}$) also show logarithmic behaviour in the overlap region [59], [46].

$$u^{2+} = B_1 - A_1 ln \frac{y}{R}, \tag{2.17}$$

where $u^{2+} = \overline{u'^2}/u_*^2$, A_1 is the Townsend-Perry constant, and B_1 is the additive constant. This logarithmic behaviour was however observed only at very high Reynolds numbers ($Re_* > 20000$) for y/R < 0.12 by Hultmark et al. [20]. This scaling was also observed in the boundary layers by Marusic et al. [32]. They proposed a universal value of A_1 = 1.26 (Figure 2.4). Based on the conventions followed in this report, U_τ and U in Figure 2.4 represent u_* and $\overline{u}$ respectively.

The scaling behaviour of $\overline{u'^2}$ as a function of distance from the wall in inner coordinates (y^+) has also been the subject of interest at high Reynolds numbers. In general, $\overline{u'^2}$ has a near wall peak located at $y^+ \approx 15$. This peak denotes the location where the turbulence production rates are highest.

Earlier studies reported a constant magnitude of the near wall peak. However, the high Reynolds number atmospheric surface layer experiments (Kunkel and Marusic [28]) and moderate Reynolds number DNS simulations (El Khoury et al. [17]) showed a Reynolds number dependant magnitude of this near wall peak (Figure 2.5). This dependency is attributed to the interaction between near wall eddies and those further from the wall. In

contrast, Hultmark et al. [20] performed low Reynolds number experiments that indicate that the near wall peak is independent of the Reynolds number and depends only on the inner variables (Figure 2.6).

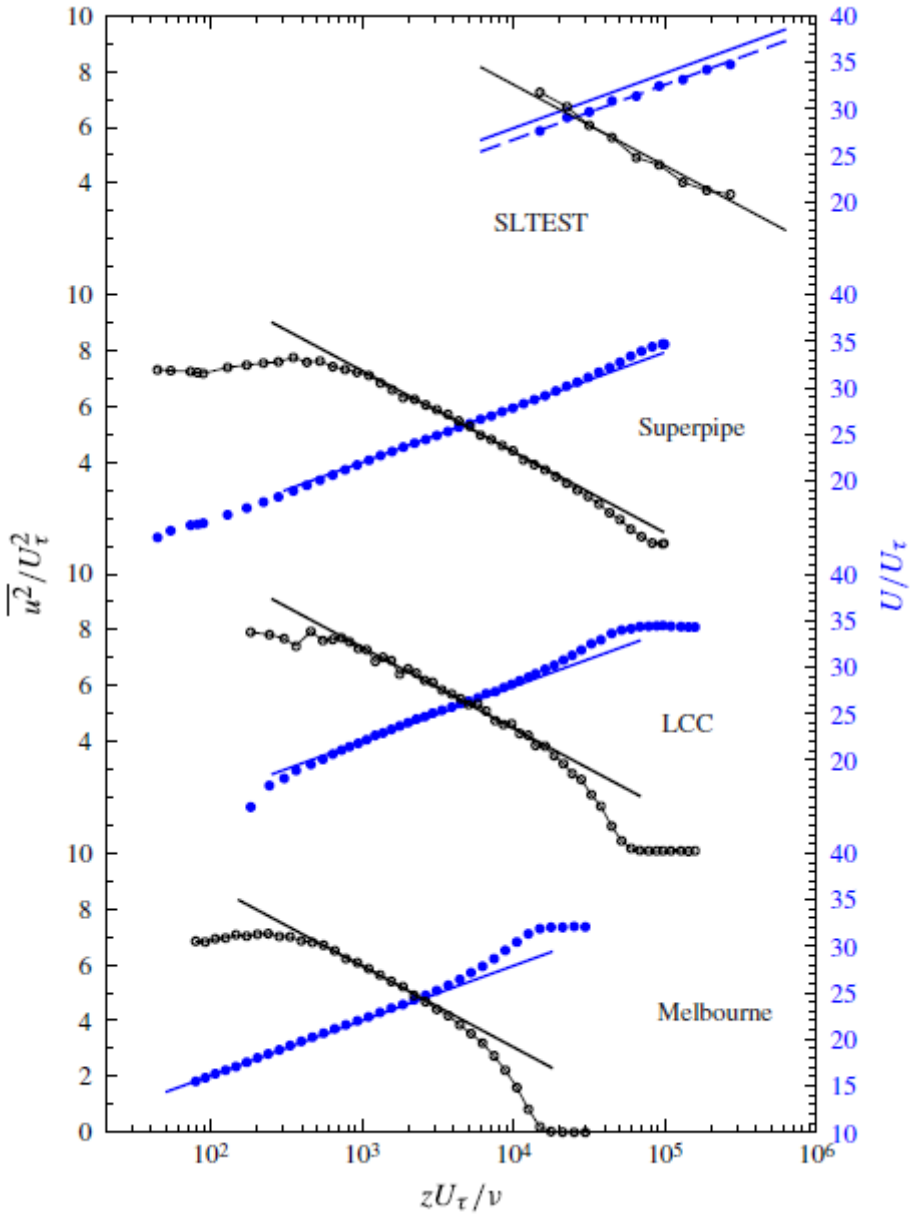

Figure 2.4: Streamwise turbulent intensity and mean velocity profiles: Melbourne wind tunnel, Re_* = 18010; LCC, Re_* = 68,780 (LDV); Princeton Superpipe, Re_* = 98,190 (NSTAP); SLTEST, Re_* = 628000 (Sonic). Solid straight lines correspond to Equation (2.15) and Equation (2.17) with κ = 0.39, B = 4.3, and A_1 = 1.26, respectively (Marusic et al. [32], Figure 1).

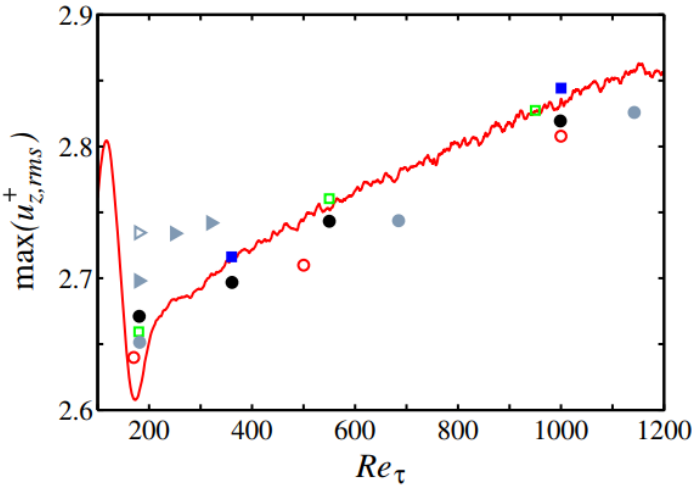

Figure 2.5: Maximum of inner scaled axial turbulence intensity ($u^+_{z,rms} = (\overline{u^{2+}})^{1/2}$ in this report) as a function of the friction Reynolds number (El Khoury et al. [17], Figure 10).

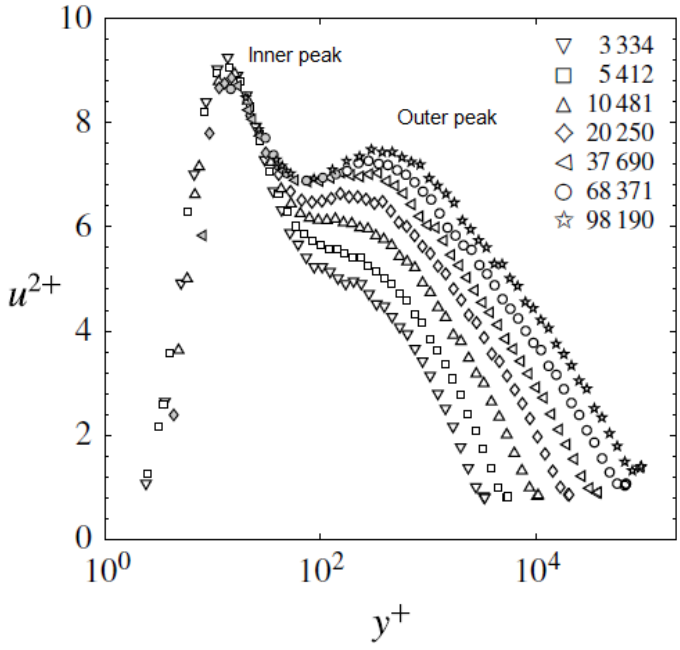

Figure 2.6: Inner scaled streamwise turbulence intensity corrected for spatial filtering effects following Smits et al. [54], taken from Vallikivi et al. [60] (Figure 4b). The legend shows the values of Re_*.

In addition to this inner peak at $y^+ = 15$, the results shown in Figure 2.6 also reveal the presence of an outer peak located between $100 < y^+ < 800$. The outer peak is only significant for the highest three friction Reynolds numbers measured in Figure 2.6. A similar observation was earlier reported by Morrison et al. [39]. However, their observations are often debated over issues with spatial filtering. The spatial resolution of their experiments varies from $l^+ = 11.6$ at $Re_* = 1500$ to $l^+ = 385$ at $Re_* = 1.01 \times 10^5$. Their results also show variations in the magnitude of the inner peak. This is depicted in Figure 2.7 along with the streamwise fluctuations (red line) as observed by [60].

In order to account for the effects of spatial resolution, Smits et al. [54] proposed a correction. According to them, the corrected streamwise fluctuations are given by,

$$\overline{u^{2+}}_{corrected} = [M(l^+)f(y^+) + 1]\overline{u^{2+}}, \tag{2.18}$$

$$f(y^+) = \frac{15 + ln(2)}{y^+ + ln[e^{(15-y^+)} + 1]}, \tag{2.19}$$

$$M = 0.0091l^+ - 0.069, \tag{2.20}$$

where l^+ is the normalized length of the hot wires with $l^+ = lu_*/\nu$ with l being the length of the hot wire probe. They also reported that η, the Kolmogorov length scale remains almost constant in the inner and the overlap region. Since the filtering effect is higher in the wall region, l^+ scaling remains to be the feasible scaling parameter over η^+. Though the correction is defined for HWA probe length, the same analogy can be applied for a PIV measurement where the light sheet thickness or the interrogation window length in the wall-normal direction act similar to the probe length in HWA.

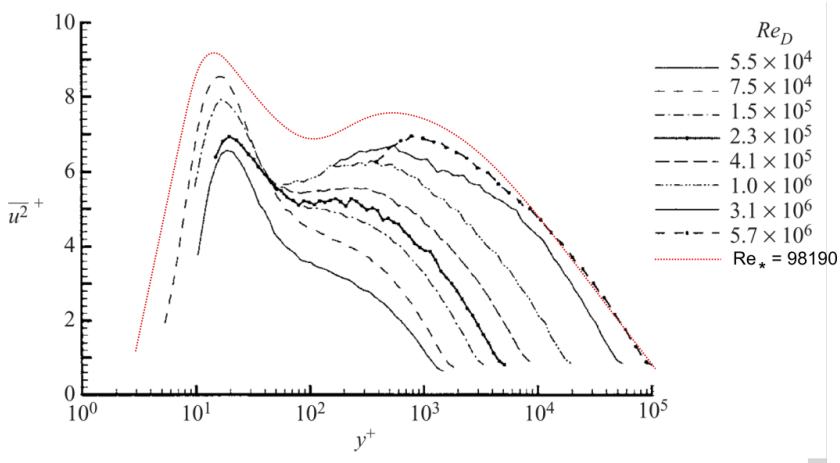

Figure 2.7: Inner-scaled streamwise turbulent fluctuations as observed by Morrison et al. [39]. The red line represents the fluctuations as observed by Vallikivi et al. [60].

2.3.2. Uncertainty in the *Von Kármán* constant

The variation in the value of κ is another unsettled issue faced while studying the wall turbulence. This arguably questions the universality of the constant. One of the factors for its variation is attributed to its dependency on the pressure gradient by Nagib et al. [41]. Figure 2.8 shows the variation of skin friction coefficient (C_f) with momentum-thickness Reynolds number for favourable (FPG), adverse (APG) , and zero (ZPG) pressure gradients. Skin friction coefficient and κ are related by [42],

$$C_f = 2\left(\frac{u_*}{u_0}\right)^2 \Rightarrow C_f = 2\frac{1}{\left(\frac{1}{\kappa}ln(y^+) + B\right)^2}. \tag{2.21}$$

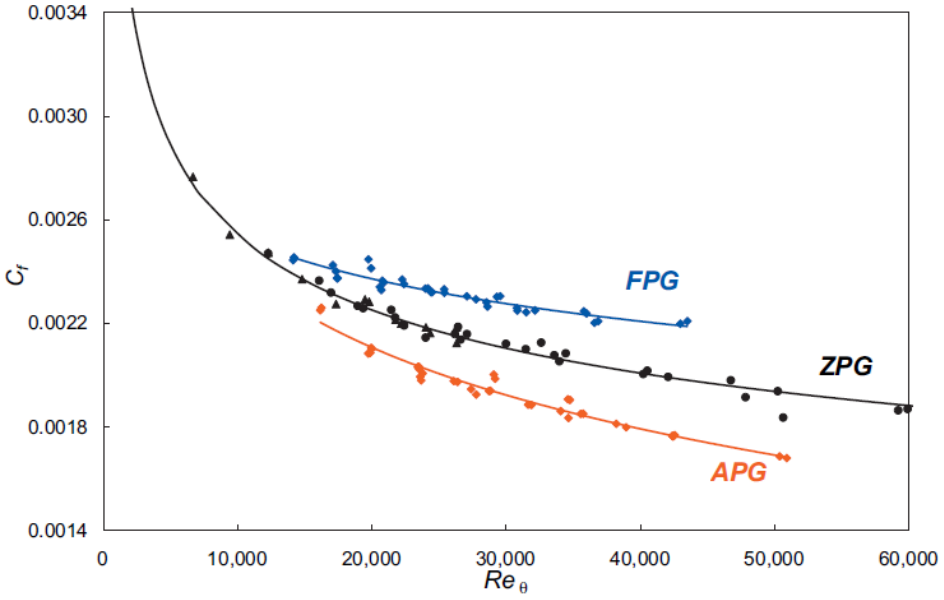

Figure 2.8: Variation of the skin friction with the pressure gradient for equilibrium boundary layers. FPG: favourable pressure gradient; ZPG: zero pressure gradient; APG: adverse pressure gradient [41] (taken from [31], Figure 10).

The flow over a channel exhibits variation in κ due to the role of the aspect ratio of the experimental facilities [31]. In the case of pipe flows, the Princeton Superpipe facility [20] and the Melbourne pipe facility Monty [37] report different values of κ with a value of 0.421 and 0.385 respectively. Nagib and Chauhan [40] estimated the variation of κ for pipes, channels and ZPG boundary layers using composite profiles. According to them, κ exhibits an asymptotic behavior with the Reynolds number reaching a constant value at high Reynolds numbers, as shown in Figure 2.9.

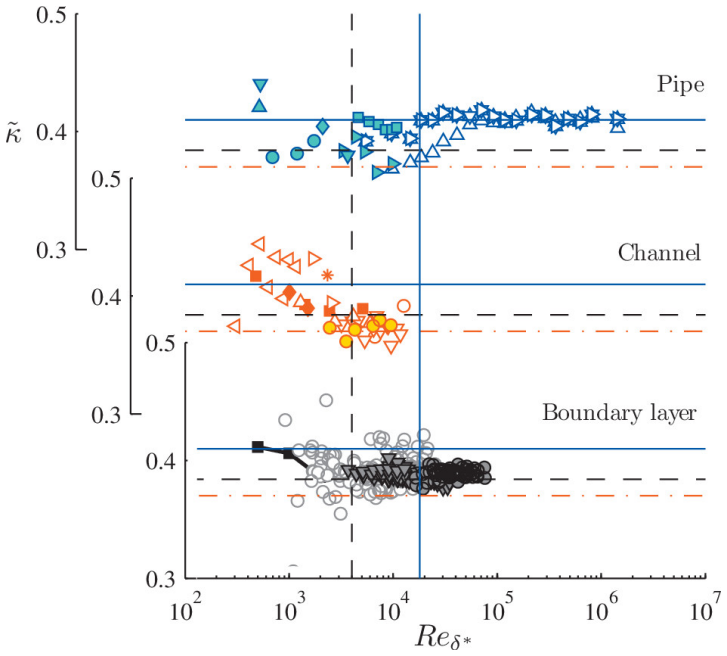

Figure 2.9: Variation of the *Von Kármán* constant, κ with Reynolds number for pipe, channel and boundary layer obtained by Nagib and Chauhan [40].

2.3.3. Roughness

The surface roughness plays an important role at high Reynolds numbers as even a well-polished surface appears to be rough because the viscous scale becomes sufficiently small. The universal resistance plots in the form of the well-known *Moody* chart provides the variation of friction factor for different values of surface roughness (ϵ) expressed in terms of relative roughness (ϵ/d) . The *Moody* chart (Appendix B) relates the *Darcy Weisbach* friction factor (f_D), the Reynolds number (Re), and the relative surface roughness for fully developed flow in a pipe. The moody chart can be divided into two parts based on the flow regimes: laminar and turbulent flow. In the laminar regime (Re < 2100), the *Hagen-Poiseuille* equation (White et al. [67]) gives,

$$f_D = \frac{64}{Re}. \tag{2.22}$$

For turbulent flow, the friction factor is given by the Colebrook (Colebrook and White [12]) expression,

$$\frac{1}{\sqrt{f_D}} = -2log_{10}\Big(\frac{\epsilon/d}{2.7} + \frac{2.51}{Re\sqrt{f_D}}\Big). \tag{2.23}$$

The friction factor can be used to determine the pressure drop of the fluid in a pipe (Δp) across a pipe length, L given by the relation,

$$\Delta p = f_D \frac{\rho u^2}{2} \frac{L}{d}. \tag{2.24}$$

Townsend [59] proposed that the effect of roughness on the outer flow is taken into account by considering friction velocity as the appropriate boundary condition at the wall. It is inherently assumed here that the boundary layer is considerably thicker than ϵ, the rms of the height of surface irregularities. Recent experiments in the Superpipe (Shockling et al. [53]) in hydrodynamically rough regime produce the same scaling laws for mean velocity and fluctuations in the outer region, as that of the results corresponding to a smooth wall. Morris et al. [38] ascertains this by reporting that the motions associated with the inclined hairpin packets at low Reynolds number develop even in flows bounded by a hydrodynamically rough surfaces.

Although the *Colebrook* expression predicts smooth transitional roughness behaviour, studies by Shockling et al. [53] on honed surfaces, and studies by Langelandsvik et al. [30] on commercial steep pipe predict a well defined onset of roughness. Langelandsvik et al. [30] observed an abrupt change in the friction factor curves with attaining fully rough regime over a relatively small interval of Reynolds number. However, they predict a monotonic curve in contrast with that observed in honed surface [53], where an inflectional trough is observed in the transitional regime.

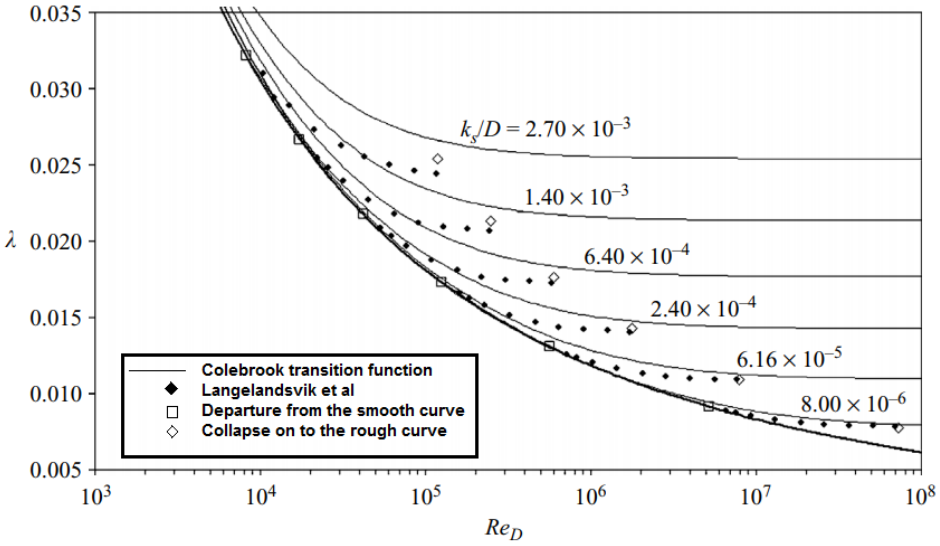

Figure 2.10: Friction factor (λ in figure) diagram for welded commercial steel pipe as proposed by Langelandsvik et al. [30].

The issues presented so far motivates to perform experiments to contribute to the research in the wall turbulence at high Reynolds numbers. A detailed explanation of all the issues in a high Reynolds number wall bounded flows is out of scope of the current study and the readers are recommended to refer Adrian [4], Marusic et al. [31], and Vallikivi et al. [60] for further details. Any attempt to study such flows require high spatial resolution. PIV has not been used extensively at such Reynolds number with Willert et al. [68] being one of the few to attempt to study high Reynolds number wall turbulence. The current study attempt to use PIV with the ensemble correlation approach and study the wall turbulence at high Reynolds number pipe flow. The observations in the near wall region are presented in Chapter 5.

3

Statistical parameters of ensemble correlation

As mentioned in Chapter 1, one of the ways to improve the spatial resolution of PIV is to time-average the individual correlation functions. The resolution can be as high as one pixel, as shown by Westerweel et al. [66]. Since its development, the signal to noise ratio of relatively smaller interrogation windows have been significantly improved but they are still not commonly used for high speed flows as averaging causes loss of instantaneous information. However, Scharnowski et al. [51] showcased that the statistical variables can be extracted from the shape of the ensemble correlation peak. In this chapter, the analytical description of relation between the different statistical quantities and the shape of the ensemble correlation is explained assuming ideal conditions. The analytical description is based on the work of different authors: Westerweel [64], Adrian and Westerweel [5], Scharnowski et al. [51], and Strobl [58]. Further, methods to retrieve the joint probability distribution functions (JPDFs) of velocity from the averaged correlation functions are discussed. Lastly, the sensitivity of the method to noise in the correlation and the methods followed to reduce the noise are discussed.

3.1. Statistical description of PIV

This section presents a brief review of the analytical description of PIV. The intention is to develop a basis for understanding the relation between the ensemble correlation and the velocity JPDFs. To keep the expressions simple, ideal conditions are considered. Important assumptions made are:

1. Ideal tracer particles: Particles are assumed to be of same size and are perfect spheres in complete focus. They are assumed to be homogeneously distributed and to perfectly follow the flow.
2. Light sheet: The light sheet is assumed to be infinitely thin, with the optical axis normal to the light sheet plane. The illumination is assumed to be homogeneous. The errors in the lenses are neglected. The two exposures of the light sheet occur in the same plane.

One these grounds, the displacement field $\vec{S}(\vec{X}, \Delta t)$ can be defined as the distance traveled by a tracer particle located at a position $\vec{X}$ initially, in a time interval Δt due to the flow velocity field $\vec{v}(\vec{X}, t)$.

$$\vec{S}(\vec{X}, \Delta t) = \int_{t}^{t+\Delta t} \vec{v}(\vec{X}(t), t) dt. \tag{3.1}$$

Assuming that the particles are distributed homogeneously in the positions given by x_{tracer} in the object plane, the particle positions can be specified as a Dirac delta peaks given as,

$$g(x,t) = \delta(x - x_{tracer}(t)). \tag{3.2}$$

Based on this, the intensity pattern $I(x)$ of the image of the particles can be expressed by the convolution of the image intensity pattern of an ideal particle, $I_{ideal}(x)$ and the position of the particles, $W(x)$.

$$I(x,t) = \int g(\eta) I_{ideal}(x - \eta) d\eta. \tag{3.3}$$

The image exposure of a single particle, $I_{ideal}(x)$ (Equation (3.6)) depends on the total energy in the light pulse (say J_O), the size of aperture, the scattering of the light, and the thickness of the light sheet (Adrian and Westerweel [5]). In reality, the particles are distributed over a volume of fluid and all the particles illuminated by the light sheet regardless of whether they are in the object plane or not, will create images on the image plane with some in focus and some out of focus. The particles have finite diameter and the image diameter of the particle is not just dependent on its finite particle diameter but also on the effects of the geometric lens aberrations and the diffraction. The effective image diameter is given by,

$$d_{image} \approx \sqrt{(M_o d_p)^2 + d_d^2 + d_a^2}, \tag{3.4}$$

where M_o is the magnification of the lens, d_p is the finite particle size, d_a is the diameter of the aberrated image of a point source and, d_d is the *diffraction-limited spot diameter* [5] given by,

$$d_d = 2.44(1 + M_o)\, f^{\#} \lambda, \tag{3.5}$$

with λ as the wavelength of the light and $f^{\#}$ = f/D_a as the f-number of the lens, where f is the focal length of the lens, and D_a is the diameter of the lens aperture.

The images of the particle filled fluid are taken at two instants, t and t + Δt, and are interrogated to estimate the displacement field which has information on the velocity of the flow given by Equation (3.1). This technique is generally referred as image interrogation. Images are recorded generally in a single-pulsed, double frame system with a dual-cavity laser. The two image intensities can be expressed as,

$$I_1(x) = I(X,t) = \int J(z) \tau_o [X - F(x)] g(x,t) dx, \tag{3.6}$$

$$I_2(x) = I(X, t + \Delta t) = \int J(z) \tau_o [X - F(x)] g(x, t + \Delta t) dx. \tag{3.7}$$

where τ_o represents the exposure of a particle image per unit of illumination beam intensity $J(z)$ with the object plane at z = 0. $F(x)$ maps the object points to the image points. There are different interrogation techniques based on the type of PIV and the concentration of the particles in the flow [5]. For the current study, a planar and high image density PIV is used and hence, the analytical description of this technique is explained in the further sections.

3.2. Spatial cross-correlation of images

The images obtained at two instants have to be interrogated to obtain the displacement field as the primary deliverable. This is achieved by cross-correlating the two image pairs with

intensities I_1 and I_2 respectively. It is a statistical approach to determine the most probable displacement of particles, specifically a group of particles during a small instance of Δt. This is achieved by finding the possible matches of all the particles present in the first image with the particles in the second image. Large images are decomposed to smaller interrogation windows. The cross-correlation estimator for an interrogation window, say W_1 is a function of position and time and is given by,

$$R(s,t) = \int_{W_1} I_1(x,t) I_2(x+s,t) dx. \tag{3.8}$$

This function has a sharp maximum in the s-plane (Figure 3.1), corresponding to the displacement between the two images, say ΔX_p. The maximum occurs when the second image is shifted with respect to the first image by $s_D = \Delta X_p$, such that the second image most probably overlaps the first image. Thus, identifying this image displacement is equivalent to identifying the most probable displacement of the particles. In practise, not every particle moves with the same velocity, hence the displacement obtained is averaged over particles contained in an interrogation window.

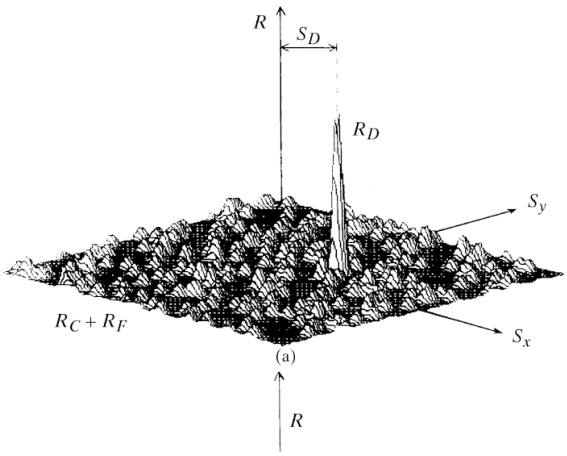

Figure 3.1: Cross-correlation of a single-pulsed, double frame images (Keane and Adrian [26], Figure 2a).

Apart from the maximum peak in the cross-correlation function, there are other peaks which represent the correlation of a particle with the other particles in the image pair. These peaks are thus considered as noise, and as a measure of the quality of the cross-correlation function, a *signal-to-noise* (SNR) is defined. It is defined as the ratio of the height of the maximum peak to the height of the second largest peak. This ratio is a function of number of particles as the maximum corresponds to the overlap of maximum number of particles. Another interpretation of SNR is that it gives a measure of perfect matches of the particles in the windows W_1 and W_2. It is important to note that Figure 3.1 corresponds to the interrogation of two images after subtracting their respective mean intensity fields. The effect of this operation is explained later (Figure 3.3).

Every particle present in an interrogation window need not be present in the second window. Some particles enter and leave the light sheet perpendicular to the plane of light sheet between successive exposures, commonly referred as losses due to *out-of-plane* motion of the particles. The fractional loss in the particles due to such motions are denoted by a factor, F_O. In addition to this, new particles enter and old particles exit the interrogation window W_2

compared to W_1 in the plane of light sheet. These loses are due to the *in-plane* motion of particles. The average particles available in both exposures are quantified by a mean fraction, denoted by F_I. In order to extract information efficiently from the cross-correlation, the *in-plane* losses are strictly constrained by the one-quarter [5] rule,

$$1 - F_I < 0.25. \tag{3.9}$$

However, the *in-plane* loss can be reduced, even completely removed in principle by choosing a bigger second window (at t + Δt) such that the particles in the first window are completely present in the second window (Landreth and Adrian [29]). More details on description of cross-correlation function and other practical considerations are given by Adrian and Westerweel [5], and Keane and Adrian [26].

The cross-correlation function can be decomposed into different components based on the nature of the recording of the image. *Single-exposure multiple-frame* recording produces subsequent exposures on separate frames. As explained earlier, the recorded signals have an image pattern given by Equation (3.3). The two exposures can be expressed as a combination of mean and fluctuating intensity fields.

$$I_1(X) = \overline{I_1} + \Delta I_1(X) \; and \; I_2(X) = \overline{I_2} + \Delta I_2(X). \tag{3.10}$$

where $\bar{I}$ represents the mean intensity and the ΔIs are the fluctuating intensity fields with $\overline{\Delta I} = 0$. Based on this, the correlation can be divided into three components [5] given by

$$R(s) = R_c(s) + R_F(s) + R_D(s), \tag{3.11}$$

$$R_c(s) = \int W_1(X) W_2(X+s) \overline{I_1} \; \overline{I_2} dX, \tag{3.12}$$

$$R_F(s) = \int W_1(X) W_2(X+s) [\overline{I_1} \Delta I_2(X+s) + \overline{I_2} \Delta I_1(X)] dX, \tag{3.13}$$

$$R_D(s) = \int W_1(X) W_2(X+s) \Delta I_1(X) \Delta I_2(X+s) dX. \tag{3.14}$$

where R_c is the correlation of the mean background intensity over the interrogation windows W_1 and W_2, R_F is the cross-correlation of the mean intensity in the first window and the fluctuating intensity field in the second window and vice versa. R_D represents the cross-correlation of the fluctuating intensity field in the two windows W_1 and W_2. This is pictorially depicted in Figure 3.2. The component R_D also contains random correlation peaks which can be eliminated by ensemble averaging the spatial correlation functions of all possible realizations of the tracer pattern in the fluid for a given fixed flow field [5]. The terms R_c and R_F contain mean intensity field which does not contribute to the displacement of the particles. Subtracting the local mean intensities from the image intensity field of an exposure, prior to the computation of the spatial cross-correlation effectively eliminates both R_c and R_F. The general image normalization followed before estimating the cross-correlation function is given by Equation (3.15), which is the removal of mean intensity from the image intensity field followed by dividing the image with its standard deviation ($\sigma_I(x)$).

$$s_I = \frac{I(X) - \overline{I(X)}}{\sigma_{I(X)}}. \tag{3.15}$$

This normalization would effectively remove the contribution of the mean intensity, thereby directly resulting in R_D. Thus, the normalized R_D has a mean value of zero. This is shown in

Figure 3.3. The strong peak corresponds to the displacement of the particles in an interval Δt, with noise fluctuating between positive and negative values.

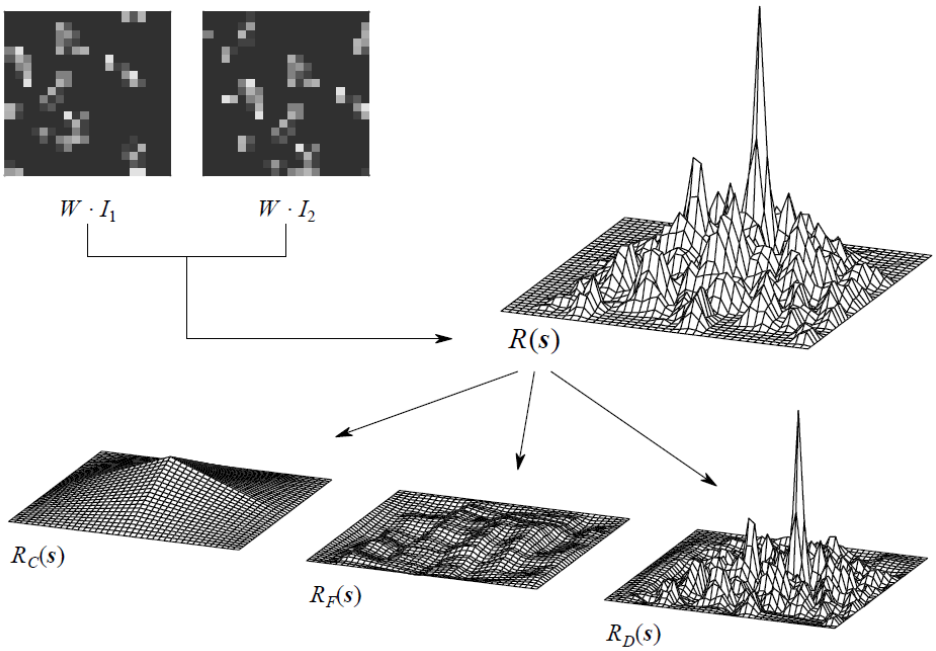

Figure 3.2: Spatial cross-correlation of two single-exposure images. Depicts the components of $R(s)$: R_c, R_F, and R_D (Westerweel et al. [66], Figure 8.3).

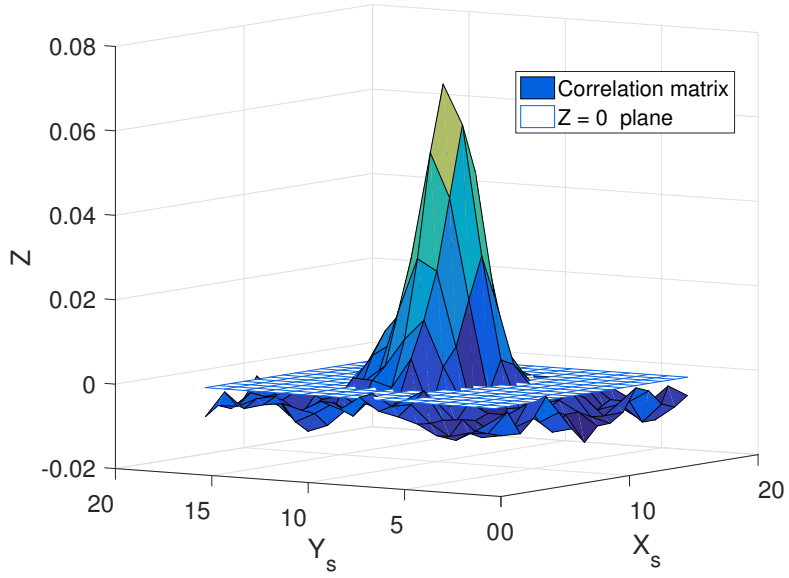

Figure 3.3: Ensemble cross-correlation matrix (using 3000 image pairs) positioned such that spatial average of the matrix is zero. This is due to subtracting the mean image intensity from the images correlated.

3.3. Ensemble correlation up to single pixel resolution

3.3.1. Ensemble correlation

The SNR of the correlation function is often increased by superposition of correlation functions of subsequent image pairs. The particle image density in an image is limited by effects like interference patterns [5]. Averaging the correlation functions can also be interpreted as increasing the particle density of the image without actually over-seeding the fluid. Such an operation that involves superposition of the cross-correlation data produces a strong displacement correlation peak with an amplitude proportional to the number of PIV image pairs used for superposition [64]. There is also loss of information due to F_1 and F_O. The ensemble correlation (R_{avg}) can be generalized as,

$$R_{avg} = NF_1F_OF_\Delta, \tag{3.16}$$

where F_Δ accounts for the loss due to the local variation of displacement field. If there are N image pairs, then the ensemble correlation (R_{avg}) can be obtained from the individual correlations (R_D) as,

$$R_{avg} = \frac{1}{N}\sum_{n=1}^{N} R_D^{(n)}. \tag{3.17}$$

The image pairs are all normalized as mentioned before (Equation (3.15)), effectively eliminating any contribution from the mean intensities. Figure 3.4 shows a typical cross-correlation of an image pair, and the ensemble correlation corresponding to the same position. The ensemble correlation function, R_{avg} is a time averaged quantity and does not contain instantaneous information.

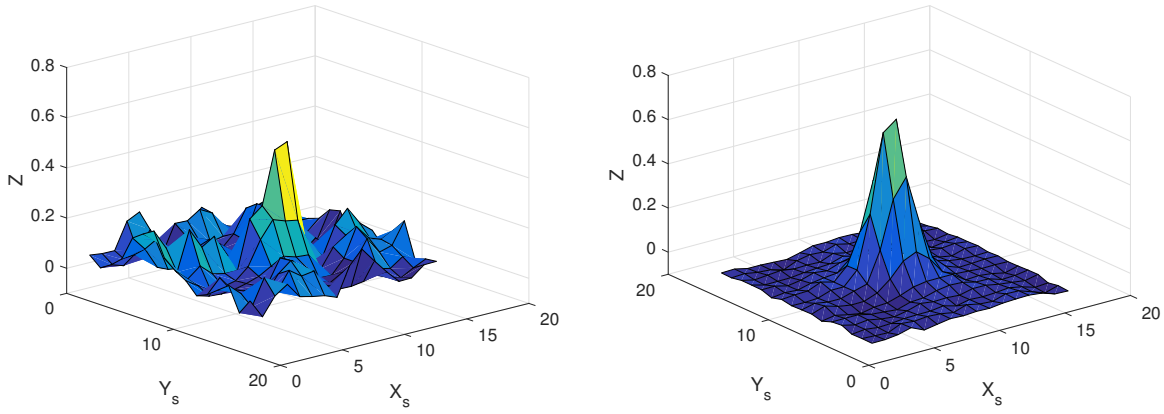

Figure 3.4: (a) 16 x 16 correlation matrix of an image pair (b) 16 x 16 ensemble correlation using 3000 image pairs, both corresponding to the same interrogation window.

3.3.2. Single Pixel Ensemble Correlation (SPE)

The increase in SNR of the ensemble correlation function gives a platform wherein, the interrogation window size of the PIV images can be decreased to a value from which sensible information can still be retrieved (achieving required image density). Since the height of displacement peak is proportional to the number of images, the spatial resolution can be increased up to single pixel by increasing the ensemble size. Such high resolution allows to capture steep velocity gradients and obtain unbiased velocity measurements at the vicinity of

the flow boundaries [23]. This method was first demonstrated by Westerweel et al. [66] where this technique was used to study the boundary layer in a micro channel. Unlike interrogating over a region, single-pixel correlation uses a two point correlation estimator defined by,

$$R^*(s) = \frac{1}{N}\sum_{i=1}^{N} I_1^{(i)}(X) I_2^{(i)}(X+s). \tag{3.18}$$

The working of the SPE compared to the conventional PIV interrogation is pictorially depicted in Figure 3.5. This method can be viewed as an extreme implementation of the ensemble correlation in which the smallest window has been reduced to single pixel. This technique requires a large number of images to produce a sensible displacement peak. A single pixel resolution would mean each pixel would contribute to the displacement measurement. Thus, the number of truly independent displacement vectors would be determined by the total number of pixels used for correlation divided by the particle image area in pixel units.

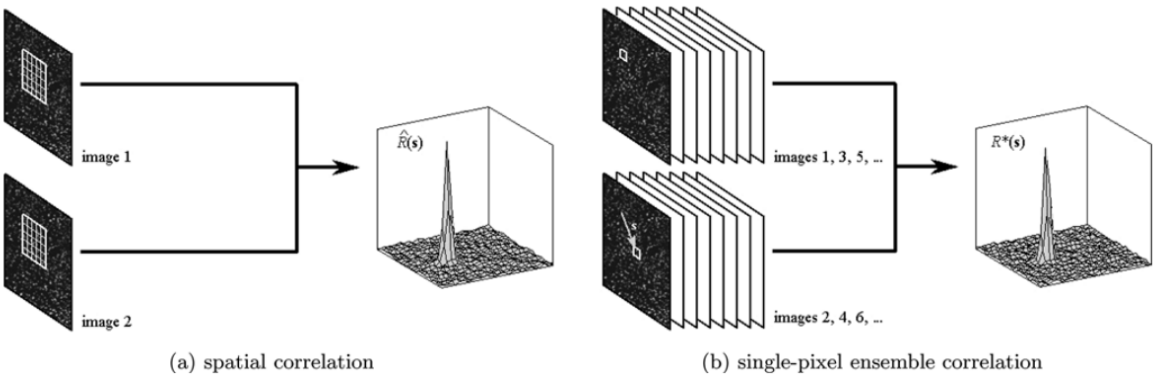

Figure 3.5: (a) NxN interrogation window of a single image pair of the conventional PIV spatial correlation, (b) 1-pixel domains avergaed over multiple image pairs of a single pixel correlation (Westerweel et al. [66], Figure 1a).

The ensemble correlation and SPE are obtained by averaging the individual correlation functions obtained at different instants. This means the instantaneous information of the flow studied is lost when statistically averaged over time. This has been a strong inhibitor in using ensemble correlation approach in many unsteady flow applications. The application and information of SPE has evolved over time as enumerated,

- *Stationary flows*: The single pixel correlation PIV was introduced by Westerweel et al. [66] in a stationary micro channel flow. The flow is not anymore a function of time and thus, SPE strongly improves the image density in the micro channel with low particle density.
- *Periodic flow*: Billy et al. [8] extended the single pixel correlation technique to periodic flows by using it for studying the Poiseuille flow in a small grooved channel.
- *Turbulent flows*: The SPE was used on fully turbulent flows by Kähler et al. [22]. By applying the technique using synthetic images, the ensemble correlation was found to broaden with the level of turbulence. The size of the peak was used to determine the velocity PDFs.
- *Turbulent flow - velocity JPDFs*: Scharnowski et al. [51] showed that the information on the velocity joint probability distribution functions (JPDFs) can be retrieved from the

shape of the ensemble correlation function. This approach is explained in detail in the next section.

Since turbulence broadens the correlation function, the velocity fluctuations can be estimated if the broadening can be backtracked to the velocity fluctuations. Keane and Adrian [25] reported that in presence of shear, the amplitude of the correlation peak decreases and the shape peak is broadened in the direction of the shear. Kähler et al. [22] reported that the statistical variables can be extracted from the shape of the ensemble correlation peak. The ensemble correlation produces biased displacement fields due to asymmetrical particle image distribution resulting in distorted correlation. This was shown analytically by Westerweel [64] for simple shear and uni-axial stress cases. Furthermore, velocity gradients also reduce the amplitude of the displacement peak. Recently, Scharnowski et al. [51] extracted the statistical variables of the flow from the shape of the single pixel correlation peaks. This is explained in detail in the next section.

3.4. Retrieving the velocity JPDFs from the ensemble cross-correlation

3.4.1. Relation between the velocity JPDFs and the correlation function

Assuming ideal conditions, the two exposures of an image pair, I_1 and I_2 can be assumed to have the same particle image pattern with the second exposure shifted by a displacement vector, S(x,t). It is assumed that the instantaneous cross-correlation of two interrogation windows is an estimator for the two point ensemble correlation. Thus, the image intensity field of the second exposure can be described by the intensity field of the first exposure shifted by the velocity vector given by, $\overline{v} = \frac{S(x,t)}{\Delta t}$. In order to represent this shift mathematically, a Dirac Delta function, $\delta(a-b)$ can be defined which has the following property (Chakraborty [9]),

$$h(a) = \int h(x)\delta(x-a)dx \; = \int h(x)\delta(a-x)dx \; = \int h(x)\delta(a-q(x))dx. \tag{3.19}$$

where $q(x)$ and $h(x)$ are arbitrary functions. The image intensity pattern of the second exposure can be expressed in terms of the intensity pattern of the first image as (Strobl [58]),

$$I_2(x) = \int I_1(x)\delta(x - S_v(x',t))dx' = (I_1 * \delta_{S_v})(x,t). \tag{3.20}$$

where $S_v(x',t) = x' + S(x',t)$. Here $'*'$ is the convolution integral. The images considered in this section are normalized, and I_1 & I_2 contain only the intensity fluctuations, say I_1' and I_2' respectively, thereby eliminating the R_C and the R_F components from the correlation function (Equation (3.11)). Thus, R_D containing information on the displacement of the particles across Δt can be expressed (based on Equation (3.8)) as,

$$R_D(s,t) = I_1' * (I_1' * \delta_{S_v})(s,t). \tag{3.21}$$

Since convolution is an associative operator, the expression in Equation (3.21) can be written as

$$R_D(s) = (I_1'^2 * \delta_v)(s,t) = \int I_1'^2(x',t)\delta(s - S_v(x',t))dx'. \tag{3.22}$$

where $I_1'^2(x',t) = \int I_1'(x,t)I_1'(x'-x,t)dx$. $I_1'^2(x',t)$ is the auto-correlation function of the intensity fluctuations of the first image. Equation (3.22) can also be written as,

$$R_D(s) = \int I_1'^2(x',t)\delta(s-x'-S(x',t))dx'. \tag{3.23}$$

Since the displacements between the two exposures can be represented in terms of velocity in a PIV system for a short interval Δt, the above equation can also be represented as

$$R_D(s) = \int I_1'^2(x',t)\delta(\frac{S(s-x',t)}{\Delta t}-v)dx'. \tag{3.24}$$

According to Pope [47], discrete PDF can be represented as,

$$f_n(V) = \frac{1}{N}\sum_{n=1}^{N}\delta(u^{(n)}-v). \tag{3.25}$$

where $u^{(n)}$ is the velocity of n^{th} realization of the flow and N is the ensemble size. If this equation is written as a continuous function ($\frac{1}{\delta V}\int_{\delta V}\delta(s-S(x'))dx'$), then the derivative of the JPDFs as a function of the number of ensemble sample would be, $f'(v;x,t) = \delta(\frac{S(x,t)}{\Delta t}-v)$. Substituting this in Equation (3.24) results in,

$$R_D(s) = \int < I_1'(x,t)I_1'(x'-x,t)f'(v;s-x',t) > dx'. \tag{3.26}$$

Thus, from the above equations, it is evident that the JPDFs of velocity is stored in the correlation function. *This information is contained such that the ensemble correlation function is the convolution of the auto-correlation function and the velocity PDF.*

In reality, the ensemble correlation over a finite volume can only be approximated as the convolution of the auto-correlation function and the velocity JPDFs. The volume (say δV) of the interrogation window is limited by the size of the window in two directions, and the thickness of the light sheet. Also, the single displacement value represented by the δ-function in Equation (3.21) is replaced by a displacement distribution function, $F_\Delta(s)$. Thus, the aforementioned relation can be expressed as (Westerweel [64]),

$$R_{avg} \approx I_1'^2\tau_{00}NF_1F_O(F_\tau * F_\Delta(s)), \tag{3.27}$$

where '*' is the convolution integral, τ_{00} is the average exposure of the laser light, N is the number of image pairs interrogated, and F_τ is the auto-correlation function over volume δV. Thus, the displacement field is not anymore an unique function, but refers to the maximum of $F_\Delta(s)$ representing the most probable displacement of particles inside the volume δ. According to Westerweel [64], velocity gradients decreases the amplitude of the correlation peak and broadens the displacement-correlation peak. It is the intention of this study to use the information on the broadening of the peak to estimate the velocity JPDFs.

3.4.2. Recognizing the velocity JPDFs in the ensemble correlation function

The relation between the ensemble correlation function, the auto-correlation function, and the velocity JPDFs is derived in the previous sub-section. This relation is the basis for this thesis study. Obtaining an ensemble correlation function, given the auto-correlation function and the velocity JPDFs is a straightforward task that involves direct convolution of the the two functions assuming ideal conditions. However in reality, the ensemble correlation function and the auto correlation function are the deliverables from a PIV analysis and the important

objective is to retrieve the velocity JPDFs of the flow. This, in contrast is very difficult operation as the inverse of the convolution operation, generally referred to as '*deconvolution*' operation is mathematically and statistically very complex and there are numerous unsuccessful attempts in the past [58]. In this study, the direct *deconvolution* is not attempted. However, numerous work have been done on *deconvolution* algorithms in the field of Astronomy (Starck et al. [57]).

A direct deconvolution is avoided by estimating the statistical moments of the ensemble correlation [51]. The simplified form of Equation (3.24) can be written as,

$$R_D(s) = \int I_1'^2(x) f(v; s-x) dx, \tag{3.28}$$

It is inherently assumed that all particles in the first exposure are contained in the second exposure. This equation when transformed in the Fourier space, yields the following result,

$$R_D^f(s) = \alpha(s)\phi(s), \tag{3.29}$$

where $R_D^f(s)$, $\alpha(s)$ and $\phi(s)$ are Fourier transforms of the ensemble correlation function, the auto-correlation function and the velocity JPDFs respectively. Thus, the convolution operation (Equation (3.28)) is simplified to a simple product of the two terms on the RHS of Equation (3.29) in the Fourier space. The PDF of any variable a, $f(a;x)$ and its characteristic function $\xi(s)$ form a Fourier pair with,

$$f(a;x) = \frac{1}{2\pi}\int \xi(s) e^{-ixs} ds. \tag{3.30}$$

The k^{th} raw moment of any PDF (say f(a; x)) can be defined as the k^{th} derivative of its characteristic function (ξ(s)) at position s = 0.

$$M^k = \frac{d^k \xi(s)}{ds^k}\Big|_{s=0} (-i)^k. \tag{3.31}$$

Applying this to the ensemble correlation function $R_D^f(s)$,

$$M_R^k = \frac{d^k R_D^f(s)}{ds^k}\Big|_{s=0} (-i)^k = \frac{d^k \phi(s)\alpha(s)}{ds^k}\Big|_{s=0} (-1)^k. \tag{3.32}$$

The current work aims at demonstrating this technique to retrieve the second moments of the velocity JPDFs, Thus, taking k=2, and expanding the second derivative,

$$M_R^2 = \underbrace{\phi(0)}_{=1} \underbrace{\frac{\partial^2 \alpha}{\partial s^2}\Big|_{s=0}}_{=M^2_{auto}} + \underbrace{\alpha(0)}_{=1} \underbrace{\frac{\partial^2 \phi}{\partial s^2}\Big|_{s=0}}_{=M^2_{pdf}} - 2 \underbrace{\frac{\partial \phi}{\partial s}\Big|_{s=0}}_{=M^1_{pdf}} \underbrace{\frac{\partial \alpha}{\partial s}\Big|_{s=0}}_{=M^1_{auto}}, \tag{3.33}$$

$$= M^2_{pdf} + M^2_{auto}. \tag{3.34}$$

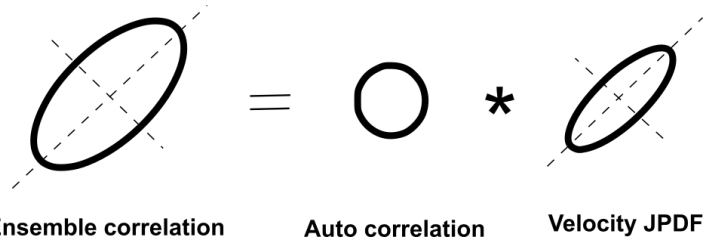

Figure 3.6: Relation between the ensemble correlation function, the auto correlation function and the velocity JPDFs.

Equation (3.33) simplifies to Equation (3.34) because the first moments of the auto-correlation and ensemble correlation function (M^1) is equal to zero. The moments of the ensemble and auto-correlation function can be estimated by two methods:

- Fitting a Gaussian profile to the correlation functions and determining the moments of the Gaussian fit function. This approach is less susceptible to noise in the correlation functions.
- Directly estimating the moments of the correlation matrices. This approach is accurate in theory, but requires clean correlation functions to give proper estimates.

The first method is used to estimate the moments in the current work. Strobl [58] used the direct-moment method primarily to estimate the moments. However, this approach is susceptible to noise in the correlation and moreover, the approximation considered in this approach is not valid anymore if the correlation does not follow a Gaussian profile. Hence, Gaussian fit approach is considered in this study to retrieve the velocity JPDFs. Fitting a Gaussian profile enables estimating the standard deviations of the ensemble correlation along two directions (say, X_s and Y_s) in the s-plane. The continuous Gaussian profile (say, G) can be represented by,

$$G = e^{-C(X^2+Y^2)}. \tag{3.35}$$

where C is a constant. X and Y are the major and minor axis of the elliptical cross section respectively. Fitting a Gaussian profile to the auto-correlation function leads to an estimate of the particle image diameter (say, d) with $d = \sqrt{2}X_{auto}$ (Warner [62]), where X_{auto} is the second moment of the auto-correlation with $X_{auto} = Y_{auto}$. If the standard deviations of the ensemble correlation function are represented by X_R and Y_R, and the standard deviations of the velocity JPDF are represented by X_{pdf} and Y_{pdf}, then according from Equation (3.34),

$$X_R = \sqrt{X_{pdf}^2 + X_{auto}^2}. \tag{3.36}$$

This is pictorially depicted in Figure 3.6. In reality, the ensemble correlation is affected by the in-plane and the out-of-plane losses [64] (Equation (3.27)). The second moments (X_{pdf} and Y_{pdf}) are thus, only an estimate for the velocity JPDFs.

3.5. Methodology

The PIV analysis is performed using the Matlab® routine as a part of PIVware tool, originated from the Aero and Hydrodynamics Laboratory, TU Delft. The ensemble correlation function and the auto-correlation function are estimated by taking the average of the correlation functions of individual frame pairs and the same images respectively. The moments of the averaged correlation functions are fit with a two-dimensional Gaussian centroid. This is achieved by using the in-built '*lsqcurvefit*' function. The interpolation scheme used is '*nearest*', which produces a maximum residual of 0.088 pixels while fitting. The fit requires specification of the position of the peak to produce an accurate estimate of the moments. Figure 3.8 shows an image of the Gaussian fit over the ensemble correlation function. The estimated velocity PDFs along the major and the minor axis are also shown in Figure.

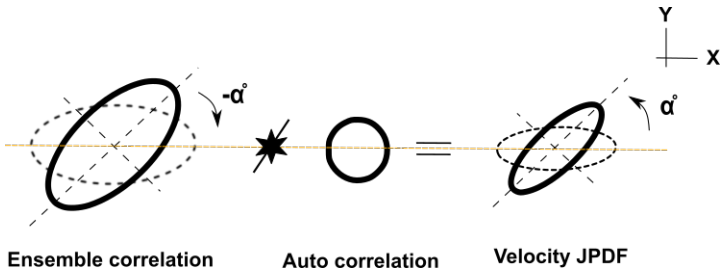

Figure 3.7: Method followed to retrieve the velocity JPDFs from the ensemble correlation function and the auto-correlation function. The symbol represents the deconvolution operation.

In order to perform the operation given by Equation (3.34), the Gaussian profile is fitted with both the ensemble correlation matrix and the auto-correlation matrix to obtain X_R, Y_R, and d. The ellipse obtained from the fit of the ensemble correlation matrix can however be rotated at a specific angle (α) dependent on the streamwise and span-wise velocity fluctuations. Thus, the ellipse fit is rotated such that it is aligned with Cartesian coordinates and the moments of auto-correlation function are subtracted from the rotated moments. The resultant is rotated again by the same angle (α) to find an estimate for the velocity fluctuations. This process is depicted in Figure 3.7. The velocity JPDFs and the ensemble correlation have the same orientation complying with the convolution operation. The corrections mentioned by Scharnowski et al. [51] for the difference in the orientation of the ensemble correlation and the velocity JPDFs are not considered in the current study. As mentioned before, only an estimate for the velocity JPDFs is obtained after correcting the second moments of the ensemble correlation with the second moments of the auto-correlation.

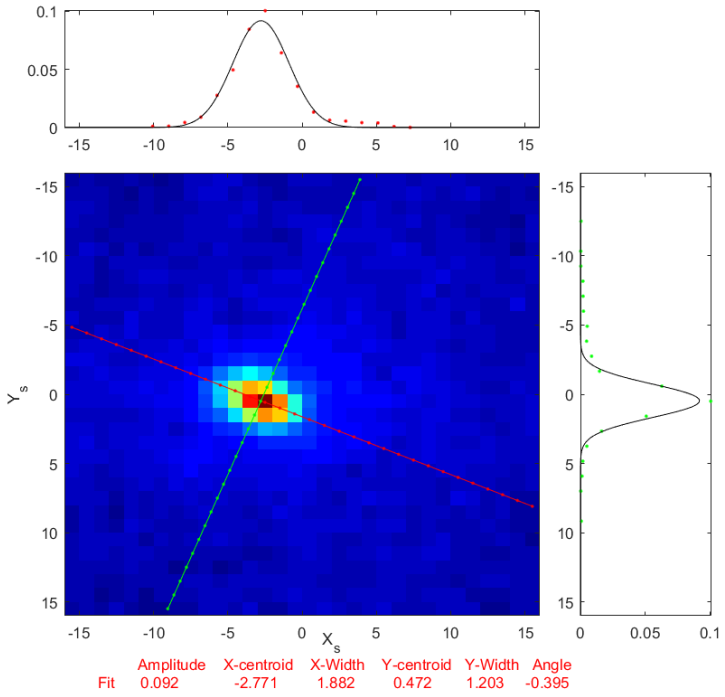

Figure 3.8: Probability density functions along major(top) and minor(right) axis of the ellipse formed by fitting a Gaussian profile to the ensemble correlation.

3.6. Sensitivity analysis

The Gaussian fit of the correlation function is sensitive to the noise in the function. The noise can produce bias in the estimates of the moment due to a bad fit. Thus in order to reduce the noise, the following two methods are carried out,

- Using a rectangular filter.
- Increasing the number of images used for ensemble correlation.

The sensitivity of the fit and hence the obtained moments to both of these operations are studied.

3.6.1. Effect of the rectangular filter

The noise in the ensemble correlation function can be reduced by using a rectangular filter, which takes the value of the unfiltered matrix in a m x n window and takes a value of '0' elsewhere. The first step is to separate the useful information and the noise in the correlation matrix. An ideal correlation matrix should only have a spread peak assuming a Gaussian profile corresponding to the moments of the correlation matrix. Away from the highest peak, the correlation matrix should have small values. Thus, in the real case, any peak away from the Gaussian spread of the highest peak can be considered as noise. The second step is to quantify how far away from the highest peak can the information be regarded as noise. In order to study this, different rectangular filter lengths are used and the variation in the residual of the fit and the moments of fit are studied. A sample analysis is described in this section. The correlation functions considered here correspond to a 16 x 16 interrogation windows of a turbulent jet flow. For simplicity, square filter lengths are employed in this study. Four filter lengths are used for this purpose: 5 x 5, 7 x 7, 9 x 9, 11 x 11 square filters in pixel units centered at the highest peak of the correlation matrix. The corresponding Gaussian fits are shown in Figure 3.12.

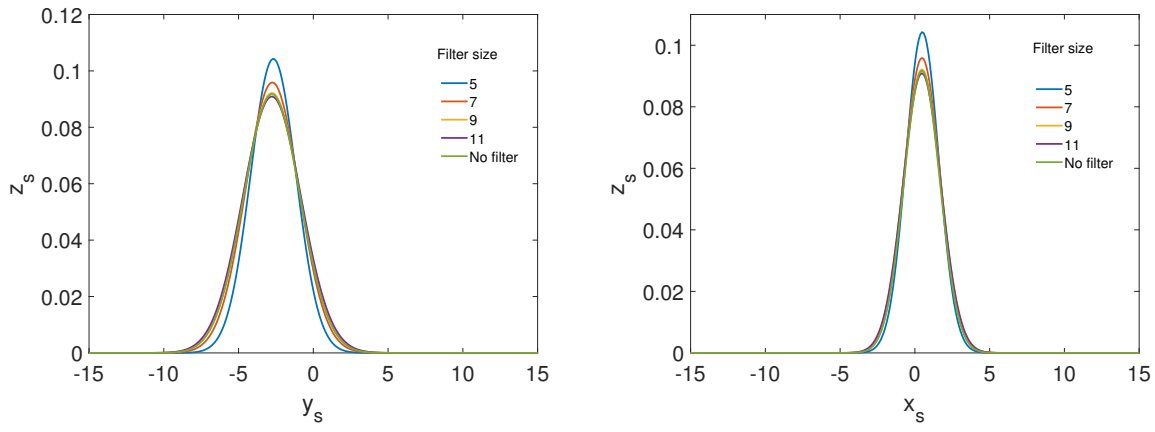

(a) PDF along major axis.

(b) PDF along minor axis.

Figure 3.9: Variation in the second moments of the Gaussian profile with the rectangular filter size.

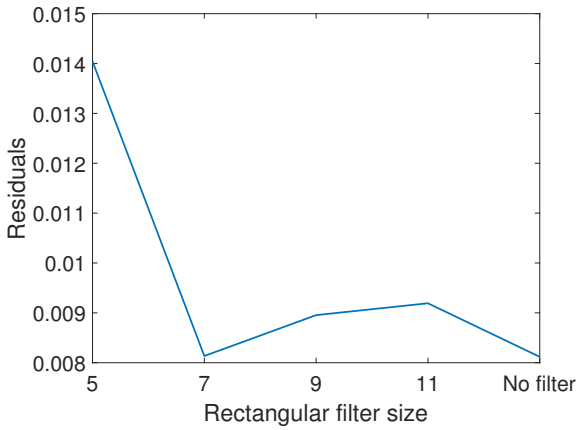

Figure 3.10: Residuals of the Gaussian fit function with the rectangular filter size.

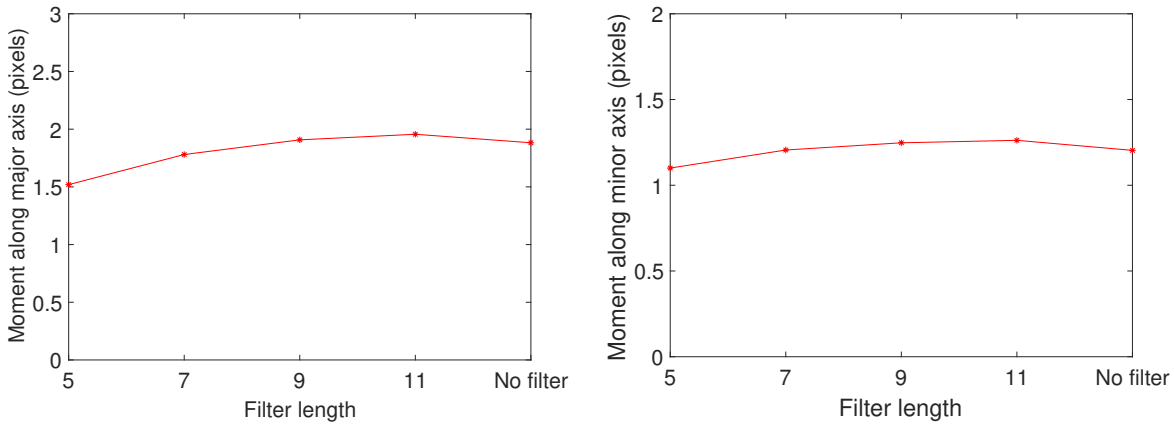

(a) Moment along major axis.

(b) Moment along minor axis.

Figure 3.11: Variation of second moments with the rectangular filter size.

Figure 3.12(a) shows the Gaussian fit (blue layer) and the corresponding raw correlation matrix (red mesh) without employing a rectangular filter. It is clear from this figure that there are areas where the Gaussian fit is not aligned with the ensemble correlation matrix completely. The residual of the fit is plotted in Figure 3.10 for different filter lengths. A strong SNR thus gives a low residual value for the unfiltered correlation matrix. The subsequent Figure 3.12(b), (c), (d) and (e) shows the Gaussian fits of the filtered matrices. The 5 x 5 filter provides a thin Gaussian profile as too much information has been filtered. Due to this, the residual of the fit (Figure 3.10) is higher. The residuals are lower for 7 x 7, 9 x 9, and 11 x 11 filter size and comparable with the residual of the unfiltered fit. Figure 3.9 depicts the change in the probability distribution functions along the major axis and the minor axis of the ellipse formed by the Gaussian fit. The spread of the Gaussian fit (in both directions) decreases with the filter size, with 5 x 5 filter producing a tall, steep, and reduced fit. As the size of the filter is increased, the spread of the PDF also increases. However, a 11 x 11 filter provides spread out fit with its width more than that of the unfiltered function (Figure 3.9). The corresponding change in the moments along two directions are shown in Figure 3.11.

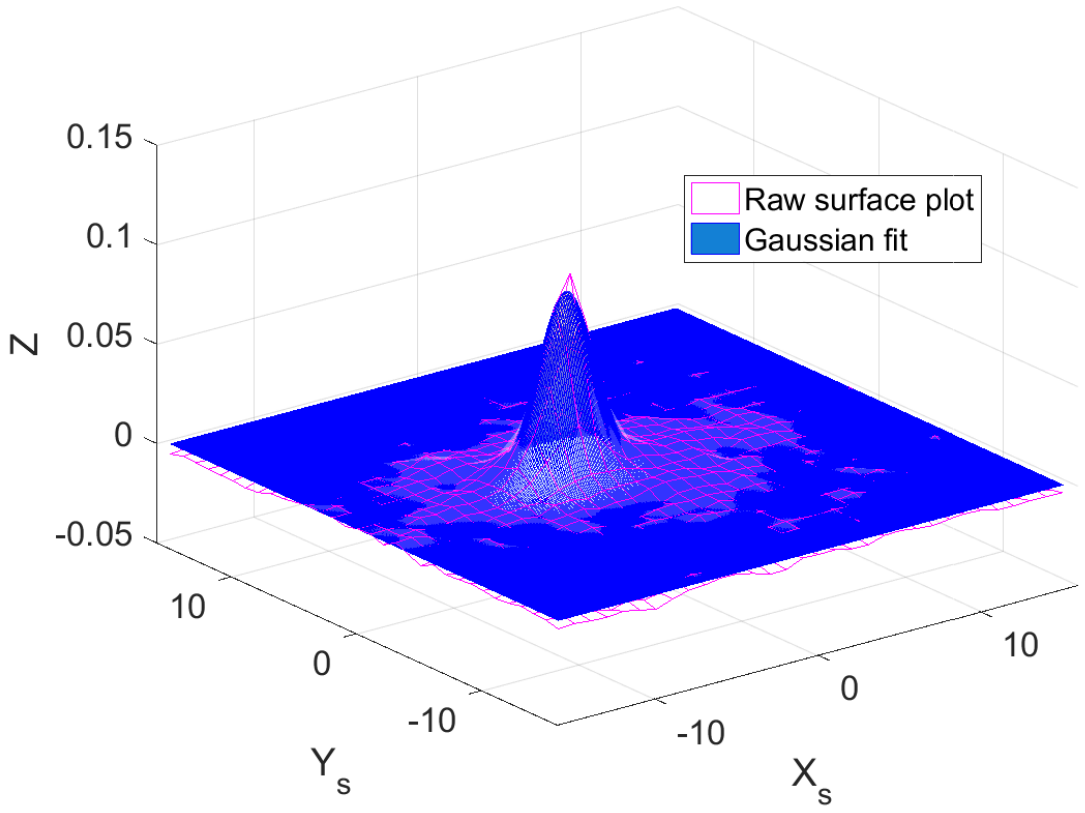

(a) Without using the rectangular filter.

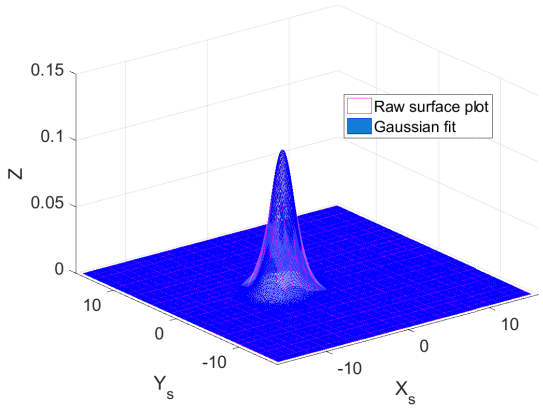

(b) Filter size: 5 x 5.

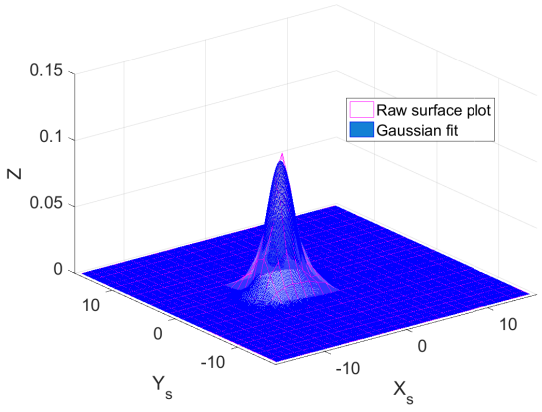

(c) Filter size: 7 x 7.

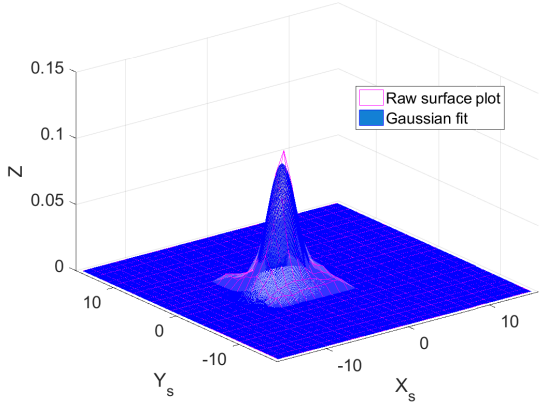

(d) Filter size: 9 x 9.

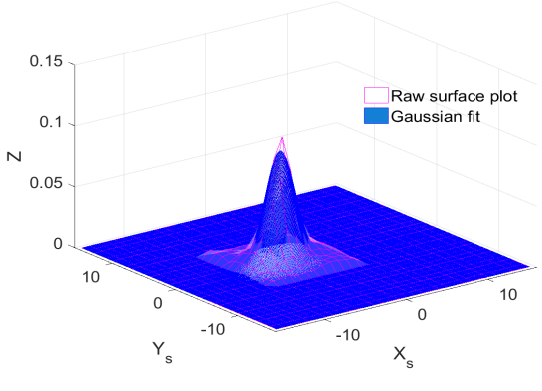

(e) Filter size: 11 x 11.

Figure 3.12: Gaussian fits and the corresponding raw correlation functions for different rectangular filter size.

3.6.2. Effect of number of images

The effect of the number of image pairs used to find the ensemble correlation can be interpreted as effective improvement in the image density. The effective image density is then proportional to the number of image pairs used for averaging. From Equation (3.27), it is evident that the amplitude of the ensemble correlation is directly proportional to the number of image pairs used. The increase in the signal strength is shown in Figure 3.13 using different number of image pairs. The information corresponds to a position inside the half-width of the turbulent jet flow. In order to retrieve the information on velocity JPDFs from the shape of the ensemble correlation, the noise has to be sufficiently low.

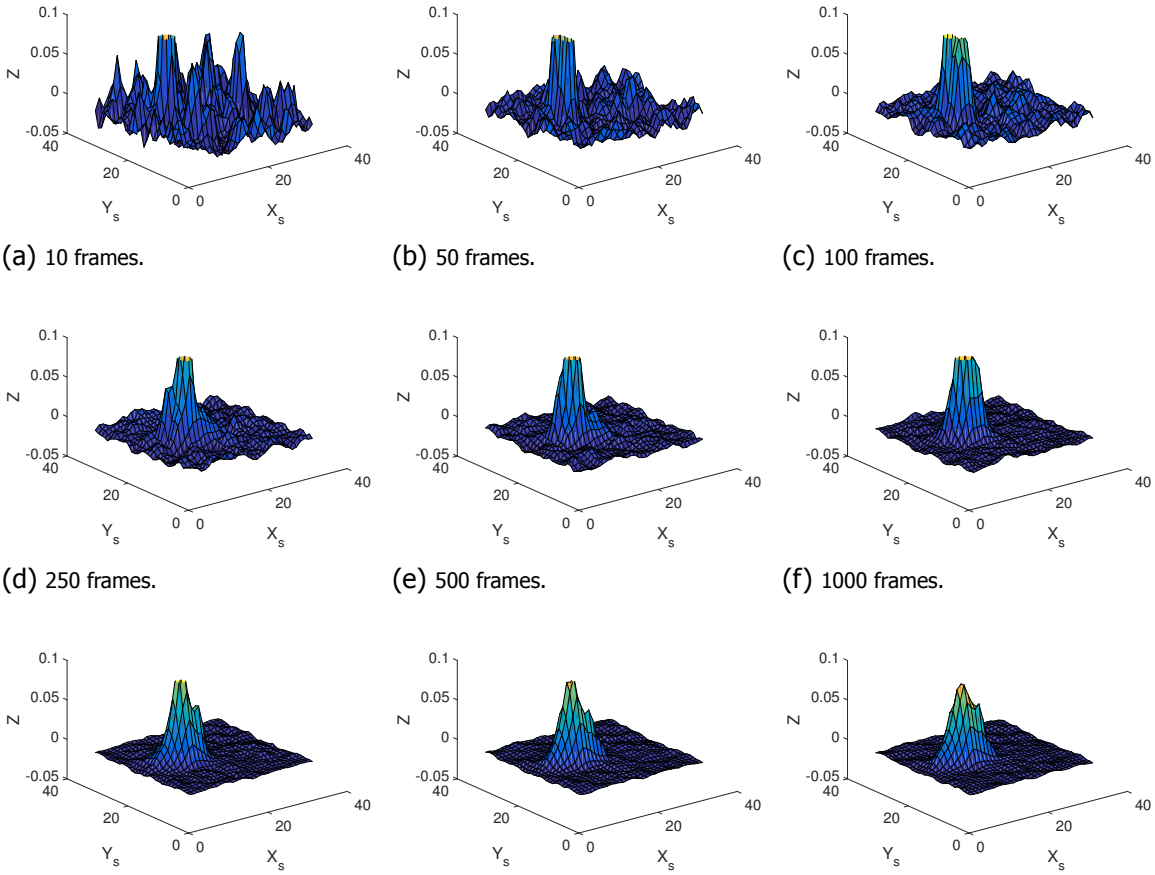

(a) 10 frames. (b) 50 frames. (c) 100 frames.

(d) 250 frames. (e) 500 frames. (f) 1000 frames.

(g) 2000 frames. (h) 3000 frames. (i) 4000 frames.

Figure 3.13: Ensemble correlation estimates using different number of frames corresponding to turbulent jet at a position inside the half-width of the jet.

4

Turbulent jet flow: experiment and validation

A PIV experiment to study a turbulent jet flow is performed. The intention of this experimental study is to apply the ensemble averaging technique explained in Chapter 3 to the recorded PIV images. The results obtained using this technique, are compared with the results from the conventional PIV analysis. Also, the results are validated with the turbulent jet experimental results from Westerweel et al. [65]. The ensemble correlation approach is also used to process the PIV data from Westerweel et al. [65] which contains 657 image pairs. In order to investigate the performance of the ensemble correlation, a scaled up turbulent jet model is set up and 9000 image pairs are recorded. In the first section, the setup from Westerweel et al. [65] is explained briefly, followed by the results obtained from the ensemble correlation of 657 image pairs. In the second section, the scaled up jet flow setup developed in the current work is explained in detail. Later, the results from the ensemble correlation technique and the conventional PIV processing are compared.

4.1. Turbulent jet setup: Westerweel et al. [65]

4.1.1. Experimental setup

The experiment by Westerweel et al. [65] involves conditionally sampled PIV measurements of a turbulent round submerged jet in a laboratory. The transport properties are studied at a jet Reynolds number of 2000 between 60 and 100 nozzle diameters from the jet nozzle.

The experimental setup consists of a rectangular test section of 110 x 110 x 300 mm^3. The jet fluid enters the test section as a fully developed pipe flow in laminar regime. The Reynolds number (*Re*) is maintained at 2000, implying a nozzle exit velocity of 2 m/s. The fluid is seeded with 5 μm tracer particles. In order to avoid interference of recirculation flow field on the jet flow, a large outflow section has been used (Fukushima et al. [18]). The detailed description of the setup is given in Westerweel et al. [65].

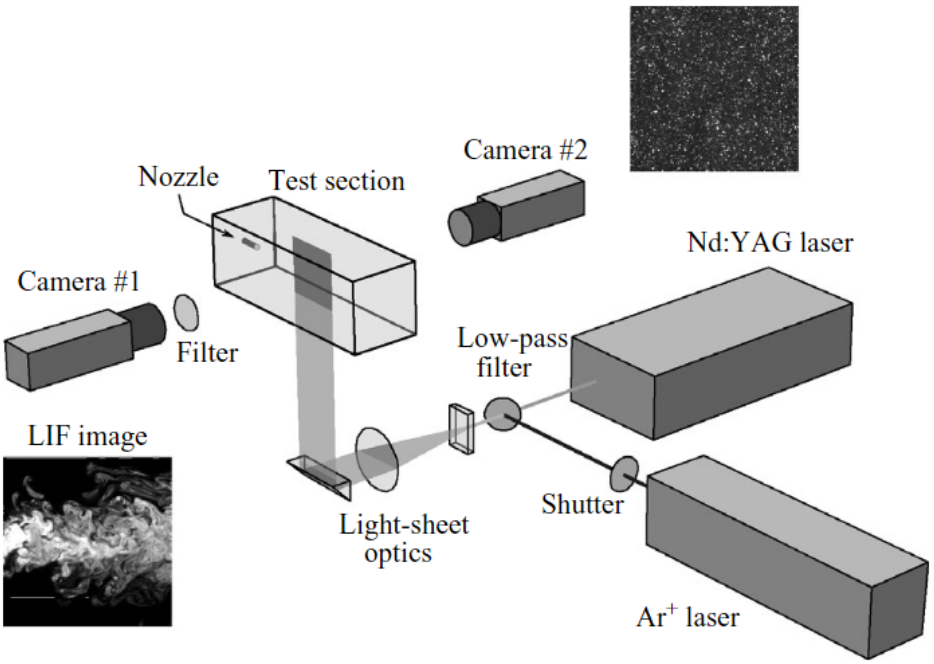

Figure 4.1: Schematic of the optical configuration for the combined PIV/LIF measurement (Fukushima et al. [18], Figure 1).

A twin-cavity frequency-doubled pulsed Nd:YAG laser is used for the PIV measurements. A planar cross-section of the the test Section is illuminated by a 1 mm thick light sheet. The instantaneous concentration field and the velocity field obtained from the laser induced fluorescence (LIF) and the PIV measurements respectively, are shown in Figure 4.2.

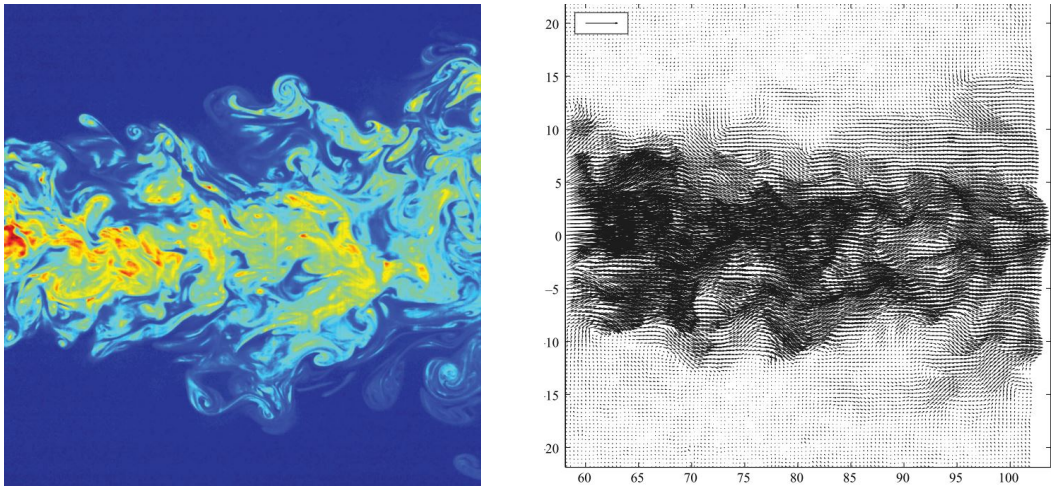

Figure 4.2: Instantaneous concentration field (left) from the LIF measurement and instantaneous velocity field (right) from the PIV measurement (Westerweel et al. [65]).

4.1.2. Results

The PIV frame pairs of the jet flow are interrogated with a two pass interrogation technique with 50% overlap. A 32 X 32 pixel interrogation window is used in the first pass with 16 X 16 pixel spacing. The vectors from the first pass are validated and interpolated onto a grid with a lower window size of 16 x 16 pixels. This procedure is same as the one followed by

Westerweel et al. [65]. The fraction of spurious vectors in the velocity is less than 2%.

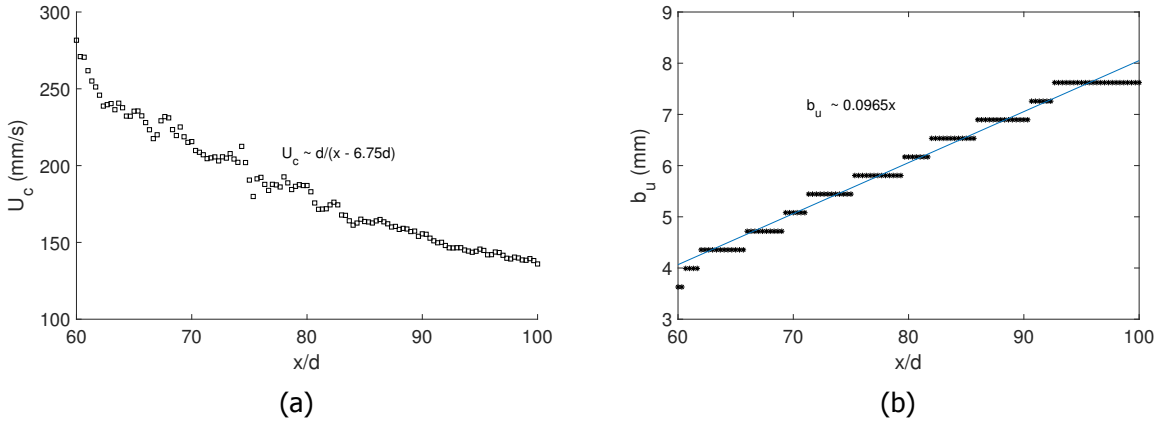

Figure 4.3: (a) The centreline mean velocity (U_c), and (b) the half widths (b_u) for the velocity field as a function of distance from the jet nozzle (x/d).

An example of instantaneous velocity field obtained from the PIV analysis is shown in Figure 4.2. The mean velocity field of the jet flow is estimated from the peaks of the ensemble correlation functions corresponding to each of the interrogation windows. Each frame pair yields (121 x 121) 14641 velocity measurements at a spatial resolution of 0.37 mm. The half width (b_u) of the velocity field, and the centreline mean velocity (U_C) as functions of distance from the nozzle (x), normalized with the jet diameter are plotted in Figure 4.3. The half width of jet is defined as the distance between the jet axis and the point where the velocity is half its centreline value measured perpendicular to the jet axis.

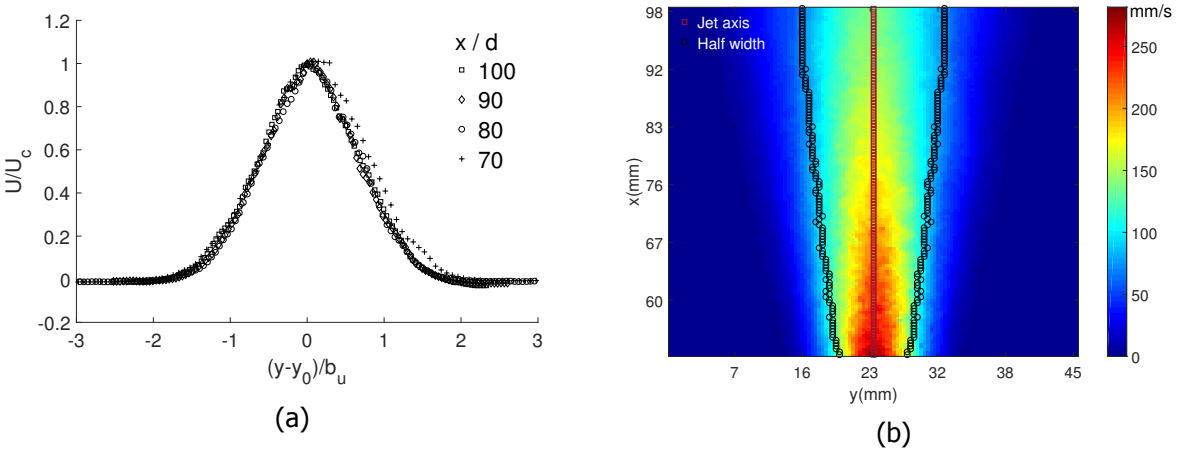

Figure 4.4: Mean axial velocity (U): (a) Normalized profiles at several distances from the nozzle; (b) Contour map with jet axis and the half widths.

The mean axial velocity (U) at different positions from the jet nozzle is plotted in Figure 4.4. The mean axial velocity is normalized with the centreline velocity (U_c). The span-wise coordinates (normal to jet axis) are normalized with the position of jet axis (y_0) and the half width. This produces self-similar profiles [65] of mean velocity at different positions from the nozzle.

The turbulent intensity self-similar profiles and the contour map are shown in Figure 4.5.

The turbulent intensity $((\overline{u'^2})^{1/2})$ (also represented as u_{rms}) is estimated by finding the standard deviation of the axial velocity.

$$u_{rms} = \left(\frac{1}{N-1}\sum_{i=1}^{N}(u_i - U)^2\right)^{1/2}, \tag{4.1}$$

where N is the number of image pairs used (N = 657), and u_i is the instantaneous axial velocity. The turbulent intensity is normalized with the centreline velocity. The self-similarity is consistent (Figure 4.5) for a larger part of axial distances from the jet, with the profile corresponding to x/d = 70 being overestimated possibly due to out-of-plane motion. The turbulent intensity is high near the centre of the jet and falls to zero away from the jet. At the axis, the turbulent intensity is approximately 25% of the centreline velocity.

$$(\overline{u'^2})^{1/2} \approx 0.25U_c. \tag{4.2}$$

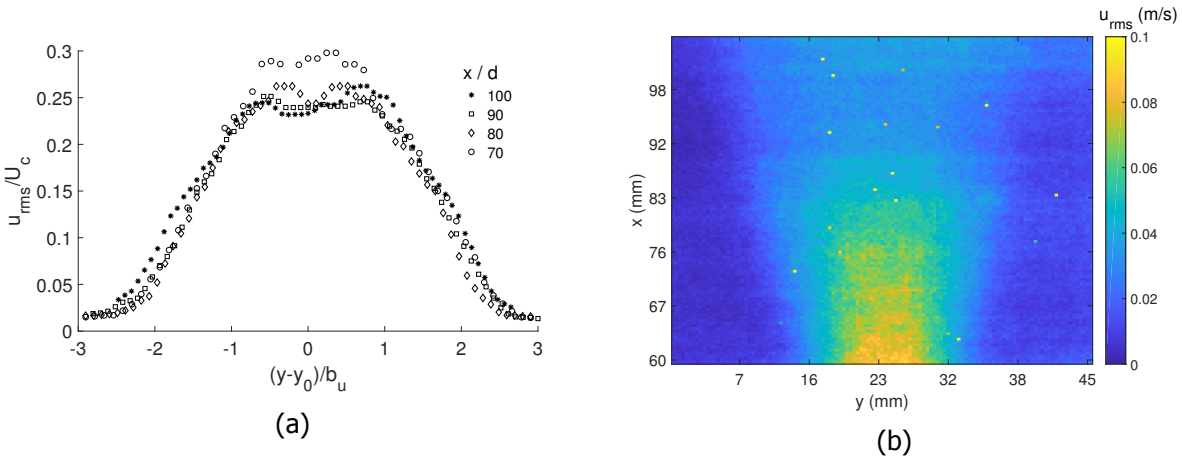

Figure 4.5: Normalized turbulent intensity of the axial velocity fluctuations (u_{rms}): (a) Profiles at several distances from the jet nozzle; (b) Contour map.

The Reynolds stress, $\overline{uv}$ is estimated with the expression given by,

$$\overline{uv} = \frac{1}{N-1}\sum_{i=1}^{N}(u_i - U)(v_i - V), \tag{4.3}$$

where v_i is the instantaneous radial velocity and V is the mean radial velocity. The Reynolds stress is normalized with the centreline velocity (Figure 4.6). Reynolds stress is zero at the centre due to absence of radial fluctuations, and increases to a maximum value around $0.8b_U$. The stresses away from the axis are negligible (zero).

With the relation $\epsilon = 0.015U_c^3/b_u$ (Panchapakesan and Lumley [45]), the dissipation rate is estimated to be 24,414 mm^2/s^3. From this, the *Kolmogorov length scale*, η is estimated to be 0.08 mm with a kinematic viscosity (ν) of 1 mm^2s^{-1}. A more detailed analysis of the jet flow using conventional PIV is given in Westerweel et al. [65].

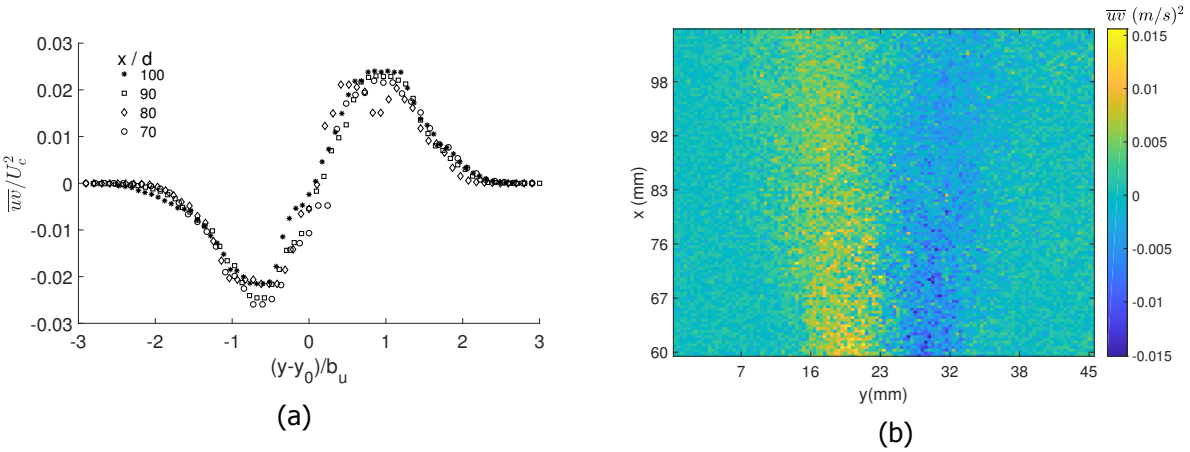

Figure 4.6: Normalized Reynolds stress $\overline{uv}$: (a) Profiles at several distances from the jet nozzle; (b) Contour map.

4.1.3. Turbulent statistics: Ensemble correlation

The PIV image frame pairs are interrogated and the successive correlation matrices corresponding to each image pair are superpositioned. The individual correlation matrices are normalized as explained in Section 3.8. The spatial resolution is same as the previous analysis (0.37 mm), employing the same multi-pass interrogation technique.

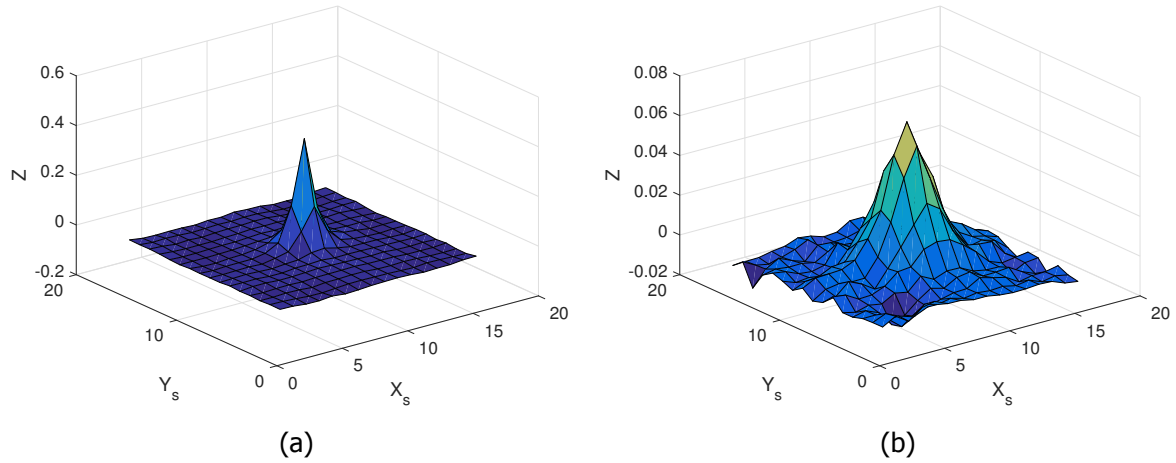

Figure 4.7: Ensemble correlation surface plots: (a) With high SNR, far away from the jet axis; (b) Noisy correlation at the jet axis at x/d = 80.

An example of ensemble correlation with a distinct peak (away from the jet axis) and an ensemble correlation matrix with lot of noise (at the jet axis) are shown in the Figure 4.7. The regions inside the half-width of the jet are dominated by strong gradients and out-of-plane motion producing noisy ensemble correlation. The number of images is not sufficient in these regions to produce an ensemble correlation with a distinct peak. The effect of the noisy ensemble correlation function while fitting a Gaussian function is explained in Section 3.6. A 9 x 9 rectangular filter size is used to filter the correlation.

The turbulent intensity profiles are shown in Figure 4.8. The profiles are smoother than the one obtained using the conventional approach (Figure 4.5). The profiles follow similar trend observed in Figure 4.5. This approach predicts the maxima of the turbulent intensity at

the jet axis. However, the conventional approach predicts a displaced maxima of the turbulent intensity slightly away from the jet axis, converging to 25 % of centreline velocity at the jet axis. This dip is in agreement with the literature [65] [23]. The inability of the ensemble correlation to predict this might be due to the noisy ensemble correlation function at the jet axis.

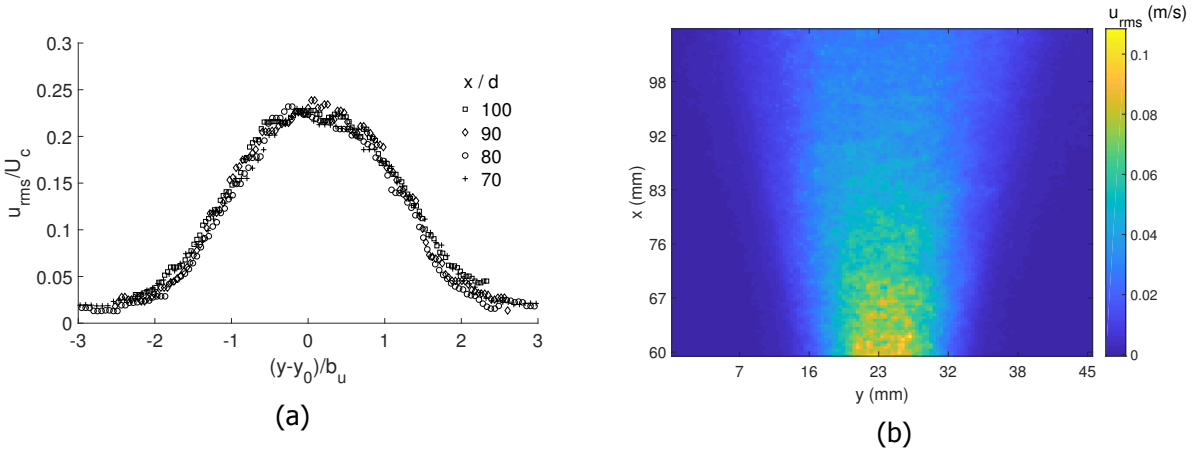

Figure 4.8: Turbulent intensity of the axial velocity fluctuations obtained by fitting a Gaussian profile to the ensemble correlation function: (a) Profiles at several distances from the jet nozzle; (b) Contour map.

The Reynolds stress $\overline{uv}$ profiles are plotted in Figure 4.9. The profiles observed show asymmetry within the half widths of the jet, possibly due to insufficient number of image pairs. With the available number of image pairs, the conventional PIV analysis performs better than the ensemble correlation. However, the results are promising as the estimates for the velocity JPDFs compare well with the literature [65].

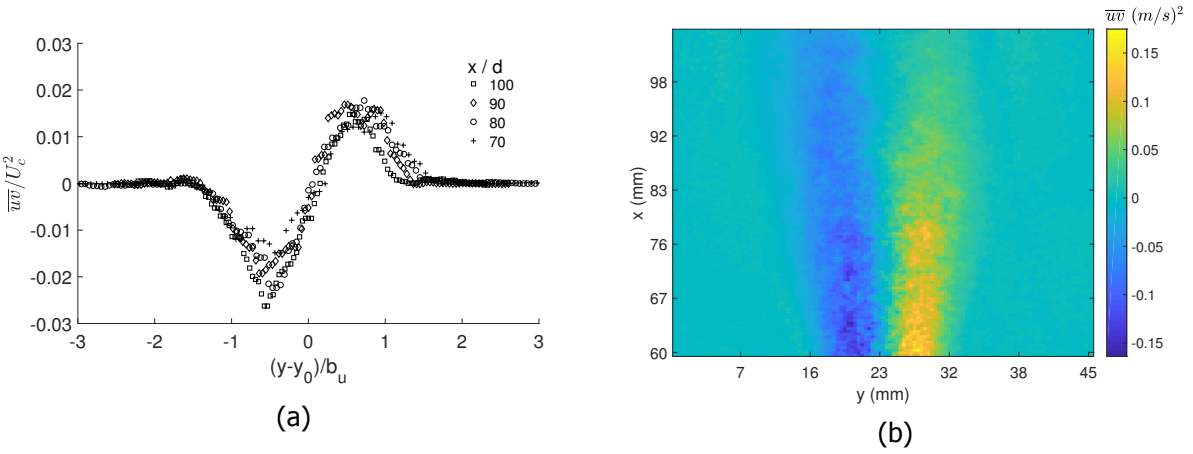

Figure 4.9: Normalized Reynolds stress $\overline{uv}$, obtained by fitting a Gaussian profile to the ensemble correlation function: (a) Profiles at several distances from the jet nozzle; (b) Contour map.

Figure 4.10 depicts the turbulent intensity profiles along with the elliptical shape of ensemble correlation at different positions. Far away from the jet, the shape of the ensemble correlation is symmetric. At the jet axis, the shape is broadened depicting strong velocity gradients. The span-wise fluctuations are negligible at the centre, thus the elliptical shape is aligned with axis. Close to the jet axis, the shape is oriented at an angle due to strong velocity

gradients along y direction.

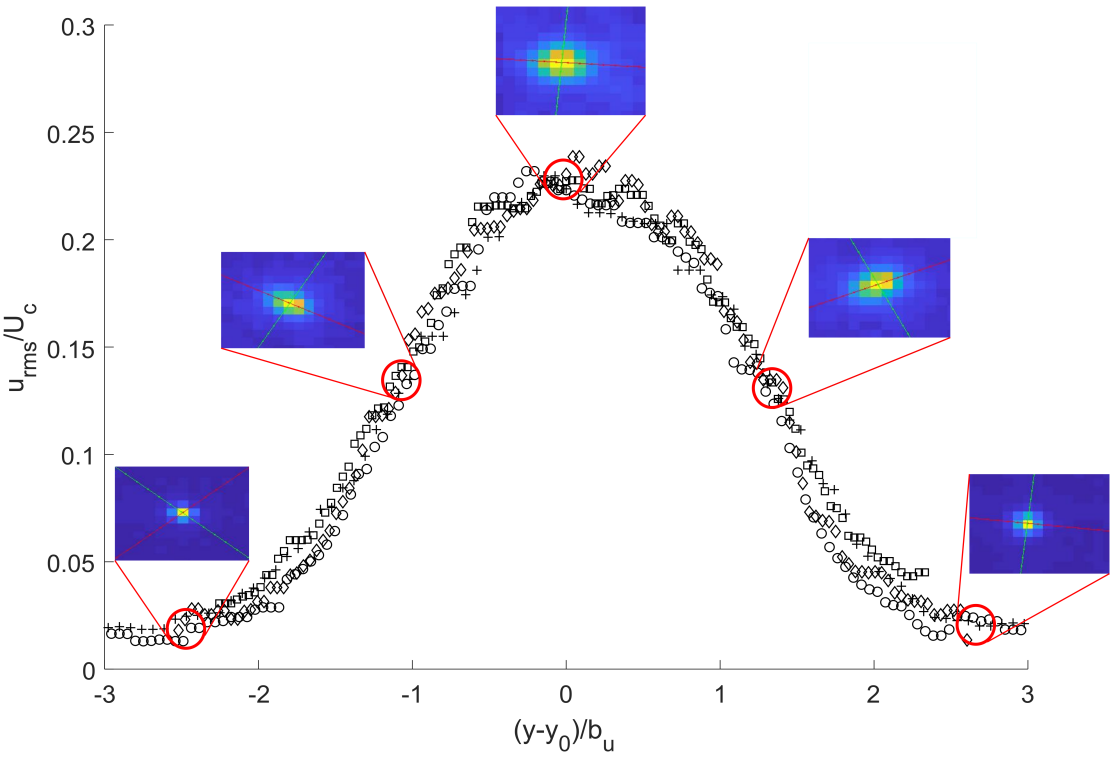

Figure 4.10: Normalized turbulent intensity profiles along with the shapes of the ensemble correlation at different positions. The red line (in the shape of the Gaussian fit) corresponds to axis along the axial direction. The symbols used are given in Figure 4.8.

4.2. Turbulent jet setup: scaled up setup

The results presented in the previous section obtained from the ensemble correlation is noisy near the jet axis. One of the ways to reduce the noise in the ensemble correlation is to increase the number of images (Section 3.6). This motivates to produce ensemble correlation with more image pairs. Thus, a scaled up model of the turbulent jet explained in the previous section is set up. In this experiment, 9000 image pairs are recorded. The experimental setup of the turbulent jet is explained in this section, followed by the results using conventional PIV analysis and the ensemble correlation averaging.

4.2.1. Experimental setup

The turbulent jet is constructed in a 1.96 x 1.96 x 0.6 m^3 tank. The test section is a part of the Row-bot laboratory at the Aero and hydrodynamics laboratory, TU Delft. The test section is primarily used for studying the flow around rowing boat paddles. The working fluid in the jet is water maintained at the room temperature (18^OC). The jet fluid enters the test section through a hollow cylindrical steel section with a constant diameter of 2.7 mm. The flow is allowed to fully develop in the pipe in the laminar regime that is 200 mm long. The jet Reynolds number (*Re*) is maintained at 2000 (jet velocity is 0.75 m/s), in order to ensure the scale similarity with the previous jet measurement. The jet is placed away from the centre of the tank due to installation and maintenance considerations. The immediate wall is 50 cm away from the jet, perpendicular to the jet axis. Furthermore, the distance between the

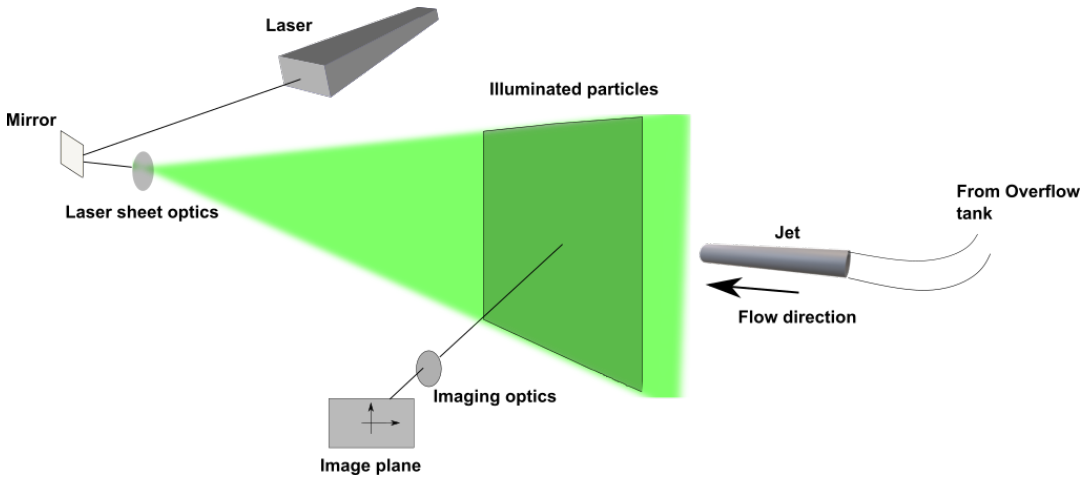

Figure 4.11: Schematic of the PIV configuration for the jet flow experiment.

jet tip and the wall along the flow direction is 110 cm (Figure 4.13). This ensures that the recirculation of flow due to the presence of wall does not affect the flow field in the field of view.

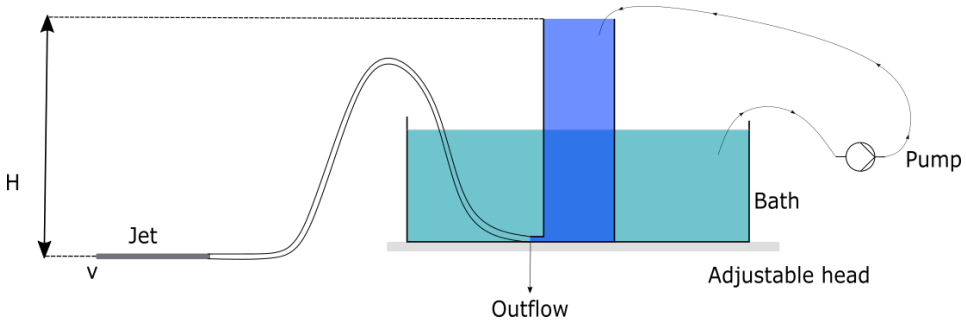

Figure 4.12: Overflow tank used to operate the jet. The head can be adjusted with the help of a vertical rail.

The jet flow is maintained at the constant Reynolds number by using an overflow tank. The construction of the overflow tank is shown in the Figure 4.12. It contains a large bath containing water. Over this bath, a cylinder with an outflow at its bottom is placed. A pump is used to keep the cylinder completely full. This is to keep a constant head in the cylinder to maintain constant flow rate. The bath, as a whole can move up or down by varying the head. The working of the system is based on hydrostatics. A constant head ensures constant outlet velocity from the bottom of the cylinder that follows the relation given by,

$$v = \sqrt{2gH}, \tag{4.4}$$

where 'v' is the outlet velocity and 'H' is the head (Figure 4.12).

The PIV images are recorded by *Imager HS 4M*, a 12 bit digital CMOS camera. The spatial resolution of the camera is 2016 x 2016 pixels (11 μm pixel size), with a maximum framing rate of 1279 fps. The lens fitted with the camera has a focal length of 105 mm. The image magnification is 0.137. The details pertaining to the camera are enlisted in the Table 4.2. The field of view corresponds to 162 x 162 mm^2 area that covers from 40 nozzle diameters to 100 nozzle diameters of the jet in the axial direction. The tank is seeded with hollow spherical glass particles that are 10 μm in size. The particle specification is provided in Table 4.1.

Table 4.2: Camera specifications and details.

Camera	Imager HS 4M
Lens	Nikkon micro Nikkor 105 mm
f#	8
Magnification	0.137
Image resolution (px x px)	2016 x 2016
Field of view (mm^2)	162 x 162

Table 4.1: Particle specifications and properties.

Product	Sphericell 110P8
Composition	Fused Borosilicate glass
Shape	Hollow non-porous microspheres
Density, g/cc	1.10 ± 0.05
Bulk density, g/cc	0.49
Maximum working pressure, psi	10,000
Size distribution (μm)	
10 %	5
50 %	10
90 %	21
97 %	25
Mean size (μm)	9-13

A twin cavity frequency-doubled pulsed Nd:YAG laser is used for illuminating the particles. The laser light illuminates the field of view with a 1 mm thin sheet. Only one pulse is used for the experiment hence, effectively operating as a single pulsed laser system. A synchronizer is used to synchronize the camera frame rate and the laser light pulse rate. Thus, the time delay is controlled by the frame rate set by the synchronizer. The frame rate is selected such that the displacement of particles is around 7-9 pixels. The frame rate is set to 630 Hz thus, the time delay between the consecutive exposures is 1.6 ms. The laser emits light at a frequency of 532 nm (viz. green). The laser light sheet is aligned with the jet axis. Figure 4.13 depicts the experimental setup.

The image particle size is calculated by considering the effect of diffraction. The diffraction limited spot, given by Equation (3.5) is estimated to be 11.81 μm. The particle image diameter, given by Equation (3.4) is estimated to be 11.89 μm. The seeding concentration is approximately 2 particles/mm^3, injected such that there are 10-12 particles on an average in a 32 X 32 pixel interrogation windows. The particle response time (τ_p) is 5.55 μs, which is negligible compared to the time delay (1.6 ms).

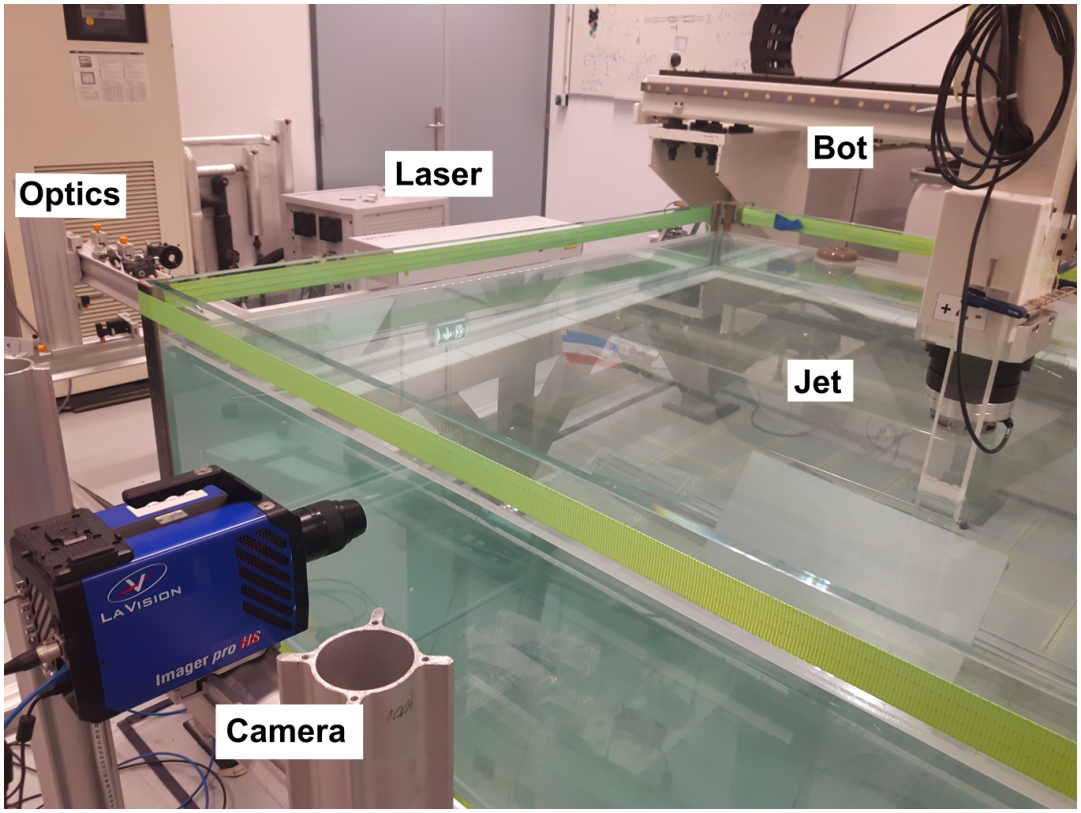

(a) The PIV components used for the turbulent jet experiment.

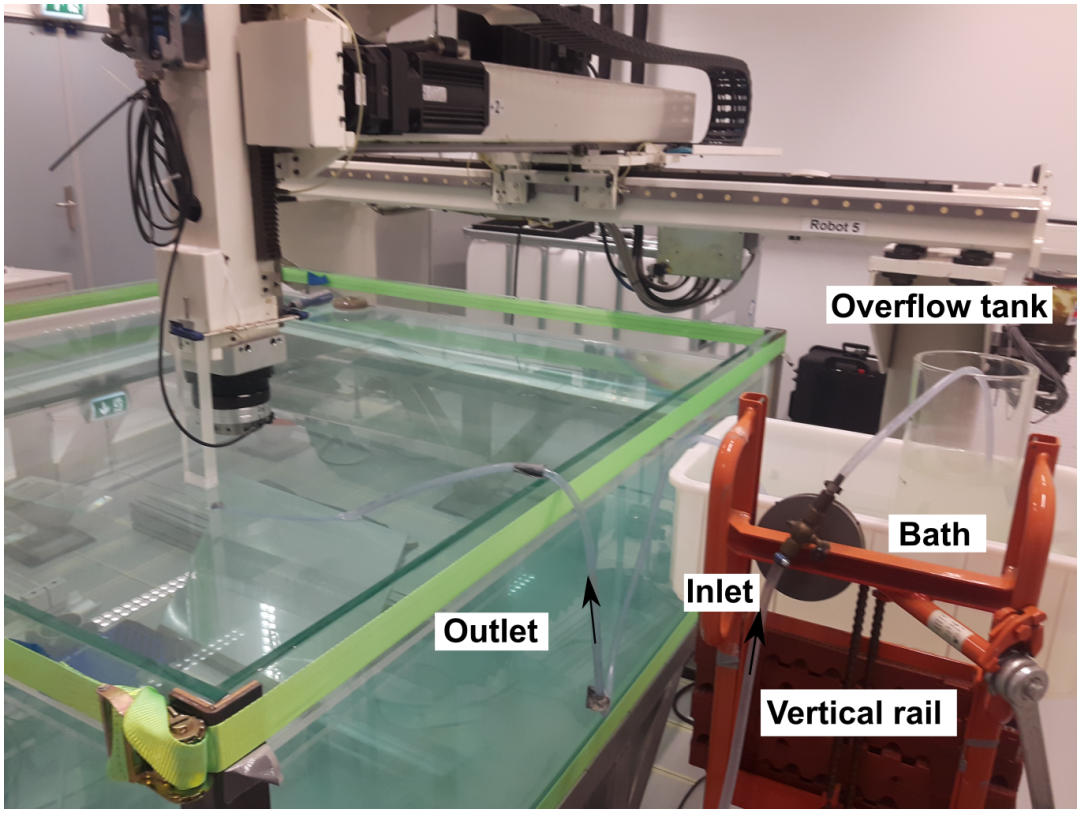

(b) The overflow tank system used to maintain the flow at a constant Reynolds number of 2000.

Figure 4.13: Experimental setup to study the turbulent jet flow.

4.2.2. Results and observations

The jet velocity measured at the outlet of the jet is 2.7 m/s. The field of view covers from 45 to 100 nozzle diameters away from the jet nozzle. In total, 9000 PIV images are captured in single pulsed mode. The interrogation of successive images results in improper cross-correlation, producing minimum correlation at zero displacement (Figure 4.14). This is an artifact of the camera, whereby an instance of the first exposure is present in the second exposure. Thus, the interrogation of the immediate exposures are skipped, and the odd images are interrogated. This doubles the time delay to 3.2 ms as well as particle displacements up to 15-18 pixels. The issue with the improper spatial correlation is explained in Appendix A.

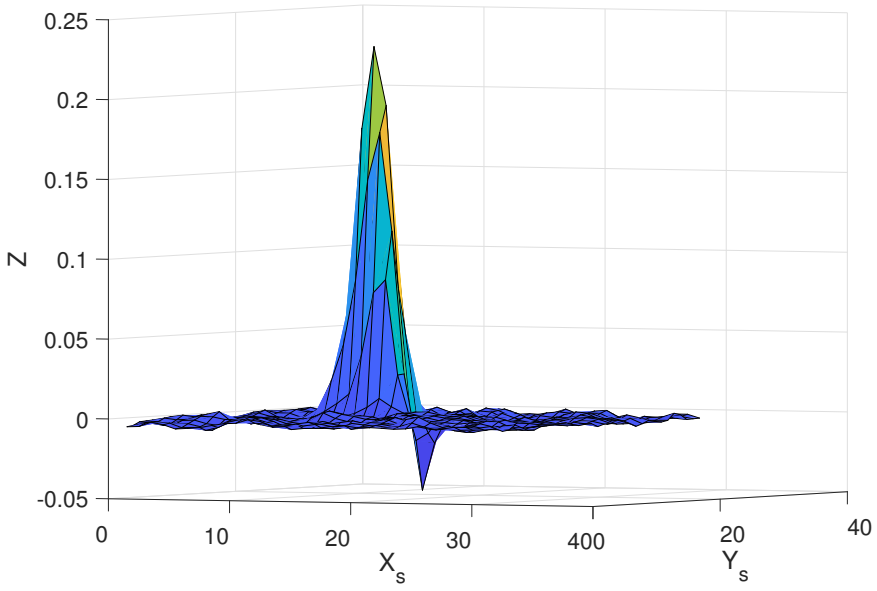

Figure 4.14: The interrogation of successive images produces minimum correlation at zero displacement (corresponds to the centre of the matrix). This affects the shape of the correlation and cannot be used for estimating the velocity JPDFs from its shape.

The odd image frames are interrogated using a two pass interrogation technique with 32 x 32 pixel window with 50 % overlap. The fraction of spurious vectors is less than 3%. Each image pair produces 15625 velocity vectors (125 x 125) at a spatial resolution of 1.28 mm. A median test in 3 x 3 vicinity of an interrogation window is applied for outlier detection in the velocity measurements. The fraction of spurious vectors is less than 4%. An example of the instantaneous PIV image pair is given in the Figure 4.15. The corresponding instantaneous and mean velocity fields are given in Figure 4.16.

(a) Exposure 1 (b) Exposure 3

Figure 4.15: The raw PIV odd images used for PIV interrogation. The inverted gray scale colour pattern varies from 0-600 counts. The jet flows from right to left.

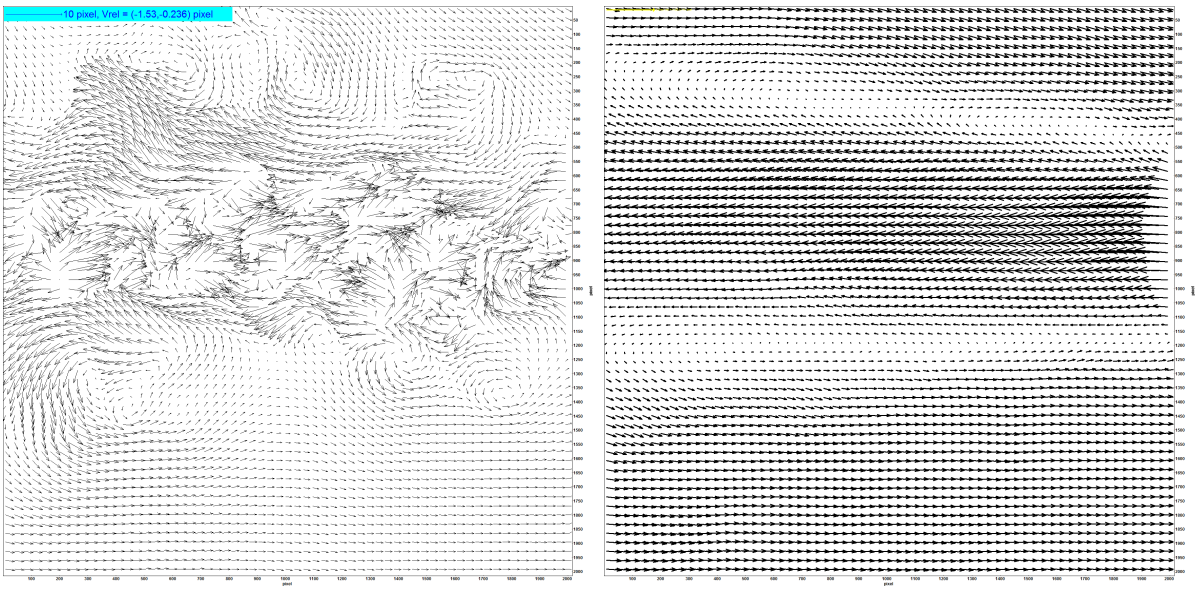

(a) (b)

Figure 4.16: (a) Instantaneous velocity field and (b) mean velocity field obtained from the PIV measurement. The jet flows from right to left. The mean velocity depicted is obtained by averaging the instantaneous vectors.

The axis of jet is misaligned with the camera field of view in the image plane. The angle between the horizontal axis of the field of view and the jet axis is 3.66^0 (Figure 4.17). In order to account for this misalignment and to produce self-similar profiles of the turbulent jet, the coordinate system is rotated by 3.66^0 such that the $x^{'}$ axis of the rotated coordinate system is aligned with the jet axis, as shown in Figure 4.17. The self-similar results discussed further are obtained using this new coordinate system $(x^{'}, y^{'})$. The contour maps are plotted in the original coordinate system (X,Y) for simplicity.

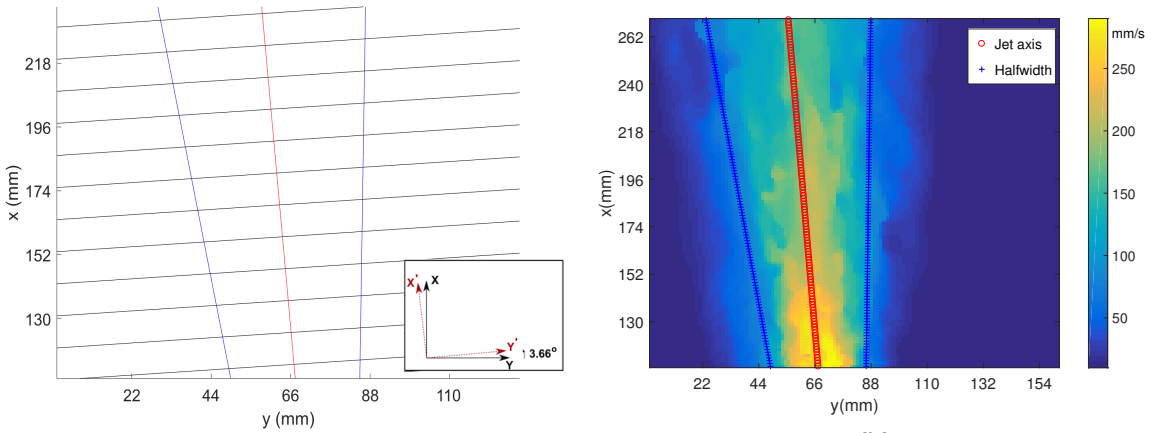

Figure 4.17: The jet axis and the corresponding jet half-widths is misalignment with the axis of the camera: (a) Coordinate transformed from X-Y system to $X'Y'$ system; (b) Axial velocity contour map with jet axis and half widths in X-Y axis.

The mean velocity of the flow field is obtained from the peaks of the ensemble correlation of instantaneous correlations of 9000 image pairs. The centreline mean velocity (U_c) and the jet half width (b_u) are plotted in the Figure 4.18. The half width is linear with the axial distance from the nozzle, with a slope of 0.9008. The centreline mean velocity (U_c) follows a displaced inverse scaling with the axial distance from the jet nozzle given by,

$$U \sim \frac{d}{x - 5.5d}. \tag{4.5}$$

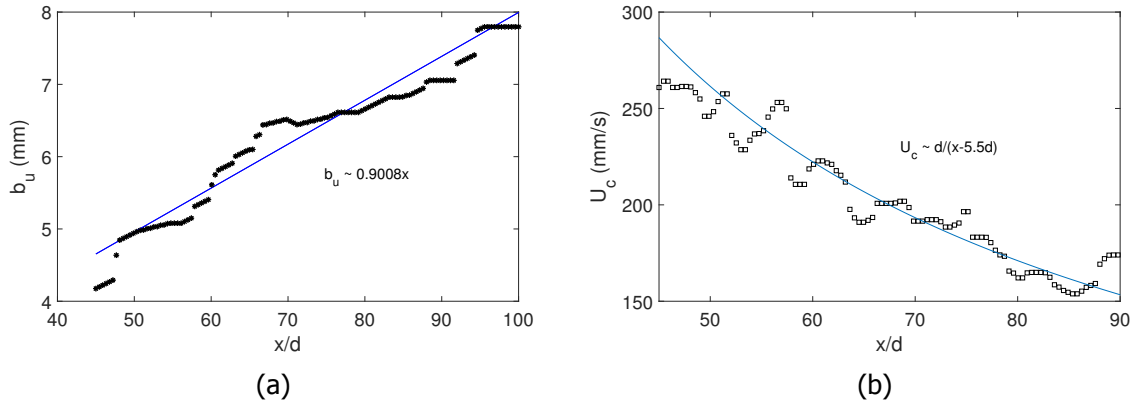

Figure 4.18: (a) The half-width (b_u) of the jet, and (b) the centreline velocity (U_c) as functions of the distance from the nozzle obtained using ensemble correlation.

The mean velocity in a conventional PIV analysis is obtained by averaging the instantaneous vectors. The mean axial velocities obtained from the ensemble correlation and from the conventional analysis are plotted at several distances from the jet nozzle (Figure 4.22). The vector averaging produces a smooth profile with some deviation from the self-similar profiles. This might be due to the finite differences in the rotated coordinate system. The mean axial velocity obtained from the ensemble correlation shows local deviations from the self-similar profiles. The local deviations can also be visualized from the velocity contour plots (Figure 4.22b). The ensemble correlation is very broad in these regions which

causes bias in determining the maximum value in the ensemble correlation. The regions corresponding to these local deviations also have biased correlation shapes as shown in Figure 4.20. The biased correlation might be due to issues with CMOS camera used. In addition to this, asymmetry with respect to the jet axis is observed in the profiles. This is something expected because of different boundary conditions in either sides of the jet axis. The top of the jet has a free shear boundary condition and the bottom of the jet has no slip and no penetration boundary condition. The velocity vectors until 60 nozzle diameters away from the jet are dominated by out-of-plane motion producing large number of spurious vectors. This produces wrong estimates for the velocity. An effect of this is shown in the Figure 4.21, where the centreline velocities (obtained by vector averaging) until 65 nozzle diameters, are predicted incorrectly. This is however not observed with ensemble correlation (Figure 4.18b) as the correlation peaks are added which effectively removes the random peaks in the correlation corresponding to one image pair.

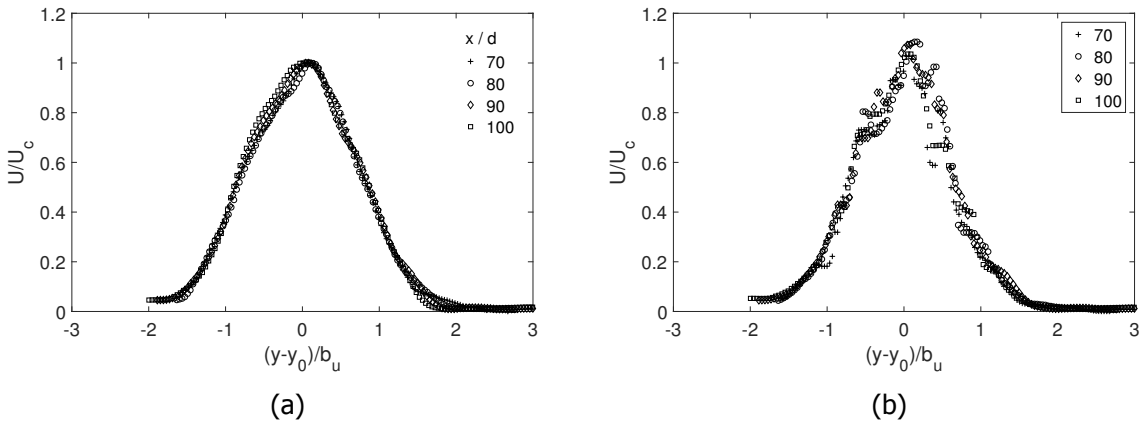

Figure 4.19: The mean axial velocity at several distances from the jet nozzle: (a) From vector averaging; (b) From ensemble correlation.

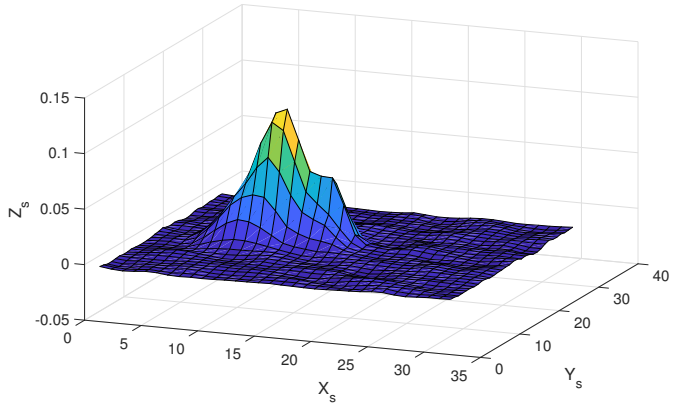

Figure 4.20: The biased correlation observed within the halfwidth of the jet. 6000 image pairs are used to produce the ensemble correlation at x/d = 60.

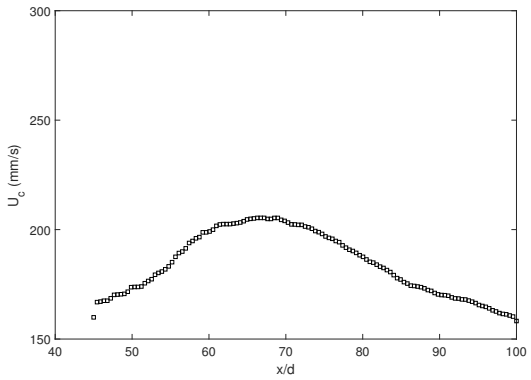

Figure 4.21: The centreline velocity (U_c) as a function of the distance from the nozzle obtained using vector averaging. The out-of-plane motion is dominant in the regions corresponding to 45-65 nozzle diameters at the jet axis.

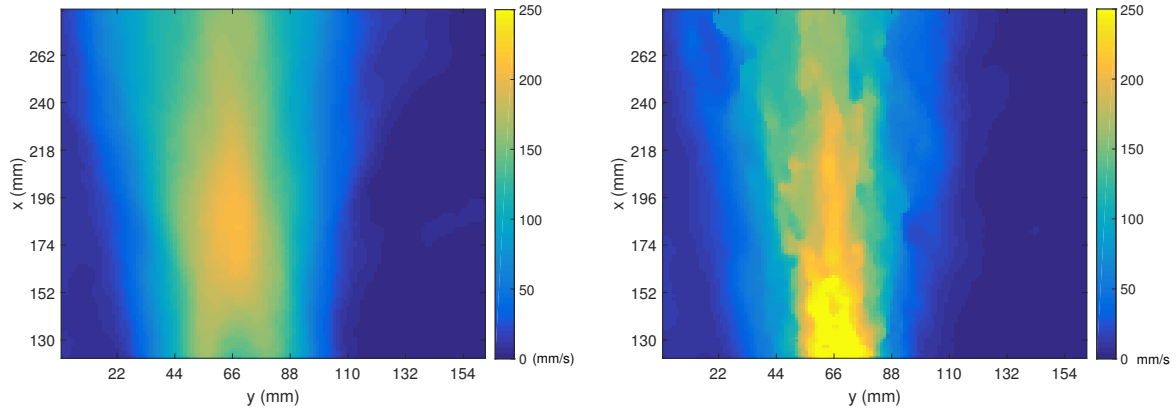

Figure 4.22: The mean axial velocity contour plots: (a) From vector averaging, produces smooth contour. The velocity vectors are under-predicted at 45-65 nozzle diameters; (b) From ensemble correlation. The contour map shows the local deviations which is due to the biased ensemble correlation.

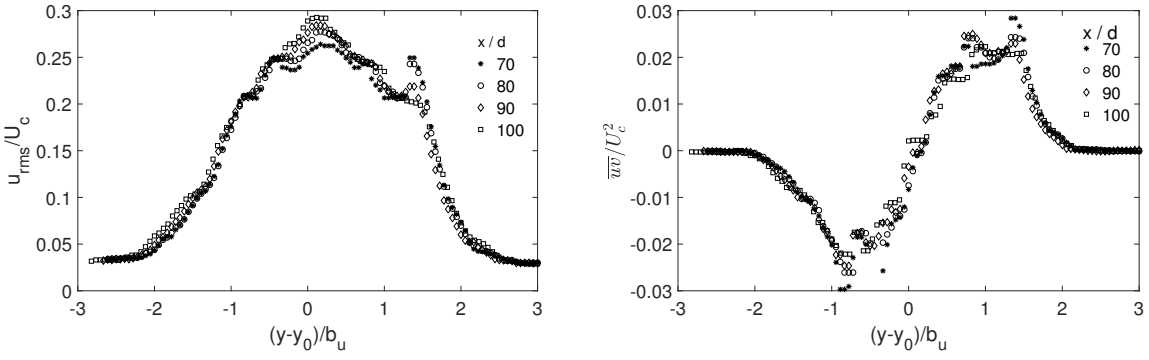

Figure 4.23: The turbulent stresses obtained from the velocity vectors following the conventional analysis.

The turbulent intensity and the Reynolds shear stress are obtained using Equation (4.1) and Equation (4.3). Figure 4.23 shows the profiles. The stresses are affected strongly by incorrect estimates for mean velocity until 60 nozzle diameters. The Reynolds shear profiles within the half widths of jet deviate from self-similar profiles. Turbulent intensity profiles estimated are not well resolved within the half widths of the jet, compared to the profile obtained in the previous experiment (Figure 4.5).

Turbulent statistics: Ensemble correlation

As mentioned before, 9000 image pairs are superpositioned to produce the ensemble correlation. A typical ensemble correlation obtained is depicted in the Figure 4.24. The ensemble correlation is broadened due to velocity gradients. The noise away from peak is very low. In the previous chapter, the variation of SNR with the number of image pairs was shown in Figure 3.13.

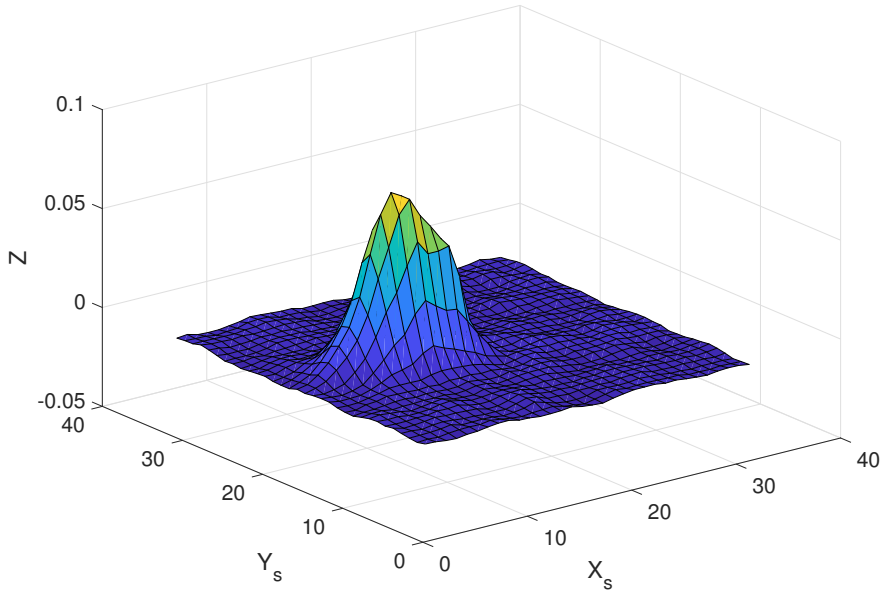

Figure 4.24: An example of ensemble correlation using 9000 image pairs at x/d = 80 near the jet axis.

In order to retrieve the velocity JPDFs, Gaussian profiles are fitted with a 4 x 4 rectangular filter. The turbulent intensity and Reynolds stress profiles are obtained for the ensemble correlations using different ensemble size. In order to determine the quality of the retrieved data, different number of images are used to produce the ensemble correlation. The variation of the stresses retrieved using different number of images to produce ensemble correlation, are shown in Figure 4.25. The stresses obtained are randomly distributed for an ensemble size of 500. As the number of image pairs increases, the profiles eventually shape into the profile estimated using 6000 image pairs. The stresses estimated using 6000 image pairs are represented by the red line in Figure 4.25.

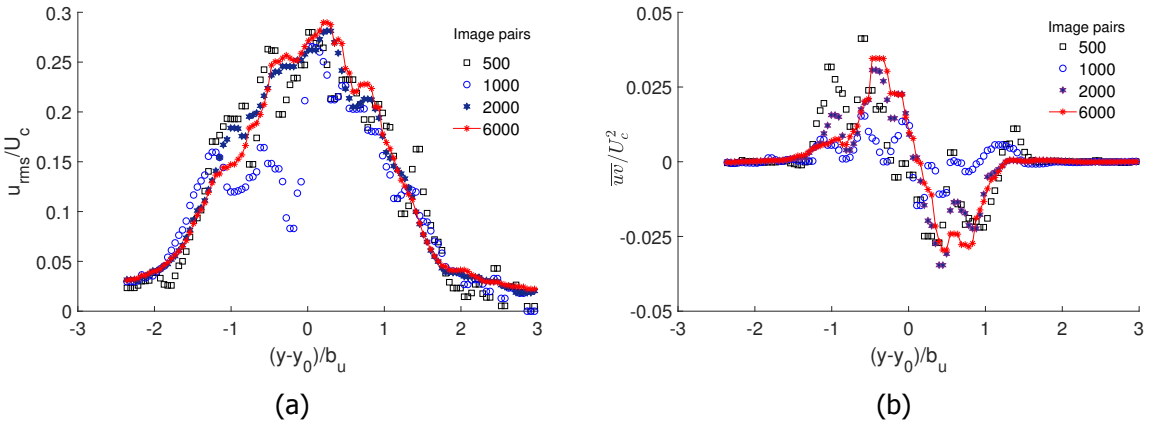

Figure 4.25: Variation of the (a) turbulent intensity and the (b) Reynolds stress with the number of images used to obtain the ensemble correlation at 80 nozzle diameters from the jet nozzle.

The turbulent intensity profiles obtained using 9000 image pairs at several distances from the jet nozzle is plotted in Figure 4.26. The profile follows similar trends to that obtained using the conventional PIV and also with results obtained by Westerweel et al. [65]. The profiles appear smooth, and at the centre, the turbulent intensity is slightly lower as observed in Figure 4.5 from experiments from Westerweel et al. [65]. The asymmetry observed might be due to combined effect of the different boundary conditions and the rotation of coordinate system.

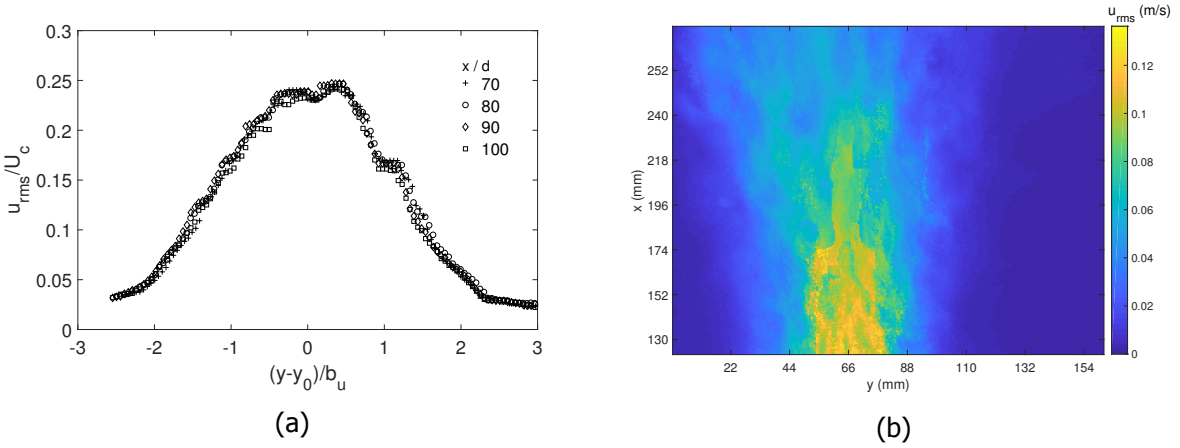

Figure 4.26: Normalized turbulent intensity profiles obtained from the ensemble correlation: (a) Profiles at several distances from the nozzle; (b) Contour map

The Reynolds stress profiles obtained (Figure 4.27) is very smooth compared with the conventional PIV analysis (Figure 4.23). The profiles appear to be self-similar for larger part of distances from the jet nozzle. The profiles agrees with the results from Westerweel et al. [65]. The dissipation rate is estimated to be 12367 mm^2/s^3. The value of η is estimated to be 0.09 mm. The linear dimension of the interrogation window is 2.57 mm. The resolution achieved is lower than that achieved in experiments by Westerweel et al. [65].

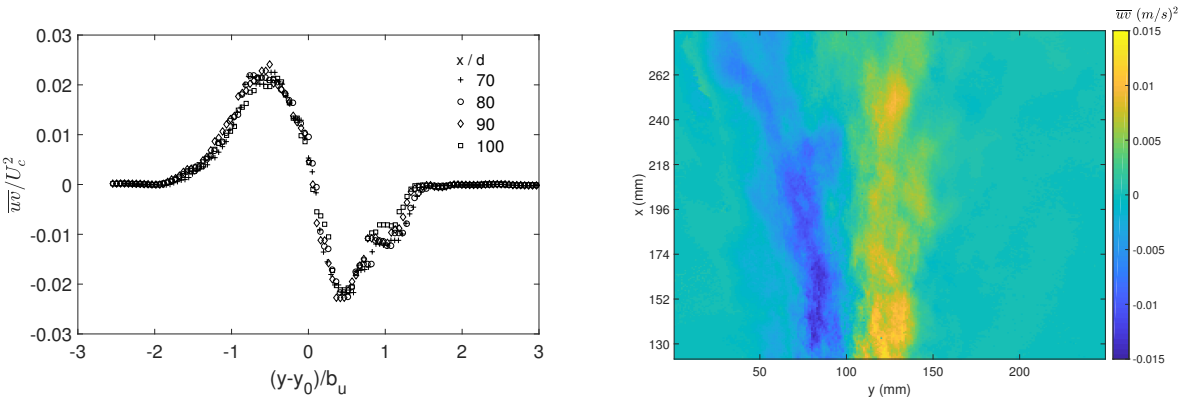

(a) (b)

Figure 4.27: Reynolds stress $\overline{uv}$, obtained by fitting a Gaussian profile to the ensemble correlation function: (a) Profiles at several distances from the jet nozzle; (b) Contour map.

4.3. Inferences

The jet images from Westerweel et al. [65] are used to produce the ensemble correlation. The image pairs are not enough to produce a distinct peak. Especially, the shape of the ensemble correlation is affected by the noise around the broadened displacement peak near the jet axis. A scaled up jet experiment is performed to record more images, and to use them to produce the ensemble correlation. The ensemble correlation produced within 65 nozzle diameters away from the jet is affected strongly by out-of-plane motion resulting in a distorted ensemble correlation. Beyond 70 nozzle diameters away from the jet, ensemble correlation predicts biased mean velocity. This bias in velocity is caused by broadening of the peak, which allows the peak value to spread over immediate pixels near the actual peak (Westerweel [64]). This causes sudden local deviations in the mean velocity within the halfwidth of the jet. This might be due to using larger interrogation windows. This might also be an artifact of the CMOS camera.

The turbulent intensity and the Reynolds shear stress are retrieved from the shape of the ensemble correlation. The estimated stresses show high accuracy display self-similar profiles. The retrieved stresses, naturally show dependency on the number of image pairs used to produce the ensemble correlation. The resolution of the experiment is not as high as experiments by Westerweel et al. [65]. However, the information on the velocity JPDFs are successfully retrieved from the shape of the ensemble correlation. The interrogation windows are intentionally kept large (32 x 32 pixels) to detect the shape of the ensemble correlation. The results obtained showcases the potential of the approach to successfully predict the turbulent stresses, even in regions with strong velocity gradients.

5

Turbulent flow in a pipe: experiment

In the Alpha Loop facility at Deltares, it is possible to study flow at high Reynolds numbers in a long pipe. The flow is studied using two-dimensional planar PIV. The method proposed in Chapter 3 is applied to study the flow. The potential for achieving higher resolution can be realized from the results discussed in Chapter 4. This approach is implemented to resolve the near wall region at high Reynolds numbers. In this chapter, the experimental setup and the corresponding results are discussed. Firstly, the anatomy of the experimental setup is explained in detail in Section 5.1. This is followed by a brief description of methods employed to minimize the reflections observed in the PIV images in Section 5.2. Finally, the results from the experiments are provided and compared with the literature in Section 5.3.

5.1. Experimental setup

5.1.1. Description of Alpha Loop facility

Alpha Loop is a multiphase flow facility at Deltares, Delft. The facility is used to investigate the flow in a wide range of academic and industrial multiphase research disciplines. The facility can be used to study single phase (water), two phase (water and air), and three phase (water, air and sediment) flow systems. The facility consists of a 320 m long pipe with an internal diameter of 206.5 mm (PN16 DN200). The facility, initially operated as a open loop system is modified to a closed loop system in order to perform high Reynolds number flow experiments. The closed loop ensures constant and homogeneous seeding density, and fully developed flow condition as flow is recirculated in pump continuously. The long pipe consists of multiple short sections (6.125 m long) bolted together. The flow is driven by either or both of the two available centrifugal pumps in the *pumping island* (Figure 5.1). The pumps can be connected in parallel or series depending on the requirement. The flow speed is controlled by the rotational frequency of the pump motor, which is varied with the help of a manual keyboard. The pump frequency can be varied from 0-50 Hz. The facility is equipped with a flow meter that measures the volumetric flow rate averaged over 3 seconds. The valves are also used occasionally to regulate the flow.

Figure 5.1: *Pump island*, Alpha Loop: the pipe section with the driving pumps. The pumps can be operated in series or parallel depending on the requirement. Only one of the pumps (rightmost in the figure) was used for the current study.

Figure 5.2: The pipe section with the surge vessel. (a) Flow direction upstream to the measurement cabin; (b) Flow direction downstream of the measurement cabin.

The total volume of the pipe is 10.7 m^3 approximately. A surge vessel is connected to the pipe just downstream of the *pump island* (Figure 5.2). It ensures the safety of the pipe against pressure fluctuations.

5.1.2. PIV setup

The pipe is equipped with an optically transparent pipe section, 300 mm long (axially) and 206 mm in diameter. This transparent section is made of PMMA (acrylic, Poly(methyl methacrylate)) glass, also called as Plexiglas. This section is positioned approximately 530 pipe diameters downstream of the *pump island*. The transparent section is surrounded by a metal casing with glass windows (optically transparent, Figure 5.3). This section is designed to withstand a maximum pressure of 3 $bar(g)$. However, the pressure is maintained below 1 $bar(g)$ throughout the measurement to ensure safe operation.

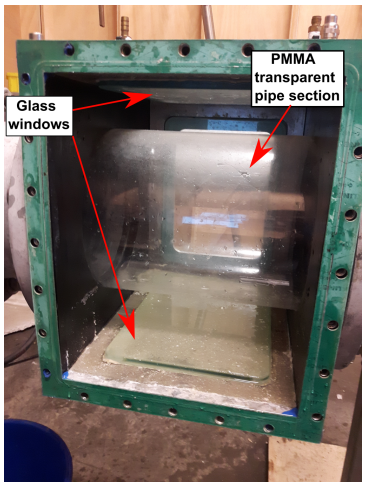

Figure 5.3: Photograph of outer box with glass windows and the acrylic pipe section taken while cleaning the section prior to the PIV experiment.

The water is seeded with 10 μm hollow spherical glass particles. The properties of the particles are given in Table 4.1. A planar cross-section of the optically transparent section is illuminated with a laser light sheet. A twin-cavity frequency-doubled pulsed Nd:YAG laser is employed for this purpose. The laser emits light at a frequency of 532 nm (viz. green). The laser light sheet is aligned with the centre of the pipe using an optical system (Figure 5.5). The optical system consists of two mirrors with a cylindrical lens between them, followed by a spherical lens with a focal length of 1 m. The distance between the cylindrical lens and the mirror is kept short such that the laser width just before the field of view is longer than the width of the glass window. The laser light from the cavity, circular with a diameter of 9 mm is focused such that the thickness of the light sheet is approximately 0.8 mm (estimated assuming Gaussian light path [5]) at the measurement domain.

Table 5.1: Camera specification and details.

Camera	Sensicam qe
Lens	Nikkon micro Nikkor 50 mm
f#	4
Magnification	0.035
Image distance (mm)	0.49
Image resolution (pixels)	1376 x 1040
Field of view (mm^2)	190 x 250
Pixel size (μm)	6.45

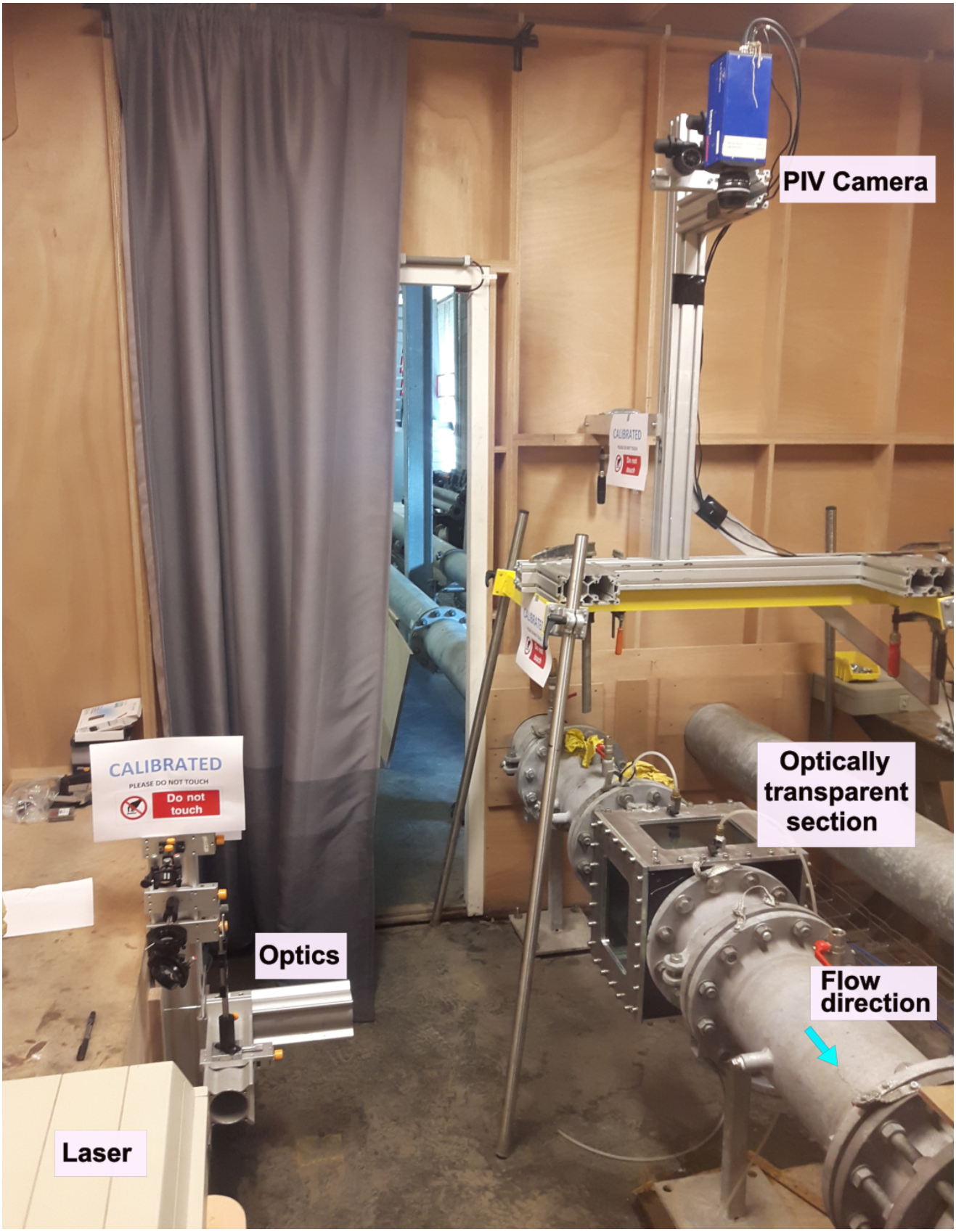

Figure 5.4: Setup of the PIV system used to measure the flow in the Alpha Loop pipe section.

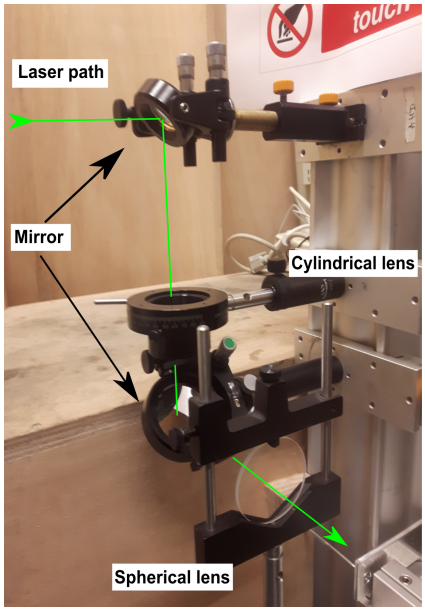

Figure 5.5: Optics employed to create a laser light sheet with 0.8 mm thickness.

The PIV images are recorded by *FlowMaster Imager Intense sensicam qe*, a 12 bit digital CCD camera. The camera is positioned such that the optical axis is perpendicular to the laser sheet plane. The camera has a spatial resolution of 1380 x 1048 $pixels$ and a framing rate of 10 Hz. The camera is fitted with a lens with 50 mm focal length (Nikon Micro Nikkor). The image magnification is 0.035, and the field of view corresponds to a 190 x 250 mm^2 area that captures the transparent glass window completely. The camera and the field of view are misaligned (in the image plane) with an angle of 0.14^0 between the pipe axis and the camera. This misalignment translates to 3 pixels difference from one end to other (1376 $pixels$) in the image plane. The camera is operated in dual frame mode such that the laser exposures are recorded in separate frames. The camera and the laser are synchronized using Davis commercial software, version 7.2. The time delay between the laser pulses is varied (using Davis) depending on the velocity of the flow such that the one-quarter rule [5] for in-plane displacement of the particles is satisfied. This is also verified (and adjusted accordingly) by performing a test PIV interrogation (in Davis) and ensuring that the spurious vectors are less than 3%. For the test PIV interrogation, a single pass 32 x 32 pixels interrogation window is used. In total, 20,000 images are recorded for each of the Reynolds number at an acquisition rate of 5 Hz. However, the intensity of the exposures varied throughout the measurement period (explained later). To reduce the mean intensity fluctuations of the laser light in a measurement series, the recordings are taken as four sets of 5000 images each.

5.1.3. Seeding

The closed-loop pipe flow is seeded with 10 μm Sphericell spherical glass particles (Table 4.1). The seeding is injected through a valve at the top portion of the pipe. The seeding injection setup is shown in Figure 5.6. The particles are mixed with water filled in a cylindrical vessel. The solution with the particles is transferred to the pipe using a small pump. To maintain 8-10 particles in 32 x 32 pixel interrogation window on an average, 0.03 g of particles are added. The PIV images are monitored while injecting particles in order to ensure that the flow does not get over-seeded. The surge vessel helps in preventing the pipe getting over pressurized while injecting the seeding. Also, the absolute pressure is maintained high to keep the flow clean of air bubbles. The properties of the seeding particles are tabulated in Table 4.1. The

particle image diameter, dominated by diffraction-limited diameter (5.37 μm) is estimated to be 5.38 μm.

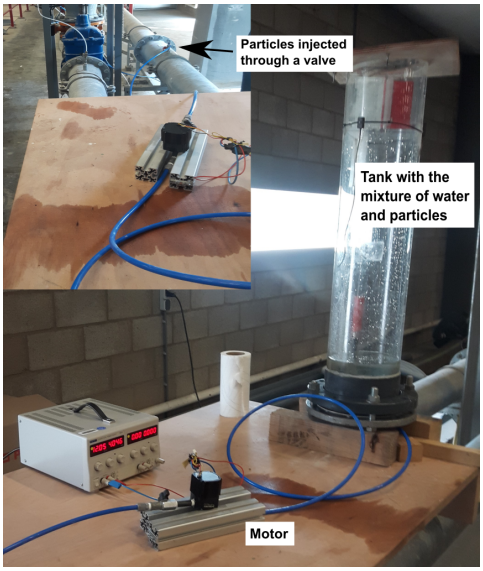

Figure 5.6: Setup of the particle injection system.

Figure 5.7: Setup during calibration of the camera.

5.1.4. Calibration

The camera is calibrated such that the field of view is in focus and aligned. This is carried out by inserting a calibration plate. The calibration plate (or target) contains symbols (pluses in the current case) that can be recognized by the camera and the processing software (Figure 5.8). The pluses are separated by 15 mm (centre to centre) and the end to end length of each plus is 10 mm. The calibration plate is fabricated such that it does not have contact with the acrylic pipe. The calibration target is attached to a holder that can be bolted with the pipe.

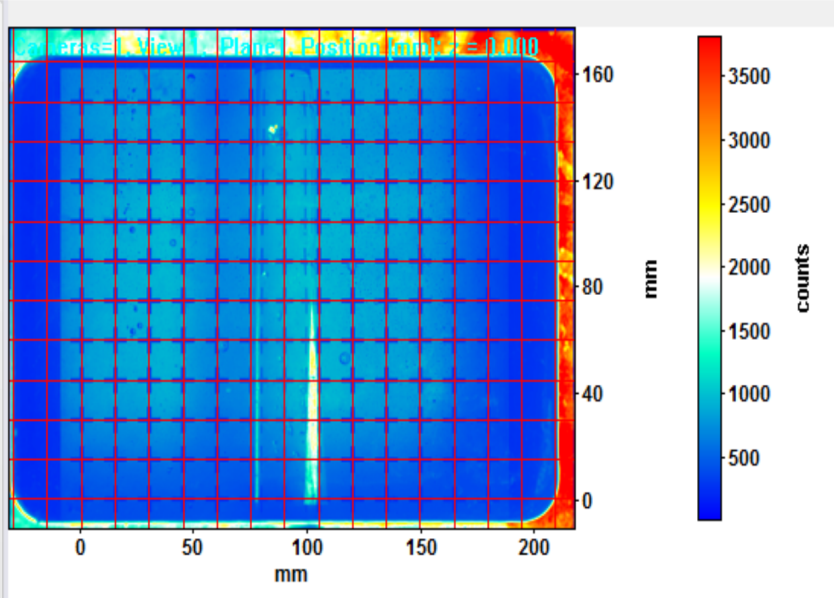

Figure 5.8: The image of the field of view with the calibration target. Note the air bubble at the top of the pipe section. The RMS of error in the calibration is 0.2784 $pixels$.

The pipe is closed from one end while calibration. This allowed many bubbles to settle in the pipe as well as in the sections between the acrylic pipe and the glass windows. The camera is calibrated with an air bubble at the top of the pipe. A third order polynomial is fit to calibrate the images (Soloff et al. [55]). The root-mean-square (RMS) of the fit is estimated to be 0.2784 $pixels$. The calibration is performed using Davis commercial software.

5.2. Study on optical disturbances in the PIV images of the pipe

PIV is an optical technique, wherein the camera images the particles illuminated by the laser light sheet. This requires an optically transparent section such that the light sheet illuminates the measurement domain and the field of view is optically accessible from the reference of the camera. In the Alpha loop facility, the optically transparent glass windows and acrylic pipe are exposed to the laser light and the PIV images are affected by optical disturbances due to reflection, glare and refraction. Figure 5.14 shows the time averaged image (of 4800 images) of an Alpha Loop PIV measurement. The bright lines near the centre of the pipe and other non uniform exposures (near wall) are caused by the optical disturbances from the glass windows and the PMMA section. In order to study the near wall turbulence, these optical disturbances have to be reduced. Thus, a scale similar model to the optical section in the Alpha Loop facility is constructed. The details on the experimental setup is given in Appendix D.

Figure 5.9: The optically transparent sections setup to mirror the Plexiglas pipe and glass box in Alpha Loop facility.

Table 5.2 shows the optical properties of the relevant materials for doing the PIV experiment. Plexiglas material and glass have similar optical properties. In the mock up setup, a vertically oriented acrylic tube is placed inside an acrylic box to mirror the acrylic pipe inside a box with glass windows in Alpha Loop facility (Figure 5.9). The outer box is also made of Plexiglas as its properties are similar to that of glass.

Table 5.2: Optical properties of acrylic glass (PMMA) and glass [6].

Properties	**PMMA glass (Plexiglas)**	**Glass**
Refractive index (at $23^{O}C$)	1.49	1.51
Reflectance at zero incidence	0.039	0.042
Transmitivity (visible light)	0.92	0.91
Critical angle	42.2^{O}	41.1^{O}

The reflections observed in the images recorded are shown in Figure 5.10a. The front wall reflections represent the reflections from the face of the Plexiglas pipe facing the camera. The back wall reflections represent the reflection from the face opposite to the camera. There are four bright lines in the region corresponding to the measurement domain. In order to mitigate the reflections, three modifications are applied and studied, namely:

- **Internal slits**: The highest relative refractive index is between the glass window and air. Assuming that the maximum disturbances are due to refraction of the laser light, the disturbances can be subsided by blocking the refracted rays and only allowing the light sheet to illuminate the measurement domain (usually, 1 mm thick). In order to implement this, a slit is placed between the glass box and the acrylic pipe section. An identical slit is placed on the farther side, after the measurement domain. The image recorded after this modification is shown in the Figure 5.10b. The reflection from the back wall is reduced in the near side of the laser light, but the sharp lines near wall still remain.

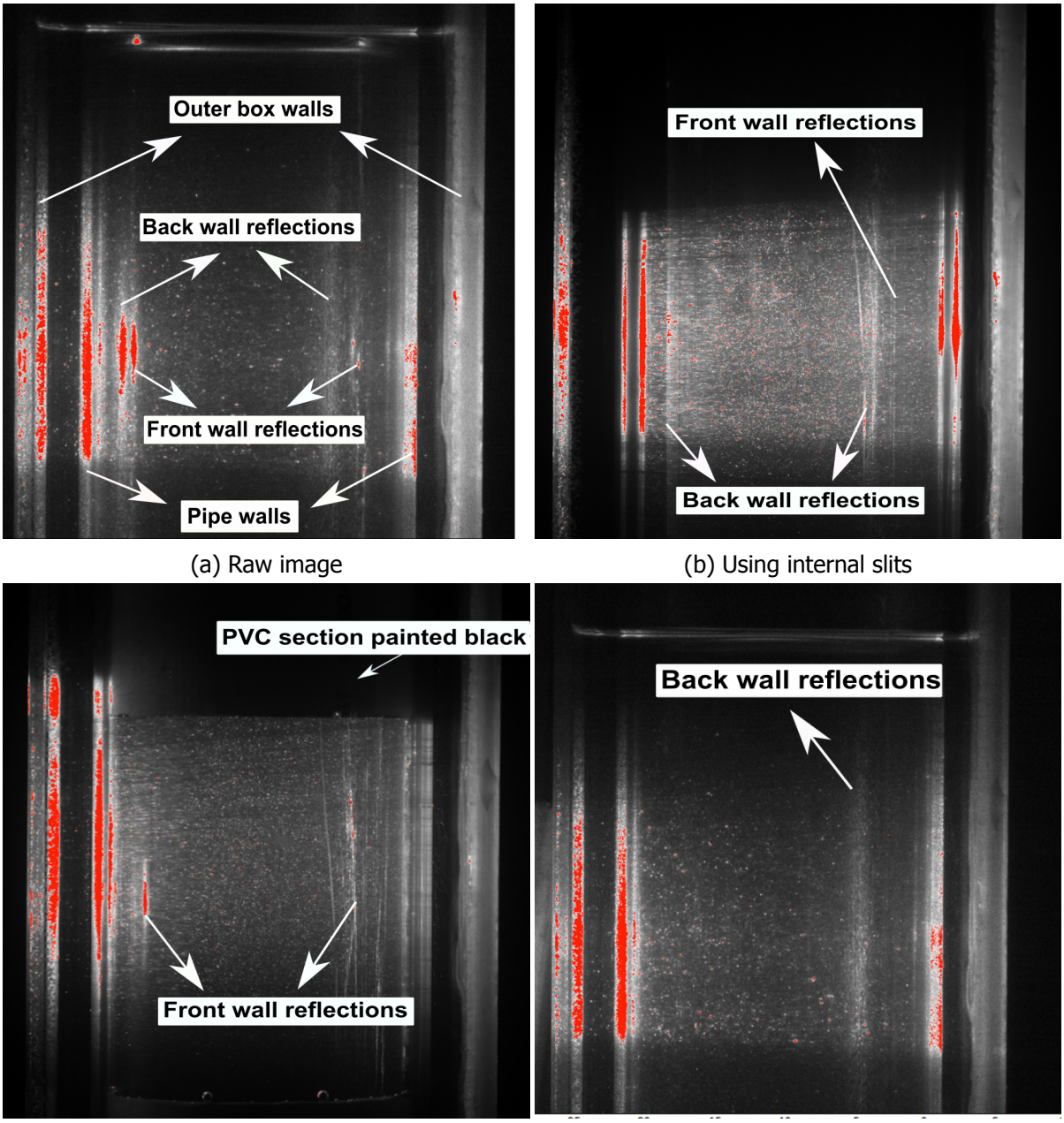

(a) Raw image

(b) Using internal slits

(c) Using the PVC section painted black

(d) Using external slits on both sides

Figure 5.10: Reflections and other optical disturbances observed in the model setup. The laser light path in the images is from left to right.

- **Painting the acrylic surface opposite to the camera black**: The disturbances can also be created by reflection of laser light. One solution to mitigate this is to paint the internal surface of the acrylic section black. Black paint is however highly reflective. A blackboard paint (*schoolbordverf* in Dutch) is used to paint the rear internal PMMA surface black (without obstructing the optical path). The texture of the paint prevents the reflection from the painted surface. The black paint helps in removing the stray light (Outram [44]) from the image and also the texture of blackboard helps in reducing the reflections from the back wall. In order to setup this model, a PVC pipe was cut into half sections, painted black and placed inside the pipe (Figure 5.11). The reflection lines

from the back wall are absent (Figure 5.10c). However, the bright lines from the front wall still remain significant.

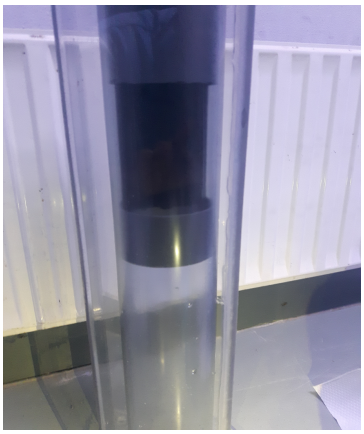

Figure 5.11: PVC section painted black to study reflections.

- **External slits**: Based on an attempt to trace the path of the light contributing to the reflections, the origin of the disturbances appear to majorly originate from the effects of the optical system (Figure 5.10d). The optics produce spread out light around the focused high intense light sheet. The less intense light (spread out light) is intense enough to reflect from the walls of the acrylic pipe to produce the bright lines in the image. In order to prevent this, the path of the spread light is blocked. This can be effectively achieved by using an external slit that only allows light to the measurement domain (aligned with the domain) with a thickness corresponding to the light sheet thickness. In this experiment, a plank is used to obstruct the light sheet (Figure 5.12). The image recorded with this model is shown in Figure 5.10d. The image shows significant improvement. However, a bright line in the far side is still present, which might be due to the reflection from the back of the wall. This bright line is not present in Figure 5.10c, with the black painted PVC section. The effect of optics spreading the high intense light can be seen in Figure 5.12.

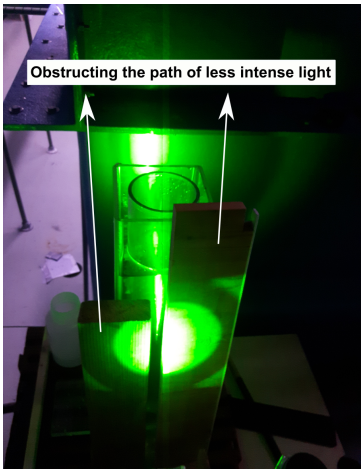

Figure 5.12: The obstruction placed to block the path of the less intense light. The pattern in the obstruction depicts the effect of optics.

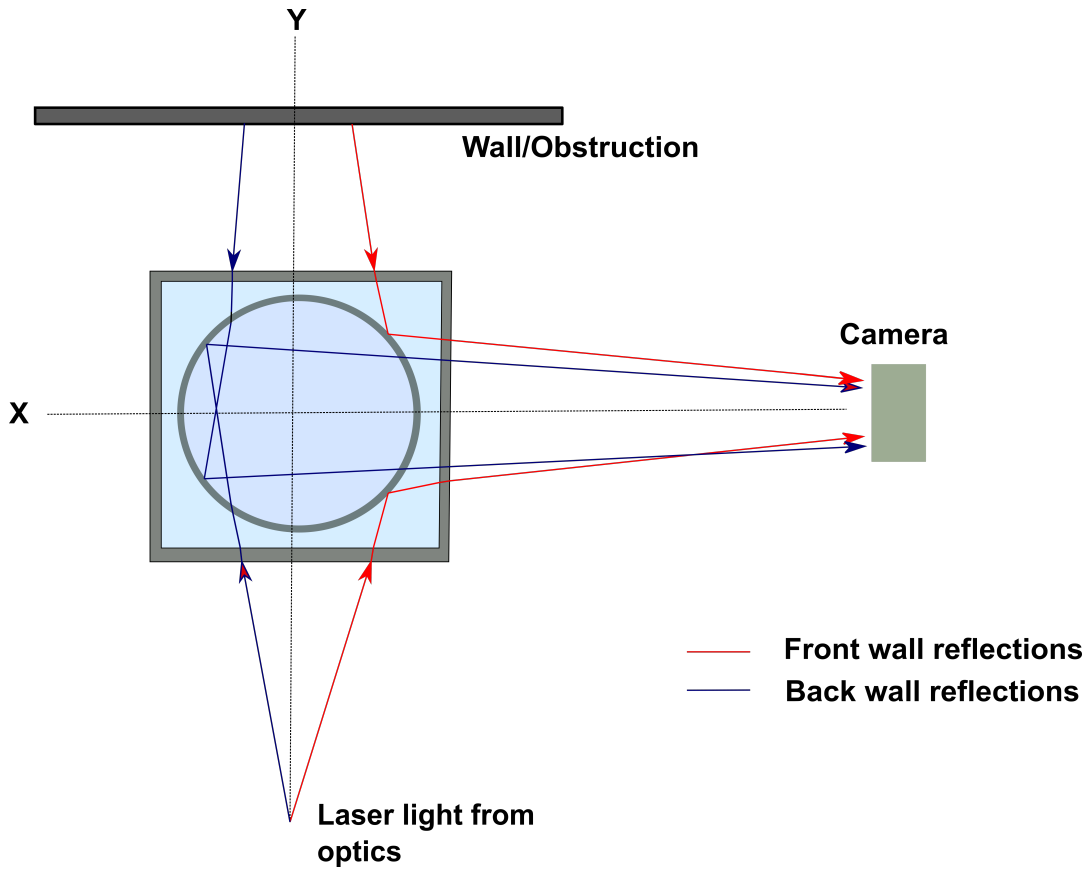

Figure 5.13: Ray diagrams representing the bright lines appearing in the raw PIV images. The picture is not to scale.

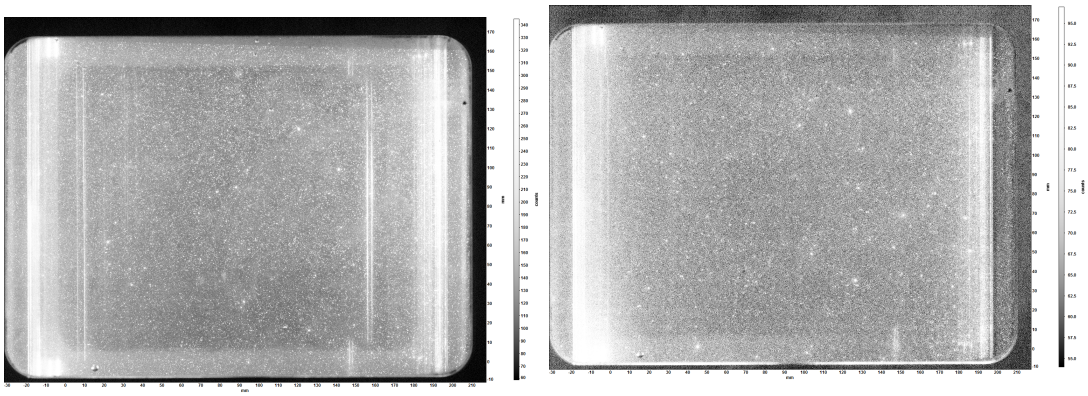

(a) Raw image

(b) Images after using external slits

Figure 5.14: Reflections and disturbances in the Alpha loop PIV images as taken from Davis. The grey scale varies from 200-600 counts.

It is important to note that the internal slit could also effectively obstruct the optical path of the lesser intense light. But the internal slit employed in the mock-up study is thinner and is not able to obstruct the light from the optics that contribute to the reflection. Based on this study, the path of the light corresponding to the bright lines formed in the image is traced and the corresponding ray diagrams are shown in the Figure 5.13. In addition to effect of the optics, the laser light travelling across the field of view might encounter an obstruction which

can reflect back to the field of view causing more reflections. This is observed in the Alpha Loop facility wherein, the pipe downstream of the field of view forms a loop with a section just behind the field of view. The laser light reflects back strongly from the walls of the pipe to the field of wall. This is represented in Figure 5.13. The combination of black paint and external slit can remove the bright reflection lines completely. However, the pipe in Alpha Loop facility is not painted black as the external slits remove reflections effectively near left wall (Figure 5.10d). The flow in pipe is axisymmetric and the results from the left side can interpolated to the region corresponding to the reflections.

5.3. Results and observations

The flow is measured at different Reynolds numbers, all in the turbulent regime. The pressure drop across 6.125 m pipe length, the velocity, and the temperature are measured using a pressure transducer, an electromagnetic flow meter, and a temperature probe. The details on the type and precision of the transducers are given in Appendix C. All the cases measured are tabulated in Table 5.3. The range of the measurements is limited by the installed equipment. The maximum limit is set by the glass windows in the PIV measurement region which is not operated over 2 $bar(g)$ pressure. The flow meter could not measure the flow accurately at lower velocities. The results and observations are discussed further with the following structure: Firstly, the transducer measurements are reported and the pressure drop measurements are compared with the Blasius friction law. The pressure gradient from these measurements are used to normalize the variables obtained from PIV measurements in the near wall region. The PIV results are reported later following the ensemble correlation approach.

Table 5.3: Different cases measured; the flow rate is varied by adjusting the pump frequency.

Case	Flow rate (lps)	Reynolds number	Pump frequency (Hz)
1	50.74	337496	15
2	57.37	378839	16
3	69.33	462454	18
4	73.32	495855	19
5	85.53	551839	24
6	97.44	622033	25

5.3.1. Pressure drop and friction factor - From transducer measurements

Data from the transducers are acquired using Delft-Measure 2, an in-house Deltares hardware and software system. The device can measure voltage in the range 0-10 $Volts$ DC. The voltage inputs are converted to the physical units based on the calibration of the respective transducers. A sample of acquired raw pressure drop measured over a pipe length of 6.125 m, and the corresponding flow rates are shown in Figure 5.15.

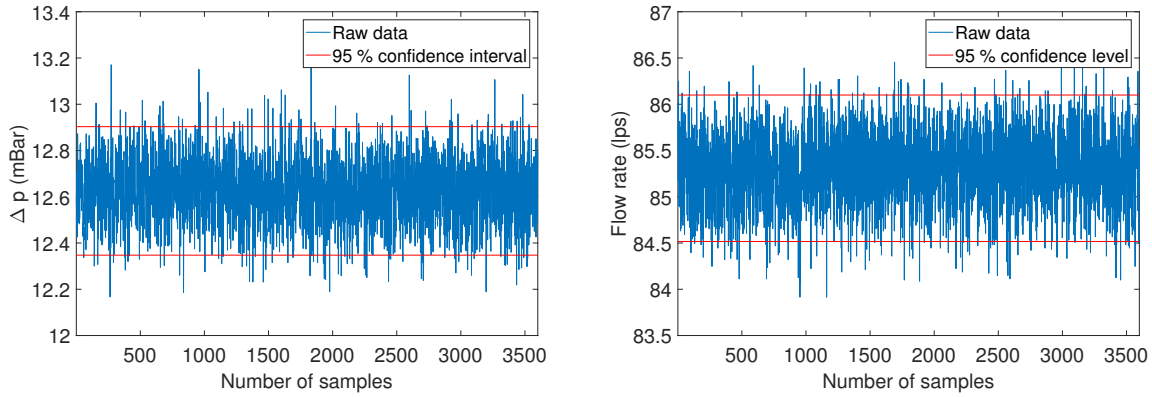

(a) (b)

Figure 5.15: Raw pressure drop (measured over a pipe length of 6.125 m) and flow rate signals measured, along with the confidence level considered for filtering at an average Re = 5.52 x 10^5.

The data is acquired simultaneously with the PIV image acquisition for more than 3600 seconds at a sampling frequency of 1 Hz. Such a long series removes the effect of high frequency noise effectively. The data is further filtered by performing an amplitude domain analysis with 95% confidence level (Figure 5.15). The maximum uncertainties in ΔP and Q observed are 0.38 Pa and 0.0154 lps respectively.

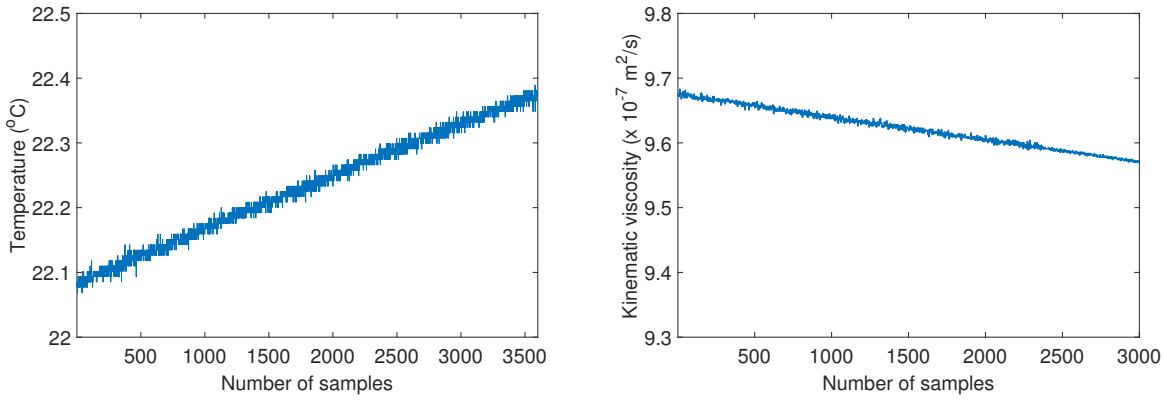

Figure 5.16: Variation in temperature and kinematic viscosity over a PIV measurement series at an average Re = 5.52 x 10^5.

The temperature of the fluid is observed to vary throughout a single PIV measurement. The temperature variation is linear with time as shown in the Figure 5.16. The change in the temperature throughout the measurement series lies in the range 1.2-1.5% for all the cases. This variation further affected the kinematic viscosity of the fluid and the Reynolds number (Figure 5.17), with both of them being functions of temperature. The change in kinematic viscosity and Reynolds number is estimated to be in the range 1-1.2% and 1.2-1.5% respectively. The changes in the variables mentioned are well below 2% and thus, the average values are used to characterize the respective variables.

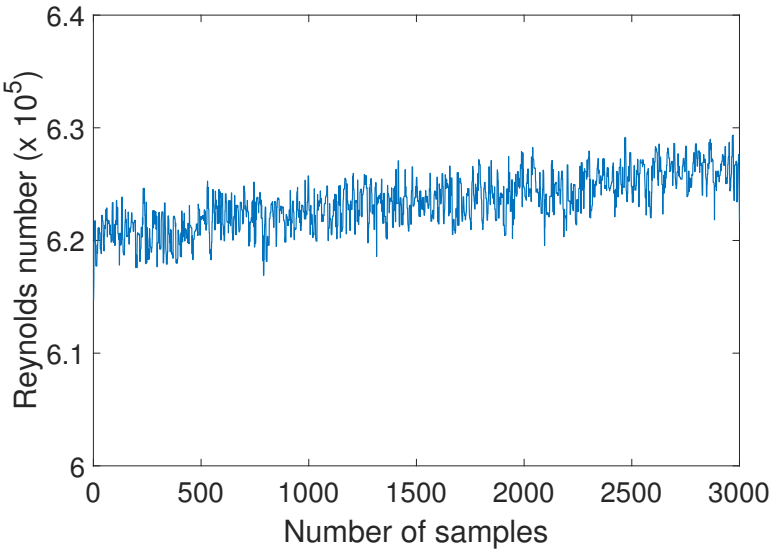

Figure 5.17: Variation in Reynolds number over a PIV measurement series corresponding to Case 6.

The aim of the pressure drop measurement is to estimate the shear stress and eventually the roughness of the pipe to classify if the measurements (Table 5.3) are in the smooth pipe regime. The pressure drop of the fluid in a fully developed pipe flow is balanced by the shear stress acting on the fluid. Based on the pressure drop measurements, shear stress (τ) can be estimated from the relation,

$$\frac{\Delta p}{l} = \frac{4\tau}{d} \tag{5.1}$$

where l is the length of the pipe over which the pressure drop is measured. The *Darcy-Weisbach* friction factor (f_D) can then be estimated from the relation,

$$f_D = \frac{8\tau}{\rho U_b^2} \tag{5.2}$$

where U_b^2 is the bulk velocity of the fluid, given by the ratio of flow rate (Q) and the cross-sectional area of the pipe ($\pi d^2/4$). The Darcy friction factor is dependent on the characteristics of the pipe (diameter, d and roughness, ϵ), the characteristics of the fluid (kinematic viscosity), and the velocity of the fluid flow. *Moody diagrams* (Appendix B) contain charts that map the friction factor as a function of all the parameters mentioned above. The friction factor obtained from the pressure drop and flow rate measurements shows very weak dependency on temperature. The flow rate and the pressure drop influences the friction factor to fluctuate around an almost constant mean. The friction factor estimated is plotted with the average Reynolds number for all the cases, along with the *Moody* diagrams in the Figure 5.18. Figure 5.19 shows a zoomed view of the estimated friction factors in the measured region.

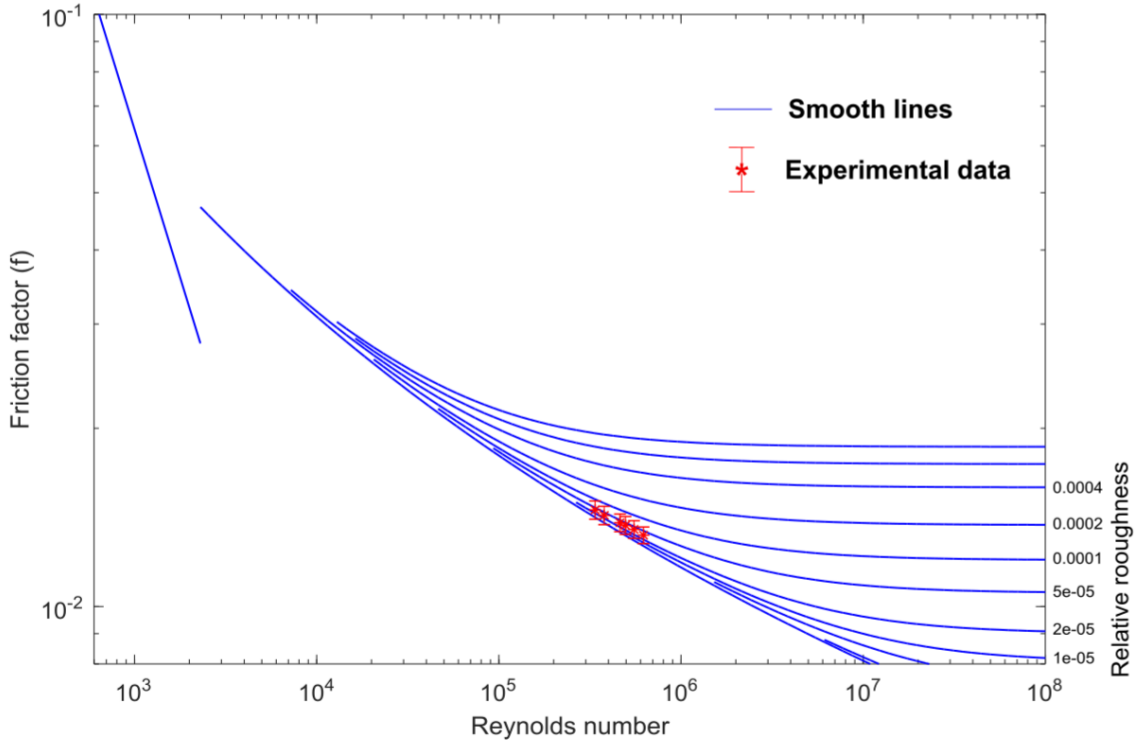

Figure 5.18: The estimated friction factor (f_D) plotted with the average Reynolds number (Re) corresponding to the measurement series, along with the Moody diagram.

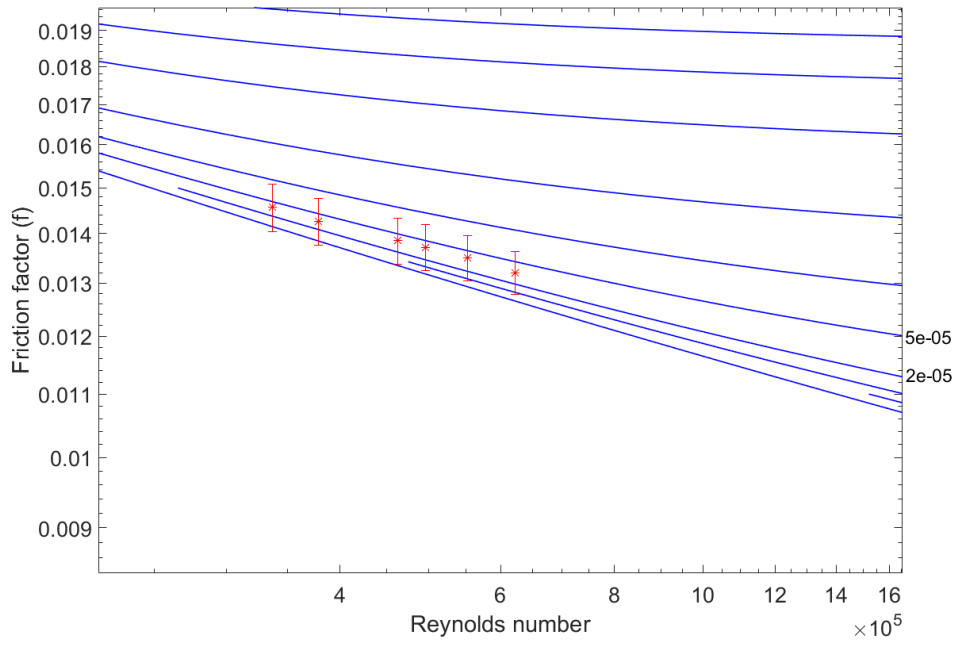

Figure 5.19: The estimated friction factor (f_D) plotted with hydrodynamic smooth lines corresponding to the *Blasius* friction law.

From Figure 5.19, it is evident that the friction factor is decreasing with the Reynolds number, parallel to the lines corresponding to hydrodynamically smooth regime. The

Table 5.4: Important measurement parameters.

Cases		1	2	3	4	5	6
Bulk Reynolds number, Re	*Average*	337496	378839	462454	495855	551839	622033
	Change in Re (%)	3.68	4.49	4.36	3.53	3.23	3.96
Pressure gradient, dP/dx (Pa/m)	*Average*	80.73	101.07	143.36	158.71	212.24	270.55
	Uncertainty	0.255	0.304	0.373	0.400	0.453	0.560
Temperature, T (K)	*Average*	23.29	22.98	23.42	24.02	22.13	21.61
	Change in T (^oC)	0.16	0.31	0.41	0.31	0.28	0.51
Friction factor, f	*Average*	0.0146	0.0143	0.0139	0.0137	0.0135	0.0132
	Uncertainty (x 10^{-3})	0.26	0.25	0.24	0.25	0.23	0.21
Friction velocity, u_* (m/s)		0.0646	0.0723	0.0861	0.0906	0.1048	0.1183
Friction Reynolds number, Re_*		7191	7986	9610	1025	11347	12654
Viscous scale, ν/u_* (μm)		14.36	12.93	10.74	10.07	9.10	8.16

roughness estimated from the friction factor following the *Colebrook-White* equation gives a low estimate of 8-15 μm. From the literature, standard commercial steel pipes have a roughness of 30 - 60 μm [30]. The uncertainty in the friction factor signal measured is very low. However, the diameter of the pipe has a strong influence in the fraction factor ($f_D \sim d^4$). Though the nominal internal diameter of the pipe is 0.2065 m, the pipe has welded areas which tend to change the effective diameter of the flow. The uncertainty in pipe diameter measured with vernier caliper (measured at the ends of the pipe) is 0.5 mm. The effect of this uncertainty in the friction factor is represented in the form of error bars in Figure 5.18 and Figure 5.19.

The maximum uncertainty in the friction factor is 0.26 x 10^{-3}. The highest estimate for roughness is 15 μm, which is still a low estimate for a commercial steel pipe. The important parameters measured and estimated corresponding to the experiment are tabulated in Table 5.4. Generally, a pipe is considered smooth at a particular Reynolds number if the roughness of the pipe is less than the thickness of the viscous sublayer ($y^+ \approx 5$). The thickness of the viscous sublayer for the highest measured Reynolds number is approximately 40 μm which is higher than the roughness estimated. Thus, the flow can be assumed be in the hydrodynamically smooth pipe regime.

5.3.2. PIV measurements

The PIV frame pairs are obtained at an acquisition rate of 5 Hz. The double frame double exposure system is used to record 20,000 image pairs for all the measured cases (Table 5.4). Based on inferences from the study on reflections, the external slits are positioned at the opposite faces of the glass box along the laser light path. A sample of the PIV image pair acquired is shown in the Figure 5.20.

The mean intensity of the laser light is observed to vary throughout a measurement series. In order to reduce this variation across one series, 20,000 image pairs are recorded as 4 sets of 5000 image pairs. The laser intensity varies over the 5000 images as well, but the variation is relatively very small compared to the exposure of particles. The first 200 images of every

set has relatively high laser intensity compared to the remaining 4800 images. Thus, only 4800 images in every set are considered for processing. The variation in the intensity of 4800 images for Case 5 (Table 5.4) is shown in the Figure 5.21. Also, the mean intensity of the first and the second exposures are different for all the cases measured.

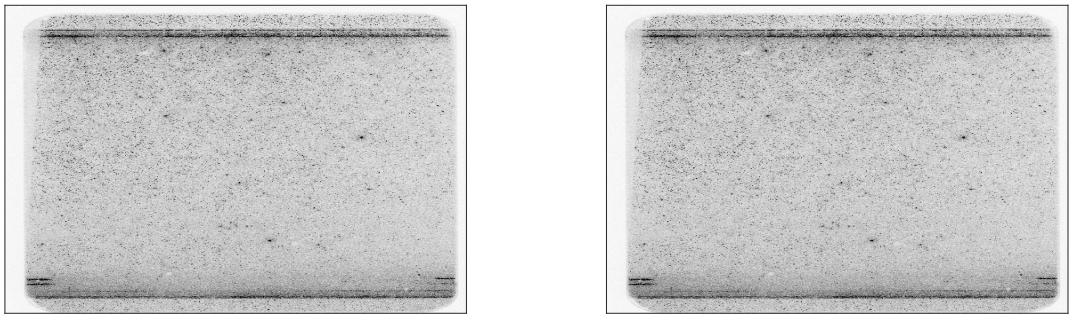

(a) First exposure. (b) Second exposure.

Figure 5.20: The raw PIV image pairs corresponding to Re = 5.52 x 10^5. The inverted grey scale varies from 0-600 counts.

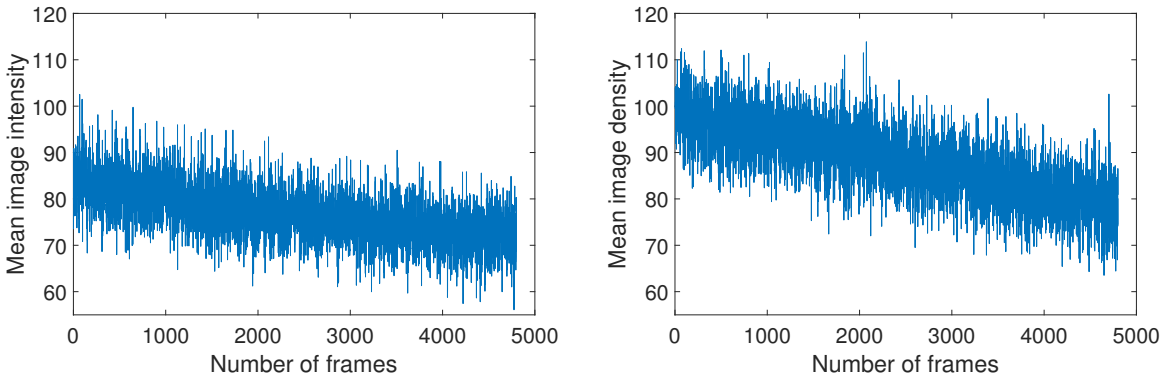

(a) Exposure 1. (b) Exposure 2.

Figure 5.21: The mean image intensity counts of 4800 frames, corresponding to Re = 5.52 x 10^5.

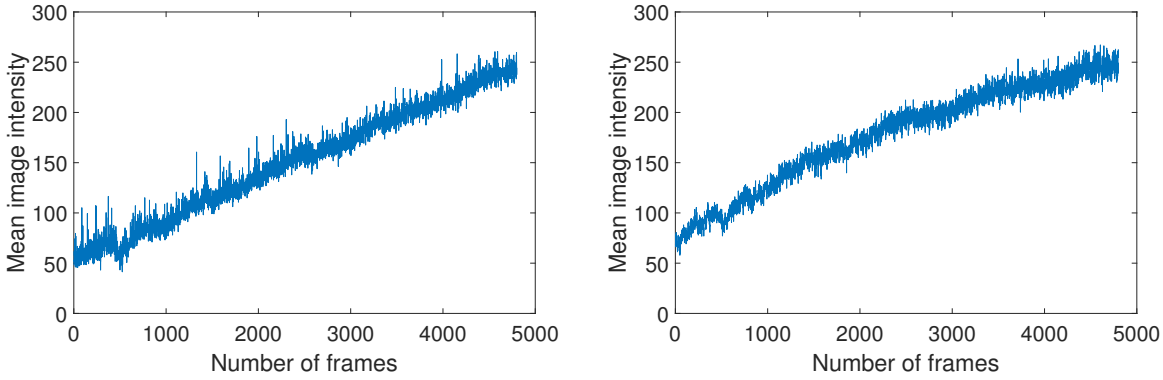

(a) Exposure 1. (b) Exposure 2.

Figure 5.22: The mean image intensity counts of 4800 frames, corresponding to Re = 3.79 x 10^5 (Case 2).

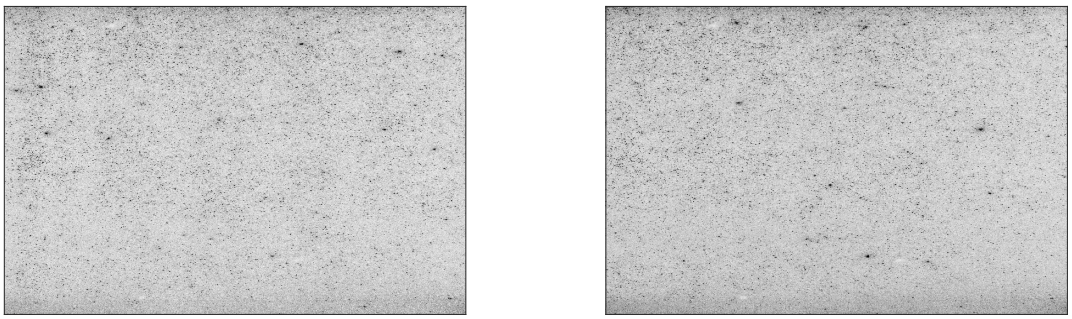

(a) Exposure 1. (b) Exposure 2.

Figure 5.23: The filtered PIV image pairs used for interrogation corresponding to Re = 5.52 x 10^5 (Case 5). The inverted grey scale varies from 0-600 counts.

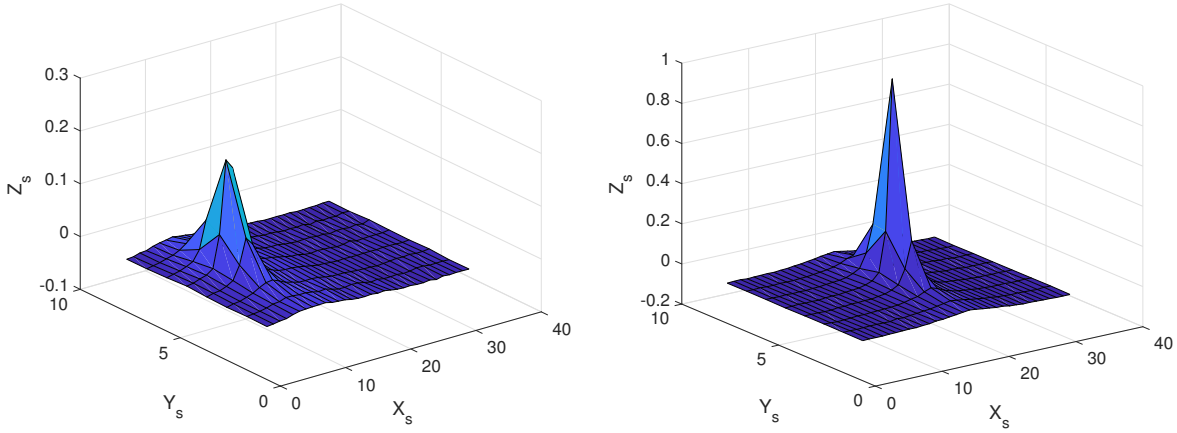

(a) Cross correlation (b) Auto-correlation

Figure 5.24: The ensemble cross-correlation and auto-correlation corresponding to Re = 5.52 x 10^5, in the overlap region.

The PIV measurement corresponding to Re = 3.78 x 10^5 (Case 2, Table 5.4) shows large variations in the mean intensity which makes the series unfit for processing (Figure 5.22).

The raw images are masked so as to remove the walls from vector processing, and the quality is further improved by subtracting the minimum of every pixel in all the 4800 images used (using Davis). The images obtained after implementing this filter are shown in Figure 5.23. The frame pairs are interrogated with single pass interrogation of 8 x 32 windows with 50% overlap. The window size is 8 pixels in the wall-normal direction which improves the resolution in near wall region. The physical dimension of one window is 1.45 x 5.79 mm^2. This process yields 14178 velocity vectors (278 x 51), and the vectors are filtered with a median filter applied in 3 x 3 vicinity of every interrogation window. The fraction of spurious vectors is less than 5%. The spurious vectors are dominant near the wall on the far side of the pipe away from the optics. The time delay between two exposures is varied such that the particle displacement is in the range of 8-12 pixels. The camera frame rate and the laser pulse rate is synchronized by using Davis software. The ensemble correlation of 4800 image pairs provides a very high signal to noise ratio even near the wall region (Figure 5.24). Thus, all the cases have been ensemble averaged over 4800 frame pairs. The quality of the measurements near the wall at the far side of the pipe (left side in Figure 5.14) contains noise due to the glaring near the wall. However, the data at the near side of the wall has sufficient quality required for PIV processing.

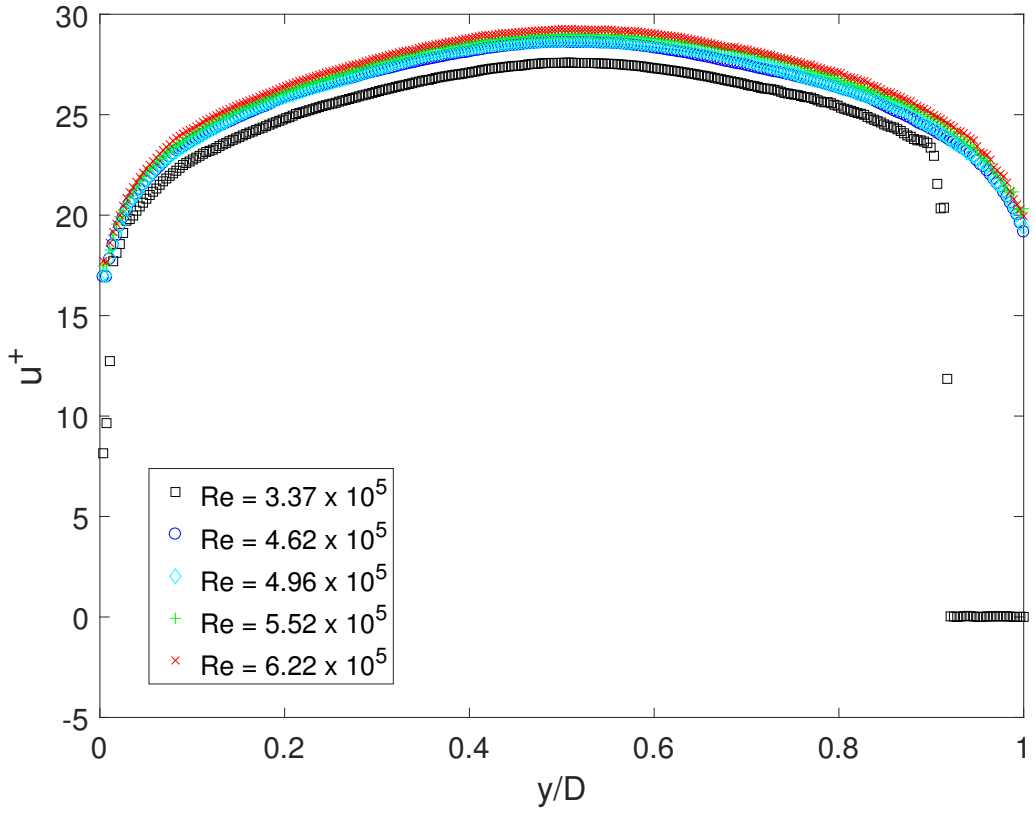

Figure 5.25: Normalized mean velocity (u^+) profiles as a function of y/d for different Reynolds numbers (Table 5.4). The spurious vectors appear (for Case 1) because of absence of the slit on the far side (right in the figure) in Case 1.

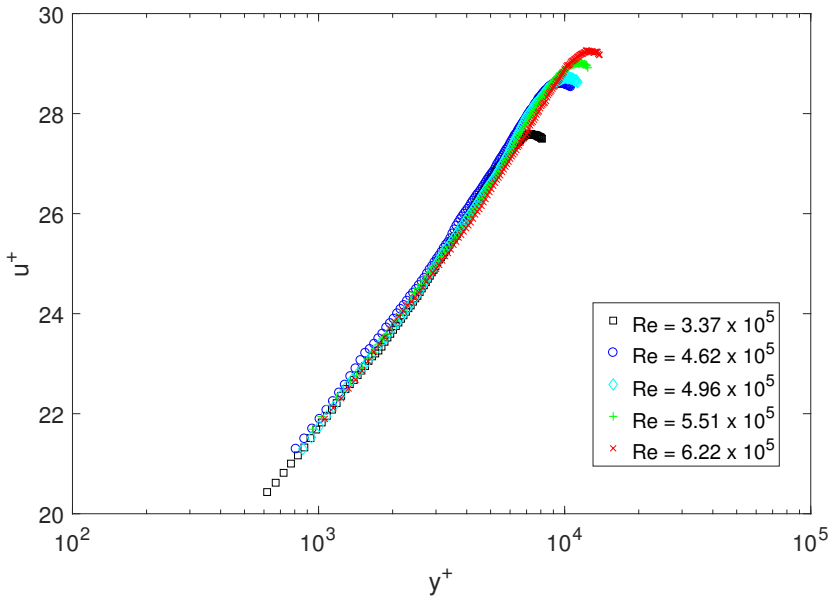

Figure 5.26: The normalized velocity profile (u^+) as a functions of y^+ in a semi-logarithmic scale for different Reynolds numbers (Table 5.4). The logarithmic fit, plotted in the figure results in κ = 0.3855.

The mean velocity is obtained from the displacement peak of the ensemble correlation. The mean velocity of the fluid flow is normalized with the friction velocity (u_*). The normalized mean velocity (u^+) profiles for all the cases measured as a function of distance from the wall are shown in Figure 5.25. The data plotted is obtained by averaging the profiles axially (along the pipe). For the Case 1 corresponding to Re = 3.37 x 10^5, the spurious vectors are predominant in the far side of the wall, resulting in improper velocity estimates. This is because only one slit is used for the Case 1, in the near side. The normalized mean velocity follows a logarithmic profile in the overlap region given by Equation 2.15. The velocity profile is plotted as a function of the wall unit, y^+ in a semi-logarithmic plot, given in Figure 5.26. The profiles for all the Reynolds number overlap, satisfying the Equation 2.15 with a '*Von Kármán*' constant (κ) of 0.3855 and the constant B is 4. The *Coles wake factor* then, is estimated to be 1.544. The core region (y/R > 0.65) follows Equation (2.9) with an estimate of β as 0.13 and u_0 as 3.02 m/s which also corresponds to the centreline velocity. The estimates are in agreement with the literature [42].

In the outer region, according to the defect law, the velocity deficit compared to the centerline velocity (u_{cl}) scales with the length scale, given by Equation 2.16. This profile also agrees with the estimated κ value of 0.3855. The estimate for κ lies within the range given in the literature (0.36-0.42, [42]). Thus, the agreement of mean velocity profiles with literature also reassures the values of u_* obtained using pressure drop measurements. The resolution (0.72 mm) is not sufficient to comment on the velocity profile in the viscous sublayer.

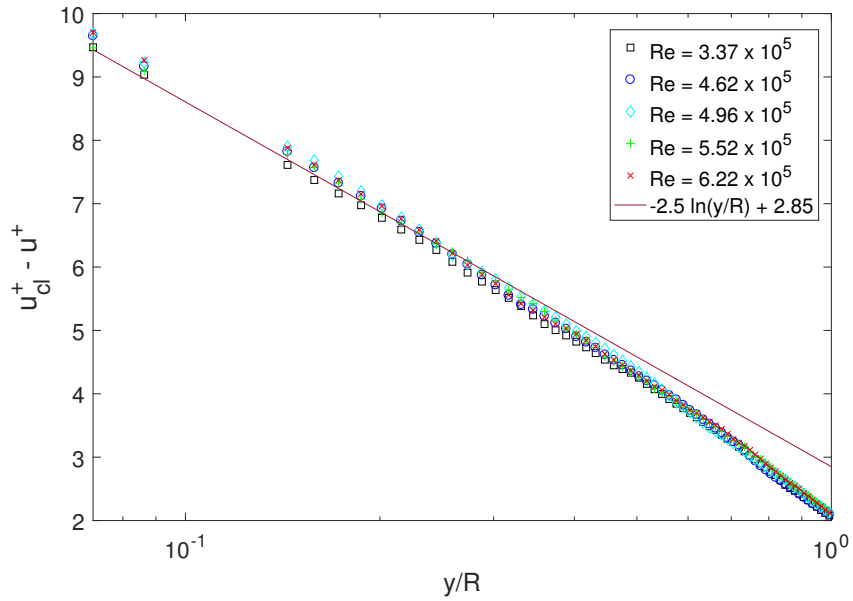

Figure 5.27: The defect law for the pipe flow along with the fit. The superscript '+' indicates the normalized parameters with u_*. The fit corresponds to Equation (2.16) with κ = 0.3855 and B^* = 0.8.

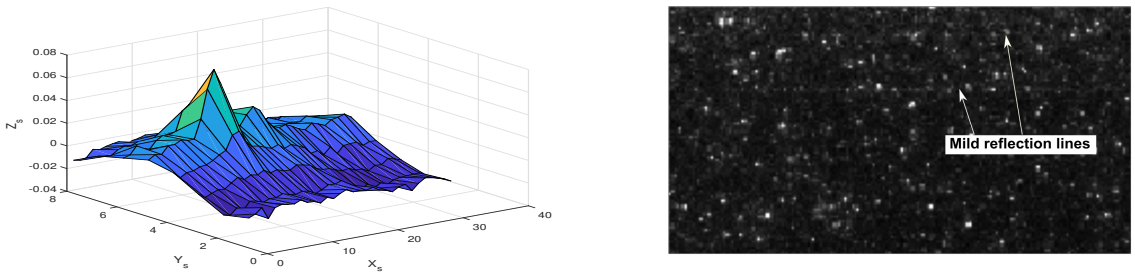

(a) Effect of the reflections in the cross correlation

(b) Mild reflection lines close to wall

Figure 5.28: The corrupted ensemble correlation due to optical disturbances caused by mild reflection lines in the images, corresponding to Re = 5.52 x 10^5.

In order to retrieve the velocity JPDFs from the ensemble correlation, Gaussian profiles are fit as explained in Chapter 3. However, close to the wall, the ensemble correlation has a disoriented shape due to presence of reflections, high exposure, and glaring from the wall. These optical disturbances highly influence the correlation and makes them unfit for retrieving the velocity JPDFs. An example of the affected ensemble correlation is given in Figure 5.28. Ideally, the influence of the disturbances can be removed by subtracting the cross-correlation of mean intensities, given the mean intensities are constant throughout the measurement series. But in this case, the variation in the mean intensities does not allow to remove the artifacts of optical disturbances. Hence, the first four interrogation windows from the wall are removed from the evaluation of turbulent stresses. Also, the reflection lines present across the regions corresponding to 8^{th} and 9^{th} interrogation windows (Figure 5.28) provided spurious values while evaluating the moments. Note that the shape of ensemble correlation is corrupted by the displacement peak is still large enough to provide the displacement data. Thus, though the spatial resolution is 0.72 mm, the data nearest to the wall is 3.6 mm away from the wall.

The velocity JPDFs of all other interrogation windows are estimated using a 5 x 9 rectangular filter. The normalized Reynolds shear stress ($\overline{uv}$) obtained is plotted as a function of y/R in the Figure 5.30. The obtained profiles are averaged over the length of the pipe optically accessible. In contrast to the literature, where the Reynolds shear stress is linear with y until very close to the wall, later converging to zero (Figure 5.29), the shear stress profiles are non-linear. The Reynolds shear stress is underestimated over a large part of the pipe radius. The origin of this effect is might be due to the inaccuracy of ensemble correlation to detect smaller values of stresses. The shapes of the ellipse formed by fitting Gaussian is shown in the subsequent Figure 5.31.

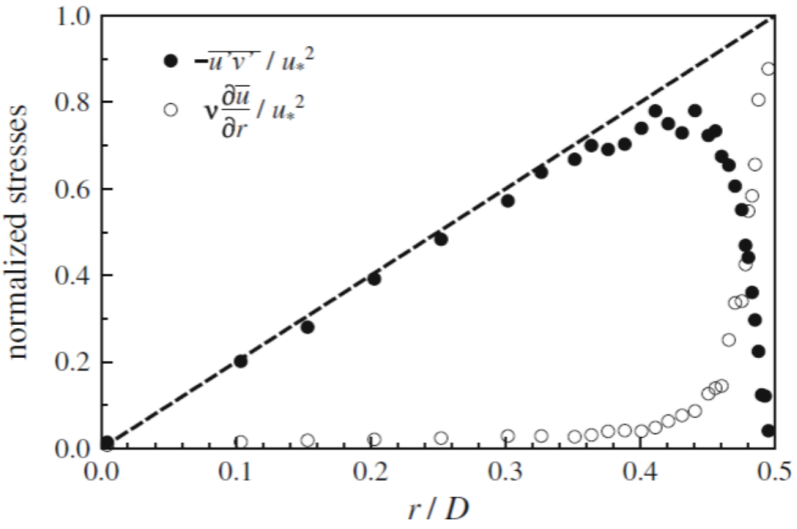

Figure 5.29: The normalized Reynolds stress ($\overline{u'v'}/u_*^2$ in figure) and the viscous stress ($\nu\partial\overline{u}/\partial r/u_*^2$) profiles in a turbulent pipe flow at Re = 10,000 (Den Toonder et al. [15]).

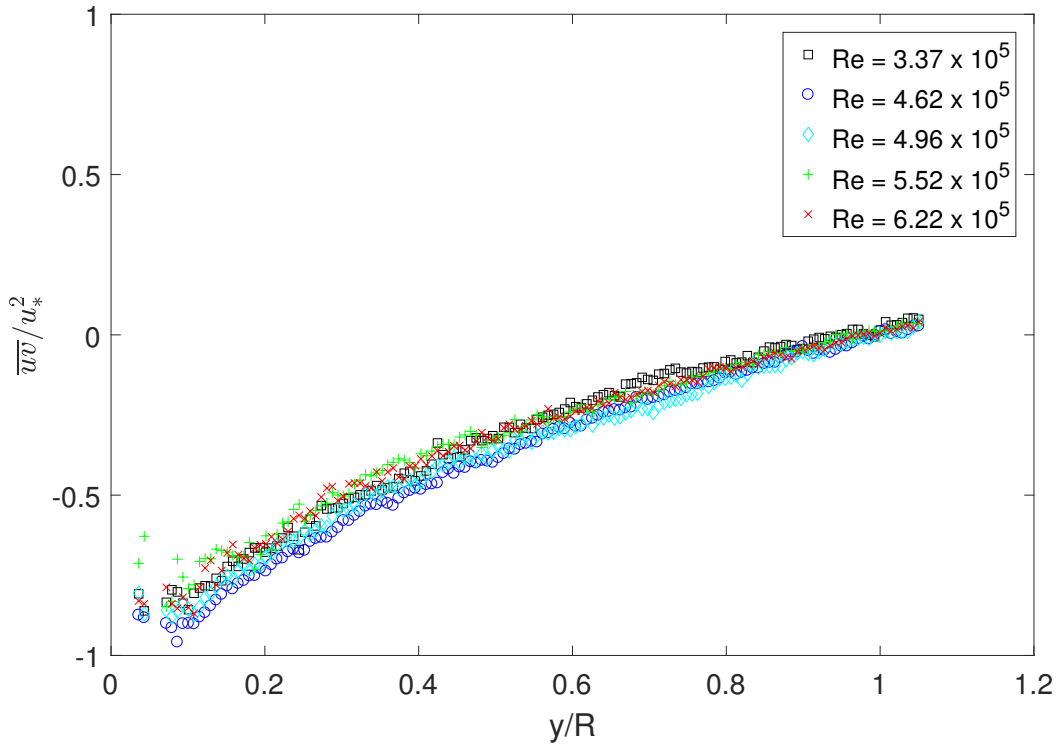

Figure 5.30: Normalized Reynolds shear stress as a function of y/R, plotted for different Reynolds numbers (Table 5.4).

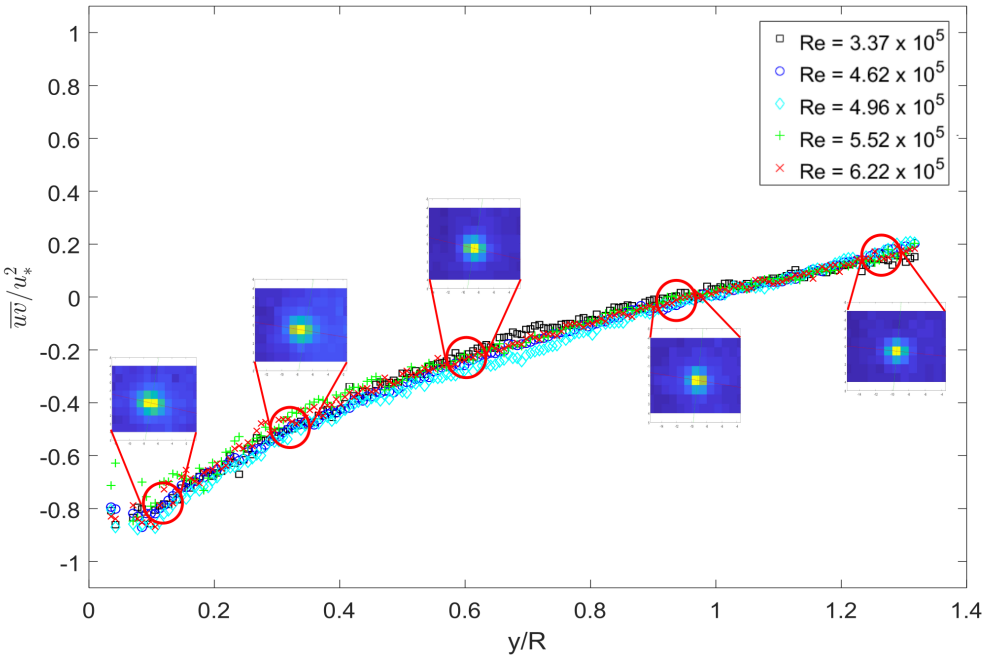

Figure 5.31: Normalized Reynolds shear stress vs y/R, with the shapes of the Gaussian fits at various positions. The shape is almost symmetric near the centre of the pipe (y/R ≈ 1). The shape is broadened near the wall (y/R « 1).

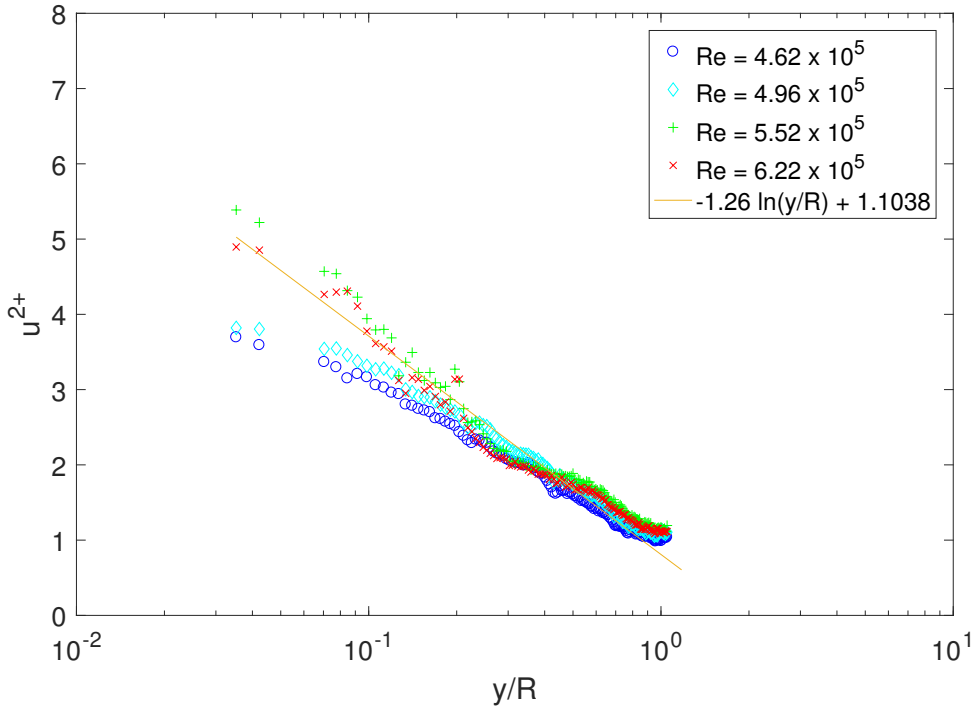

Figure 5.32: Normalized streamwise turbulent fluctuations (u^{2+}) as a function of y/R, plotted in a semi-logarithmic scale for different Reynolds numbers (Table 5.4). The fitted line corresponds to Equation (2.17) with A_1 = 1.1038 and B_1 = 1.26.

The streamwise turbulent fluctuations (u^{2+}) obtained in a similar fashion, are plotted in Figure 5.33 as a function of y/R. The profiles are averaged over the length of the pipe optically accessible. The streamwise fluctuations follow a logarithmic profile with A_1 = 1.26, and B_1 = 1.1038. This is in agreement with Hultmark et al. [20]. However, the fluctuations at highest two Reynolds numbers are overestimated compared to the fit, which is in contrast with the literature (Figure 2.4). The streamwise turbulent fluctuations are plotted as a function of y^+ (Figure 5.33). The fluctuations corresponding to Re = 3.37 x 10^5, Re = 4.62 x 10^5, and Re = 4.96 x 10^5 follow similar trend. In the region between y^+ = 3 x 10^4 and 10^5, the highest two Reynolds number show bias, leading to the sudden increase. Though the resolution is enough to capture the region corresponding to the outer peak observed in literature (Figure 2.6), the reflections dominate this region and the data is not sufficient to predict the profiles in this region.

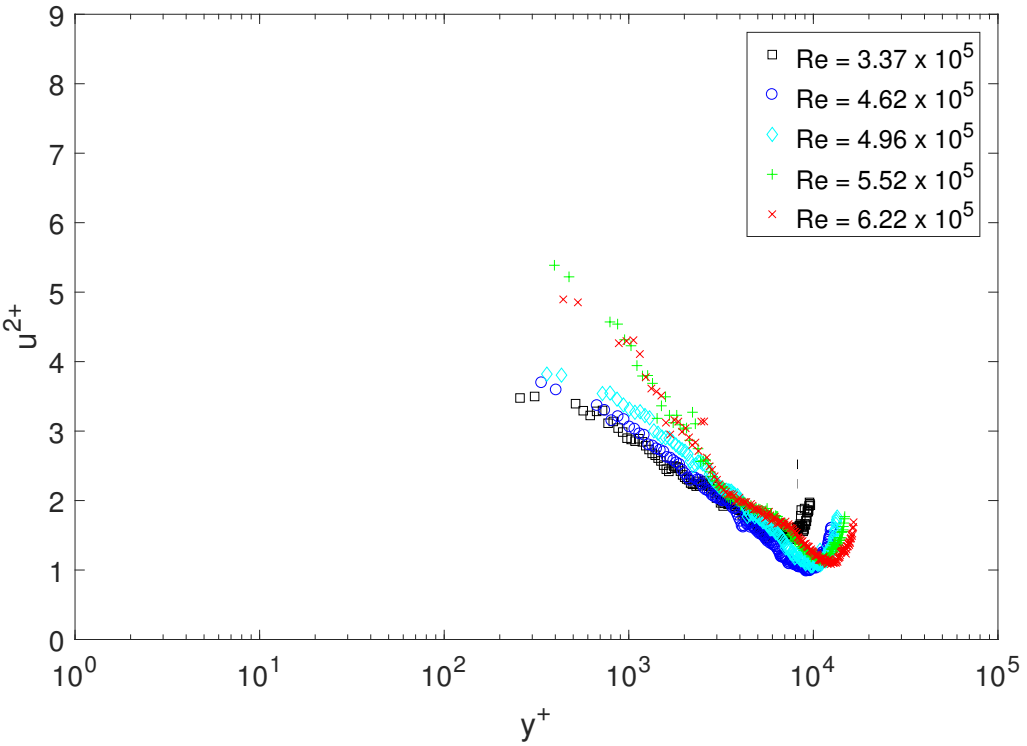

Figure 5.33: Normalized streamwise turbulent fluctuations (u^{2+}) as a function of y^+, plotted in a semi-logarithmic scale for different Reynolds numbers (Table 5.4).

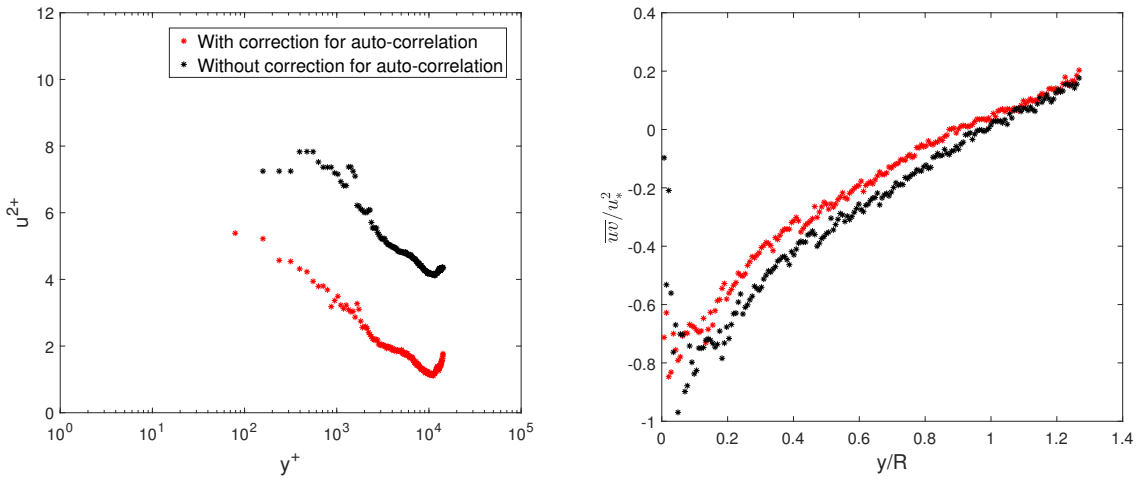

(a) Streamwise fluctuations vs y^+.

(b) Reynolds shear stress vs y/R.

Figure 5.34: The stresses retrieved from the shape of the ensemble correlation with correcting for auto-correlation (represented by *), and without correcting for auto-correlation (represented by *). The profiles correspond to Re = 5.52 x 10^5.

The correction for auto-correlation is applied in the previous estimates of the stress profiles. Figure 5.34 shows the plots for stream fluctuations and Reynolds shear stress with and without corrections. The trend without the correction is over-predicted as expected. The second moments for auto-correlation is observed to be symmetric and uniform throughout

the measurements, with a constant value of 0.62 $pixels$ (RMS of 0.012 $pixels$).

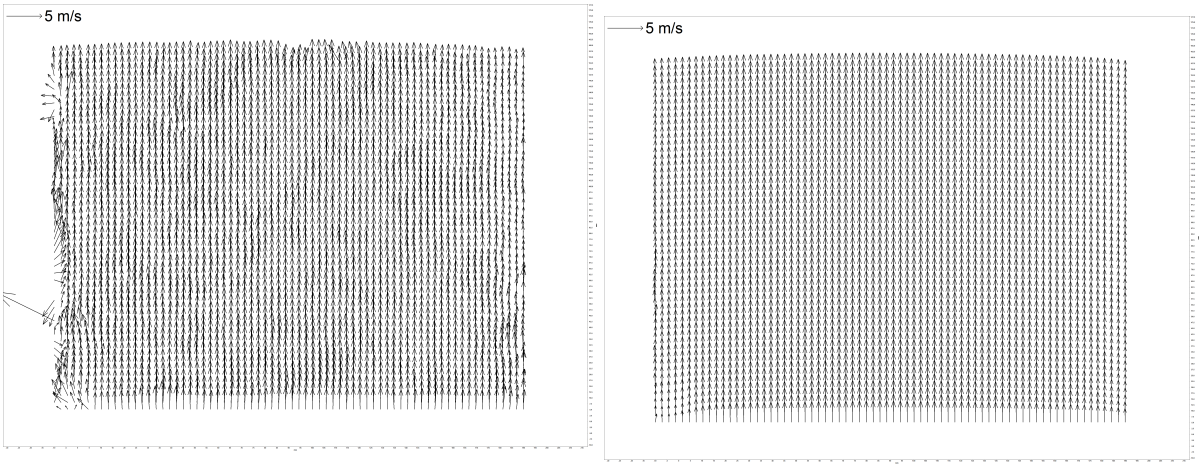

(a) Instantaneous velocity field

(b) Mean velocity field

Figure 5.35: Velocity vector field using 32 x 32 interrogation window. The velocity field correspond to Re = 5.52 x 10^5.

In order to compare the results with conventional PIV analysis, Case 5 is processed using the conventional analysis using Davis. The image pairs are preprocessed with min-max filter (in Davis). The image pairs are interrogated with two-pass interrogation technique with 64 x 64 pixel interrogation windows as the first pass and 32 x 32 pixel interrogation windows as the second pass. The vectors are filtered by applying the universal outlier detection applied to 3 x 3 windows (Figure 5.35). The fraction of spurious vectors is less than 3%. The mean velocity obtained is plotted along with mean velocity obtained from ensemble correlation shown in the Figure 5.36. The plots obtained from both techniques overlap for a large part part with a maximum bias of 0.86 $pixels$ between them. The bias is only observed at y/R < 0.6.

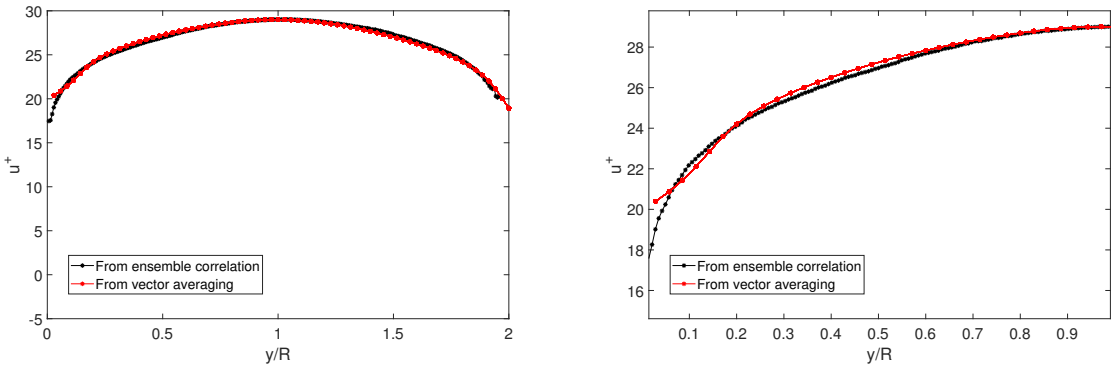

(a) (b)

Figure 5.36: The mean velocity profiles at Re = 5.52 x 10^5 (Case 5) as a function of distance from the wall (y/R) obtained using ensemble correlation (represented by —), and vector averaging (represented by —). Maximum bias between the profiles from the two methods is 0.86 $pixels$.

The stresses are also obtained from the conventional PIV analysis. The plots comparing the stresses obtain from both the approaches are given in the Figure 5.37.

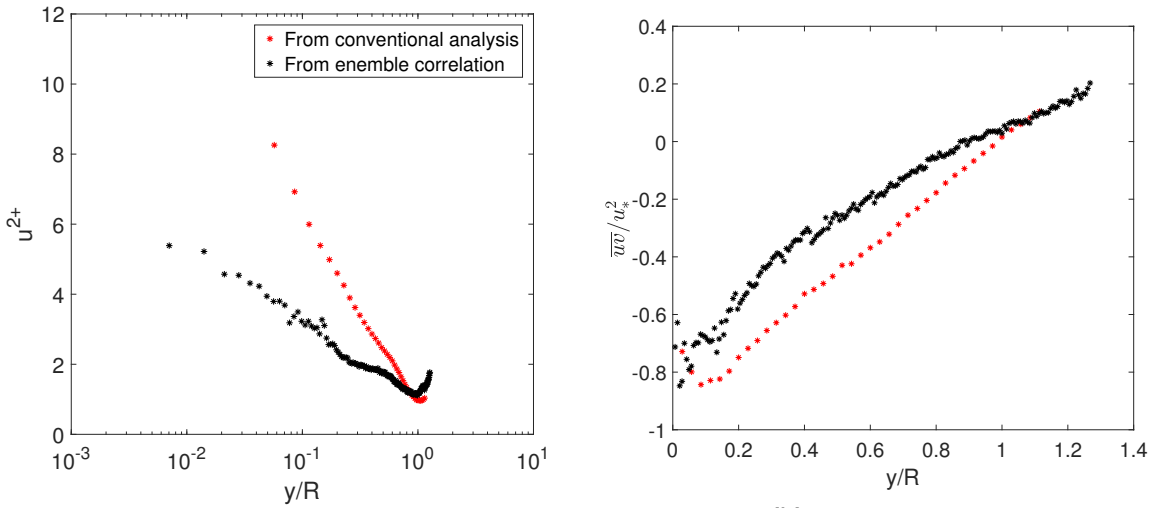

(a) Streamwise fluctuations

(b) Reynolds shear stress

Figure 5.37: The estimated stresses as a function of distance from the wall (y/R), retrieved from the shape of the ensemble correlation (represented by *), and using the conventional PIV analysis (represented by *). The plots correspond to Re = 5.52 x 10^5 (Case 5).

The streamwise fluctuation obtained from the conventional analysis is over estimated. The estimates for logarithmic profile fits are A_1 = -2.1 and B_1 = 0.8375. However, the Reynolds shear stress follows a linear profile as expected, in contradiction with the results from ensemble correlation approach.

5.4. Inferences

The high Reynolds number experiments are performed in the Alpha Loop facility, achieving a maximum Reynolds number of 6.2 x 10^6. Based on the pressure drop measurements, the roughness of the pipe is estimated to be 8-15 μm. The measurements are in the smooth pipe regime. The study on reflections helps in reducing the reflections in the facility with the use of external slits. However, the disturbances very close to the wall still remain significant thereby reducing the quality of measurements in these regions. The normalized mean velocity profile (u^+) follows the profile given by,

- Overlap region:

$$u^+ = \frac{1}{0.386} ln(y^+) + 4. \tag{5.3}$$

- Core region:

$$u^+ = u_{cl}^+ - \frac{2}{3}\frac{1}{0.13}\left(1 - \frac{y}{R}\right)^{3/2}. \tag{5.4}$$

The equations are represented in similar format as Equation (2.9) and Equation (2.15). The value of κ is estimated to be 0.3855. From the retrieved velocity JPDFs, the streamwise fluctuations and the Reynolds shear stress are estimated. The Reynolds shear stress is underestimated compared to the results from conventional analysis. The logarithmic profile followed by the normalized streamwise fluctuations (u^{2+}) is given by,

$$u^{2+} = 1.1 - 1.26\ ln\ \frac{y}{R}. \tag{5.5}$$

The u^{2+} profiles for highest two Reynolds numbers appear to be overestimated.

6

Conclusions and Recommendations

The work in the current thesis has focused on achieving high spatial resolution with PIV using ensemble correlation. The turbulent stresses are recovered from the shape of the ensemble correlation by fitting a Gaussian profile. The main contribution of this work is towards resolving smaller scales of turbulence. The measurement technique, with its ability to reach very high spatial resolution, can contribute to the study on wall turbulence at high Reynolds numbers.

The analytical description of the ensemble correlation is provided as a first step. It is assumed that **the ensemble correlation is the convolution of the auto-correlation and the velocity JPDFs**. The ensemble correlation is broadened in regions of high velocity gradients, and symmetric in regions without velocity gradients. In order to retrieve this information, Gaussian profiles are fit and the second moments are estimated from the elliptical shape of the Gaussian profile. Complying with the convolution operation, the orientation of the velocity JPDFs is considered the same as the ensemble correlation. The described technique is applied in two cases: a turbulent jet, and high Reynolds number pipe flow.

The approach is first implemented to study the turbulent jet. The results are validated with the experiments from Westerweel et al. [65], using 657 image pairs. The ensemble correlation near the centre of the jet appeared noisy. The number of images required are not sufficient to provide a distinct peak, especially near the centre of the jet. The predicted turbulent intensity and Reynolds shear stress follow trends similar to the literature at several distances from the jet nozzle. Further, high image density is achieved by acquiring 9000 image pairs from a scaled-up jet experiment. The behaviour of the ensemble correlation is studied at regions with high velocity gradients with the number of image pairs. **The velocity gradients broaden the ensemble correlation**. The shape is disoriented in areas of strong out-of-plane motion. The stresses retrieved from the shape of the ensemble correlation perform better than that obtained by following the conventional analysis. **The broadening of the shape also causes bias in the mean velocity profiles**. The displacement peaks at the regions affected by the strong out-of-plane motion are predicted accurately by the ensemble correlation whereas, the vector averaging predicts incorrectly due to presence of spurious vectors.

Further, the approach is used to study the near wall turbulence at high Reynolds number flow in a long pipe at the Alpha Loop facility. The flow rate, the temperature, and the pressure drop are measured using transducers. The bulk Reynolds number is varied from 3.37×10^5 to

6.22 x 10^5. The temperature varied linearly with time throughout each measurement series. This affected the temperature dependent variables like density and Reynolds number. This introduces uncertainty in the variables which are below 2%. The pressure drop measurements are used to estimate the friction factor. The friction factor is plotted against the Moody lines that contains lines corresponding to hydrodynamically smooth pipe. The roughness is estimated to be in the range of 8-15 μm. In order to study wall turbulence with PIV, optical disturbances due to the glass windows and acrylic pipe are reduced. **Most of the reflections disappear with the use of external slits** on the both side of the field of view along the laser path. The PIV images recorded with this modification, are processed following the ensemble correlation approach. In total, 20,000 images are recorded in each measurement series but, the first 4800 images are only used to estimate the ensemble correlation to reduce the effect of varying variation in laser intensities, the Reynolds number and other variables. The ensemble correlation produces a distinct peak with high SNR. Very close to wall, mild reflections and glaring from the wall corrupts the shape of the ensemble correlation. Though the spatial resolution achieved is 0.72 mm, the region until 2.88 mm from the wall is corrupted.

Table 6.1: Compilation of results from other experimental facilities.

Reference	Flow type	κ	A_1	B_1	Measurement method
McKeon and Morrison [33] *Princeton Superpipe*	Pipe	0.421	1.25	1.61	Pitot/HWA
Monty [37] *Melbourne*	Pipe	0.384	2.25	1.61	Pitot/HWA
Monty [37] *Melbourne*	Channel	0.389	2.20	1.10	Pitot/HWA
Österlund et al. [43] *KTH*	Boundary layer	0.38	-	-	HWA
Current work *Alpha Loop facility*	Pipe	0.386	1.26	1.10	PIV

The normalized mean velocity profiles are estimated both from the peaks of the ensemble correlation and from averaging the instantaneous velocity vectors. In the overlap region, there is a bias between the velocity profiles from both methods with a maximum bias of 0.86 $pixels$. The mean velocity follows logarithmic profile for all the Reynolds numbers measured. The **'*Von Kármán*' constant is estimated to be 0.3855** by fitting a line corresponding to the deficit scaling law in velocity. **The Reynolds shear stress retrieved from the shape of ensemble correlation is underestimated** and does not follow a linear profile. The streamwise fluctuations obtained, follows a logarithmic profile in agreement with the literature [20]. However, the highest two Reynolds numbers appear overestimated compared to the fit. This might be due to the reported difference in orientation of ensemble correlation and velocity JPDFs (Scharnowski et al. [51]). Table 6.1 shows the estimates obtained from other facilities as well as the estimates in the current work.

The thesis showcased that the turbulence statistics can be retrieved from the ensemble correlation. The camera images the pipe completely in the current study as an initial attempt to apply the followed technique at high Reynolds numbers. The field of view can however be focused in the near wall region to further increase the spatial resolution provided that the disturbances due to reflection of light are removed.

6.1. Recommendations

The work presented in this report is an initial attempt to address the issues at high Reynolds number pipe flows. There is a large scope for future work, even with the acquired data as a part of the experiments conducted. This section is divided into two subsections with an intention to separate the recommendations to improve the processing technique, and the test facility.

6.1.1. On the processing technique

- The Single Pixel Ensemble correlation (SPE), according to literature [23] performs superior to ensemble correlation provided the image density achieved can provide strong displacement-correlation peak. With the available resolution, SPE, if implemented could resolve regions near to the suspected second peak (1-3 mm away from the wall). However the reflections in this region still remain a problem.
- The effect of reflections in the correlation can be reduced by removing the correlation of mean intensities. This process could not be implemented in the current work because of the fluctuations in the mean intensities throughout the measurement series. However, this process can be carried out for cross-correlation of each image pair, then followed by ensemble averaging.
- The underestimated Reynolds shear stress might be due to the suspected difference in the orientation of ensemble correlation and the velocity JPDFs. The bias in the orientation can be studied by artificially introducing the bias and comparing it with the conventional analysis [51].
- The ensemble averaging in the current work is carried out by interrogating windows of same size. A bigger second window can be chosen, especially when the first window is very small. This would effectively capture the velocity gradients, and also would perform superior while fitting a Gaussian profile.

6.1.2. On the test facility

- The fluid properties varied throughout the measurement series due to viscous dissipation. The temperature of the fluid can however be kept constant with the help of a Heat Exchanger (similar to the cooling unit used by Willert et al. [68]). This would reduce the uncertainties in temperature dependent properties.
- The pressure drop, flow rate and the temperature are measured at a single position in a 350 m long pipe. Measuring the variables at different positions reduces the uncertainties and could be vital in estimating surface roughness of the pipe.
- The surface roughness of the pipe could be estimated directly using microscopy techniques. This would give feedback to the results from pressure drop measurements.
- The reflections observed in the PIV images can further be reduced with painting the surface (opposite to the camera view) of the pipe black. Also the glaring from the walls can be reduced by physically masking the walls from the field of view. In literature, the reflections are completely avoided by using a mirror slightly protruding into the pipe by Willert et al. [68]. However, the disadvantage of this technique is that it is intrusive and the mirror can affect the flow.
- Air bubbles are observed to accumulate in the glass box in the optical section. An accessory can be provided, which acts as a drainage to flush out the bubbles from the glass box.

- Even with focusing the camera to the near all region, the resolution is limited by the thickness of laser sheet (0.8 mm in the current work). A thin laser light sheet is necessary to reach higher resolution.

A

Appendix A: Issues with camera

In the experiment to study the turbulent jet (Chapter 4), the images are recorded by *Imager HS 4M*, a 12 but digital camera. The images (9000 images) are acquired at a frame rate of 630 Hz (single exposure system). The interrogation of successive image pairs (say I_1 and I_2 produce corrupted cross-correlation. The cross-correlation has minimum value at the centre regardless of the position of the displacement peak. On subtracting the mean intensity of the interrogation windows from the actuality intensity, the obtained cross-correlation has zero mean. This produces distinct negative values of correlation at the centre. Figure A.1 depicts this cross correlation (R_{avg}) time averaged over 1000 frames.

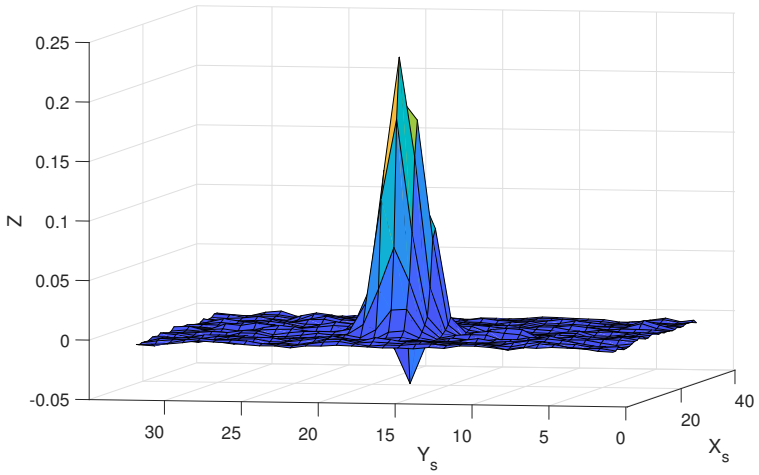

Figure A.1: The cross correlation is minimum at the centre corresponding to zero displacement.

The negative values of correlation disappears if the following factor of first exposure is subtracted from the second exposure. This factor is the negative value at the centre of cross correlation. The centre of the cross correlation is at (17,17) which corresponds to zero displacement between the two exposures.

$$I_2' = I_2 - I_1 R_{avg}(17,17) \tag{A.1}$$

The cross-correlation of I_1 and I_3 is shown in Figure B.1

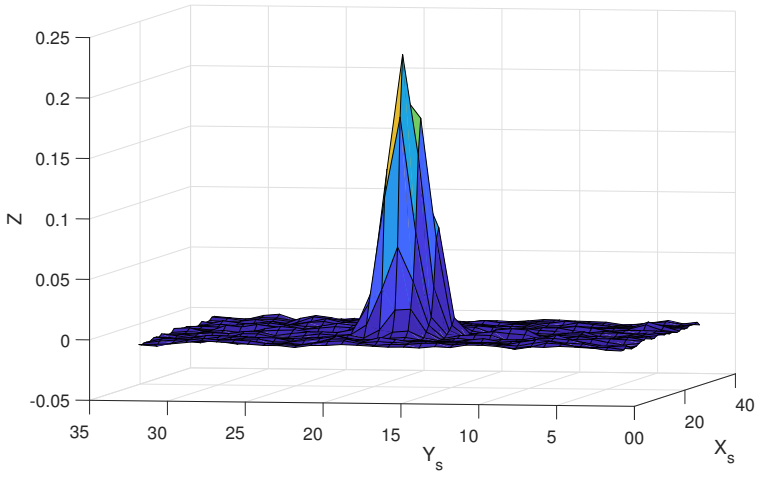

Figure A.2: The cross correlation of first exposure and modified second exposure.

In areas where the displacement peak is away from the centre of cross-correlation ($\Delta s > 0$), the negative values occur. The area over which the negative values occur have strong velocity gradients. This is shown in Figure A.3.

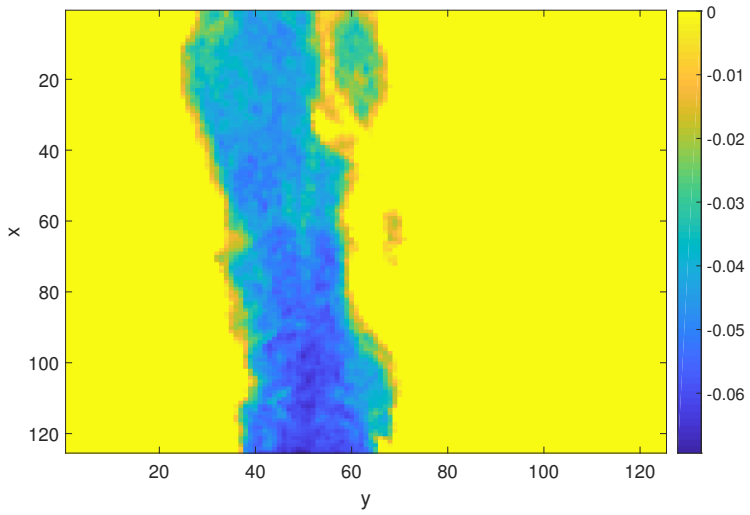

Figure A.3: The region over which the centre of the ensemble correlation have negative values. The region is also where the turbulent jet flows. The colourmap indicates the value of the correlation at zero displacement.

B

Appendix B: Moody chart

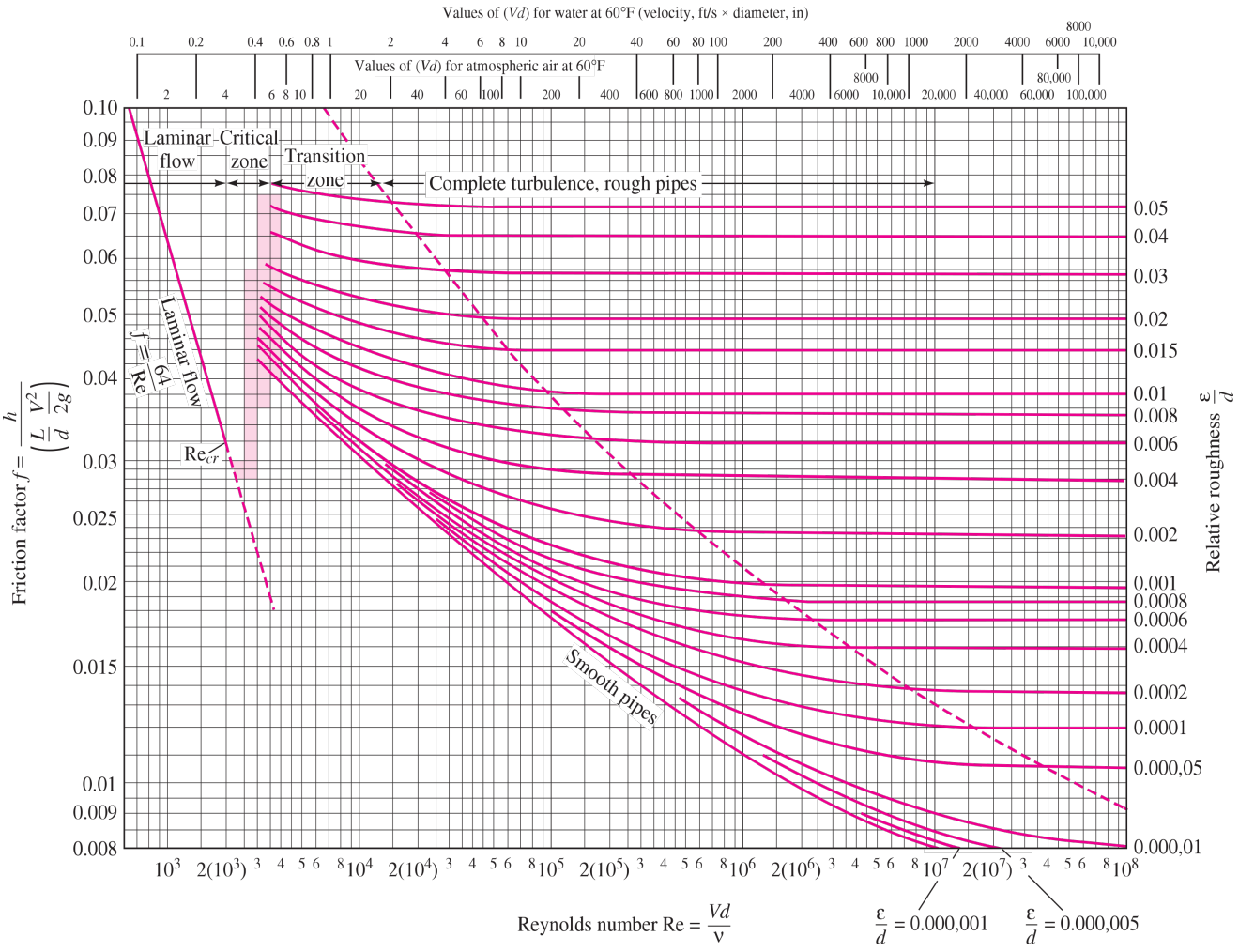

Figure B.1: Moody diagram; Taken from White et al. [67].

C

Appendix C: Transmitters for pressure, temperature and volumetric flow rate

In order to monitor and measure the flow properties,a flow meter, a differential pressure transducer, and a temperature sensor are installed. The specifications of each of these accessories are explained briefly below.

- **Flow meter**: A ABB DN200 electromagnetic flow meter type DS41P is used to measure the volumetric flow rate in the pipe. The current output of the flow meter (4-20 mA) is measured over a resistance and the voltage is obtained using an analog to digital converter attached with the computer. From the calibration sheet of the meter, the uncertainty in the reading meter is found to be 0.11%. The uncertainty increases with lower flow rates and it is higher than 0.11% for flow rates lower than 40 litres per second. The flow meter is placed 40 nozzle diameters downstream of the pump island.

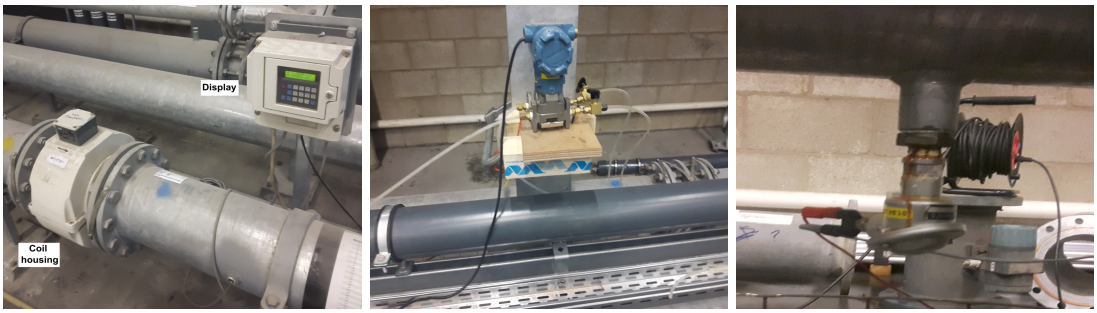

(a) ABB electromagnetic flow meter. (b) Differential pressure transducer. (c) Precision Pt100 probe.

Figure C.1: Transducers used to measure the (a) flow rate, (b) pressure drop (over 6.125 m pipe length), and (c) temperature of the fluid flow.

- **Differential pressure transmitter**: A Rosemount 3051 pressure transmitter is used to measure the differential pressure across the pipe. The transmitter measures the pressure drop across a pipe length of 6.125 m, 150 pipe diameters downstream of the pump island. The pressure drop is measured within 0.04% accuracy in the range 0 - 62.1 $mBar$. The data is obtained in the form of voltage, with an output current of 4-20

mA over resistance (internal loop resistance = 43.5 Ω). The pressure taps are connected in the side walls of the pipe to ensure that the transmitter is not affected by air bubbles (if present).

- **Temperature sensor**: A Precision Pt100 probe is used to measure the temperature of the fluid (water) at high accuracy. The sensor has an uncertainty of 0.06^oC at 0^oC. The range of the measurements at this accuracy is from -50^oC to 250^oC.

D

Appendix D: Experimental setup to study the optical disturbances captured in the PIV images

The intention of this experiment is to study the optical disturbances in the PIV images of the Alpha Loop facility. To mirror the transparent section in the Alpha Loop facility, a scaled down model is constructed with a glass box of 0.1 x 0.1 m^2 area.

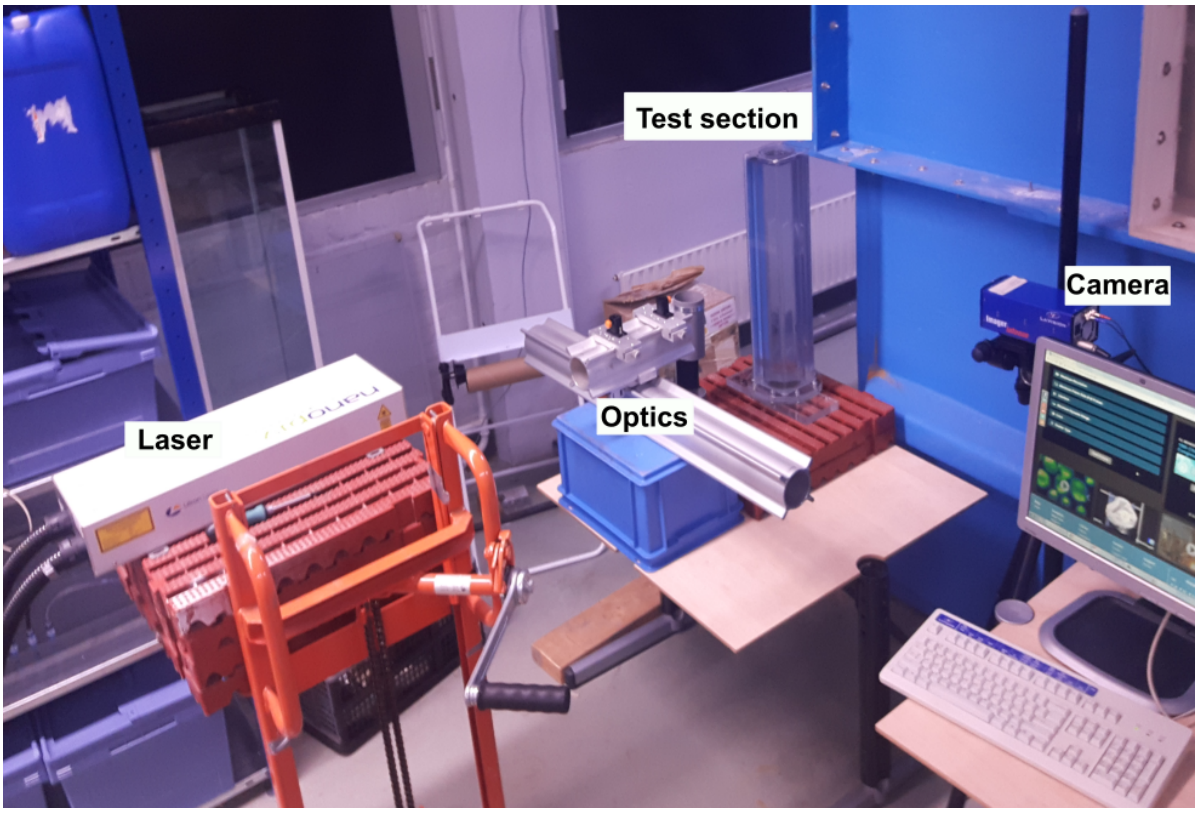

Figure D.1: Experimental setup to study the optical disturbances in the PIV images of pipe.

A 50 mJ dual cavity double pulsed laser is used to illuminate the field of view with 1 mm

laser light sheet. In order to produce the light sheet, cylindrical lens is used along with a spherical lens to make the sheet thinner. The image is recorded using 1 Megapixel *Imger Intense* camera. The magnification is 0.3. The f-number of the lens is 5.6.

Bibliography

[1] (2018). New pipelines to allow baku to increase gas supplies to foreign market.

[2] Adrian, R. J. (1991). Particle-imaging techniques for experimental fluid mechanics. *Annual review of fluid mechanics*, 23(1):261–304.

[3] Adrian, R. J. (2005). Twenty years of particle image velocimetry. *Experiments in fluids*, 39(2):159–169.

[4] Adrian, R. J. (2007). Hairpin vortex organization in wall turbulence. *Physics of Fluids*, 19(4):041301.

[5] Adrian, R. J. and Westerweel, J. (2011). *Particle image velocimetry*. Number 30. Cambridge University Press.

[6] Arkema. Plexiglas: Optical and transmission characteristics.

[7] Bali, A. (2017). Amazing bali tour travel.

[8] Billy, F., David, L., and Pineau, G. (2004). Single pixel resolution correlation applied to unsteady flow measurements. *Measurement Science and Technology*, 15(6):1039.

[9] Chakraborty, S. (2008). Some applications of dirac's delta function in statistics for more than one random variable. *Applications and applied mathematics*, 3(1):42–54.

[10] Choi, S. M., Kim, W. H., Côté, D., Park, C.-W., and Lee, H. (2011). Blood cell assisted in vivo particle image velocimetry using the confocal laser scanning microscope. *Optics express*, 19(5):4357–4368.

[11] Clauser, F. H. (1956). The turbulent boundary layer. In *Advances in applied mechanics*, volume 4, pages 1–51. Elsevier.

[12] Colebrook, C. and White, C. (1937). Experiments with fluid friction in roughened pipes. *Proc. R. Soc. Lond. A*, 161(906):367–381.

[13] Coles, D. (1956). The law of the wake in the turbulent boundary layer. *Journal of Fluid Mechanics*, 1(2):191–226.

[14] Delnoij, E., Westerweel, J., Deen, N. G., Kuipers, J., and van Swaaij, W. P. M. (1999). Ensemble correlation piv applied to bubble plumes rising in a bubble column. *Chemical Engineering Science*, 54(21):5159–5171.

[15] Den Toonder, J., Hulsen, M., Kuiken, G., and Nieuwstadt, F. (1997). Drag reduction by polymer additives in a turbulent pipe flow: numerical and laboratory experiments. *Journal of Fluid Mechanics*, 337:193–231.

[16] Dubassy. Stock video of timelapse of a power station next | 4125007 | shutterstock.

[17] El Khoury, G. K., Schlatter, P., Noorani, A., Fischer, P. F., Brethouwer, G., and Johansson, A. V. (2013). Direct numerical simulation of turbulent pipe flow at moderately high reynolds numbers. *Flow, turbulence and combustion*, 91(3):475–495.

[18] Fukushima, C., Aanen, L., and Westerweel, J. (2002). Investigation of the mixing process in an axisymmetric turbulent jet using piv and lif. In *Laser techniques for fluid mechanics*, pages 339–356. Springer.

[19] Gad-el Hak, M. and Bandyopadhyay, P. R. (1994). Reynolds number effects in wall-bounded turbulent flows. *Applied Mechanics Reviews*, 47(8):307–365.

[20] Hultmark, M., Vallikivi, M., Bailey, S., and Smits, A. (2012). Turbulent pipe flow at extreme reynolds numbers. *Physical review letters*, 108(9):094501.

[21] Ishikawa, M., Murai, Y., Wada, A., Iguchi, M., Okamoto, K., and Yamamoto, F. (2000). A novel algorithm for particle tracking velocimetry using the velocity gradient tensor. *Experiments in Fluids*, 29(6):519–531.

[22] Kähler, C., Scholz, U., and Ortmanns, J. (2006). Wall-shear-stress and near-wall turbulence measurements up to single pixel resolution by means of long-distance micro-piv. *Experiments in fluids*, 41(2):327–341.

[23] Kähler, C. J., Scharnowski, S., and Cierpka, C. (2012). On the uncertainty of digital piv and ptv near walls. *Experiments in fluids*, 52(6):1641–1656.

[24] Keane, R., Adrian, R., and Zhang, Y. (1995). Super-resolution particle imaging velocimetry. *Measurement Science and Technology*, 6(6):754.

[25] Keane, R. D. and Adrian, R. J. (1990). Optimization of particle image velocimeters. i. double pulsed systems. *Measurement science and technology*, 1(11):1202.

[26] Keane, R. D. and Adrian, R. J. (1992). Theory of cross-correlation analysis of piv images. *Applied scientific research*, 49(3):191–215.

[27] Kline, S. J., Coles, D. E., and Hirst, E. (1969). *Computation of turbulent boundary layers–1968 AFOSR-IFP-Stanford Conference: proceedings held at Stanford University, August 18-25, 1968*, volume 1. Thermosciences Division, Stanford University.

[28] Kunkel, G. J. and Marusic, I. (2006). Study of the near-wall-turbulent region of the high-reynolds-number boundary layer using an atmospheric flow. *Journal of Fluid Mechanics*, 548:375–402.

[29] Landreth, C. C. and Adrian, R. J. (1990). Impingement of a low reynolds number turbulent circular jet onto a flat plate at normal incidence. *Experiments in Fluids*, 9(1-2):74–84.

[30] Langelandsvik, L., Kunkel, G., and SMITS, A. J. (2008). Flow in a commercial steel pipe. *Journal of Fluid Mechanics*, 595:323–339.

[31] Marusic, I., McKeon, B., Monkewitz, P., Nagib, H., Smits, A., and Sreenivasan, K. (2010). Wall-bounded turbulent flows at high reynolds numbers: recent advances and key issues. *Physics of Fluids*, 22(6):065103.

[32] Marusic, I., Monty, J. P., Hultmark, M., and Smits, A. J. (2013). On the logarithmic region in wall turbulence. *Journal of Fluid Mechanics*, 716.

[33] McKeon, B. and Morrison, J. (2007). Asymptotic scaling in turbulent pipe flow. *Philosophical Transactions of the Royal Society of London A: Mathematical, Physical and Engineering Sciences*, 365(1852):771–787.

[34] Mckeon, B. J., Li, J.-d., Jiang, W., Morrison, J. F., and Smits, A. J. (2004). Further observations on the mean velocity distribution in fully developed pipe flow. *Journal of Fluid Mechanics*, 501:135–147.

[35] Meinhart, C. D., Wereley, S. T., and Santiago, J. G. (2000). A piv algorithm for estimating time-averaged velocity fields. *Journal of Fluids Engineering*, 122(2):285–289.

[36] Merlaud, A. (2012). Atmospheric boundary layer from mount meru, tanzania.

[37] Monty, J. P. (2005). *Developments in smooth wall turbulent duct flows*. PhD thesis, University of Melbourne, Department of Mechanical and Manufacturing Engineering.

[38] Morris, S. C., Stolpa, S. R., Slaboch, P. E., and Klewicki, J. C. (2007). Near-surface particle image velocimetry measurements in a transitionally rough-wall atmospheric boundary layer. *Journal of Fluid Mechanics*, 580:319–338.

[39] Morrison, J. F., McKeon, B., Jiang, W., and Smits, A. (2004). Scaling of the streamwise velocity component in turbulent pipe flow. *Journal of Fluid Mechanics*, 508:99–131.

[40] Nagib, H. M. and Chauhan, K. A. (2008). Variations of von kármán coefficient in canonical flows. *Physics of Fluids*, 20(10):101518.

[41] Nagib, H. M., Christophorou, C., and Monkewitz, P. A. (2006). High reynolds number turbulent boundary layers subjected to various pressure-gradient conditions. In *IUTAM symposium on one hundred Years of boundary layer research*, pages 383–394. Springer.

[42] Nieuwstadt, F. T., Westerweel, J., and Boersma, B. J. (2016). *Turbulence: introduction to theory and applications of turbulent flows*. Springer.

[43] Österlund, J. M., Johansson, A. V., Nagib, H. M., and Hites, M. H. (2000). A note on the overlap region in turbulent boundary layers. *Physics of Fluids*, 12(1):1–4.

[44] Outram, B. (2009). Black coatings to reduce stray light.

[45] Panchapakesan, N. and Lumley, J. (1993). Turbulence measurements in axisymmetric jets of air and helium. part 2. helium jet. *Journal of Fluid Mechanics*, 246:225–247.

[46] Perry, A., Henbest, S., and Chong, M. (1986). A theoretical and experimental study of wall turbulence. *Journal of Fluid Mechanics*, 165:163–199.

[47] Pope, S. (1994). Lagrangian pdf methods for turbulent flows. *Annual review of fluid mechanics*, 26(1):23–63.

[48] Saga, T., Kobayashi, T., Segawa, S., and Hu, H. (2001). Development and evaluation of an improved correlation based ptv method. *Journal of visualization*, 4(1):29–37.

[49] Scarano, F. (2001). Iterative image deformation methods in piv. *Measurement science and technology*, 13(1):R1.

[50] Schanz, D., Schröder, A., Gesemann, S., Michaelis, D., and Wieneke, B. (2013). Shake the box: a highly efficient and accurate tomographic particle tracking velocimetry (tomo-ptv) method using prediction of particle positions.

[51] Scharnowski, S., Hain, R., and Kähler, C. J. (2012). Reynolds stress estimation up to single-pixel resolution using piv-measurements. *Experiments in fluids*, 52(4):985–1002.

[52] Scholz, U. and Kähler, C. J. (2006). Dynamics of flow structures on heaving and pitching airfoils. In *13th International Symposium of Laser Techniques to Fluide Mechanics*.

[53] Shockling, M., Allen, J., and Smits, A. (2006). Roughness effects in turbulent pipe flow. *Journal of Fluid Mechanics*, 564:267–285.

[54] Smits, A., Monty, J., Hultmark, M., Bailey, S., Hutchins, N., and Marusic, I. (2011). Spatial resolution correction for wall-bounded turbulence measurements. *Journal of Fluid Mechanics*, 676:41–53.

[55] Soloff, S. M., Adrian, R. J., and Liu, Z.-C. (1997). Distortion compensation for generalized stereoscopic particle image velocimetry. *Measurement science and technology*, 8(12):1441.

[56] Song, X., Yamamoto, F., Iguchi, M., and Murai, Y. (1999). A new tracking algorithm of piv and removal of spurious vectors using delaunay tessellation. *Experiments in Fluids*, 26(4):371–380.

[57] Starck, J.-L., Pantin, E., and Murtagh, F. (2002). Deconvolution in astronomy: A review. *Publications of the Astronomical Society of the Pacific*, 114(800):1051.

[58] Strobl, C. (2017). *Single Pixel Particle Image Velocimetry for Measurements of Two-Dimensional Joint Velocity Distributions*. PhD thesis, Technische Universität München.

[59] Townsend, A. A. (1980). *The structure of turbulent shear flow*. Cambridge university press.

[60] Vallikivi, M., Hultmark, M., and Smits, A. J. (2015). Turbulent boundary layer statistics at very high reynolds number. *Journal of Fluid Mechanics*, 779:371–389.

[61] Van Dyke, M. (1982). An album of fluid motion.

[62] Warner, S. O. (2012). Autocorrelation-based estimate of particle image density in particle image velocimetry.

[63] Westerweel, J. (1993). *Digital particle image velocimetry: theory and application*. PhD thesis, TU Delft, Delft University of Technology.

[64] Westerweel, J. (2008). On velocity gradients in piv interrogation. *Experiments in Fluids*, 44(5):831–842.

[65] Westerweel, J., Fukushima, C., Pedersen, J. M., and Hunt, J. (2009). Momentum and scalar transport at the turbulent/non-turbulent interface of a jet. *Journal of Fluid Mechanics*, 631:199–230.

[66] Westerweel, J., Geelhoed, P., and Lindken, R. (2004). Single-pixel resolution ensemble correlation for micro-piv applications. *Experiments in Fluids*, 37(3):375–384.

[67] White, F. M. et al. (2003). Fluid mechanics.

[68] Willert, C. E., Soria, J., Stanislas, M., Klinner, J., Amili, O., Eisfelder, M., Cuvier, C., Bellani, G., Fiorini, T., and Talamelli, A. (2017). Near-wall statistics of a turbulent pipe flow at shear reynolds numbers up to 40 000. *Journal of Fluid Mechanics*, 826.

[69] Yakhot, V., Bailey, S. C., and Smits, A. J. (2010). Scaling of global properties of turbulence and skin friction in pipe and channel flows. *Journal of Fluid Mechanics*, 652:65–73.

[70] Zagarola, M. V. and Smits, A. J. (1998). Mean-flow scaling of turbulent pipe flow. *Journal of Fluid Mechanics*, 373:33–79.